TALLINN UNIVERSITY OF TECHNOLOGY
DOCTORAL THESIS
27/2019

Development of Room Temperature Secondary Fluoride Ion Batteries

IRSHAD MOHAMMAD

TALTECH
PRESS

TALLINN UNIVERSITY OF TECHNOLOGY
School of Information Technologies
Department of Health Technologies
This dissertation was accepted for the defense of the degree 17/05/2019

Supervisor:	Associate Professor Raiker Witter School of Information Technologies Tallinn University of Technology Tallinn, Estonia
Co-supervisor:	Dr. Ago Samoson (leading scientist) School of Information Technologies Tallinn University of Technology Tallinn, Estonia
Opponents:	Professor Ulla Lassi, D.Sc. Research Unit of Sustainable Chemistry School University of Oulu Oulu, Finland
	Professor Radostina Stoyanova Institute of General and Inorganic Chemistry Bulgarian Academy of Sciences Sofia, Bulgaria

Defence of the thesis: 10/06/2019, Tallinn

Declaration:
Hereby I declare that this doctoral thesis, my original investigation and achievement, submitted for the doctoral degree at Tallinn University of Technology has not been submitted for a doctoral or equivalent academic degree.

Irshad Mohammad

----

signature

European Union
European Regional
Development Fund

Investing
in your future

ISSN 2585-6898 (publication)
ISBN 978-9949-83-431-0 (publication)
ISSN 2585-6901 (PDF)
ISBN 978-9949-83-432-7 (PDF)

TALLINNA TEHNIKAÜLIKOOL
DOKTORITÖÖ
27/2019

Toatemperatuursete fluoriidioon akude väljaarendamine

IRSHAD MOHAMMAD

TALTECH
KIRJASTUS

Contents

List of Publications

The list of author's publications, based on which the thesis has been prepared:

I **Mohammad, I.**; Chable, J.; Witter, R.; Fichtner, M.; Reddy, M. A., Synthesis of Fast Fluoride-Ion-Conductive Fluorite-Type $Ba_{1-x}Sb_xF_{2+x}$ ($0.1 \leq x \leq 0.4$): A Potential Solid Electrolyte for Fluoride-Ion Batteries. *ACS Appl. Mater. Interfaces* 2018, *10*, 17249-17256.

II **Mohammad, I.;** Witter, R.; Fichtner, M.; Anji Reddy, M., Room Temperature Rechargeable Solid-State Fluoride Ion Batteries. *ACS Appl. Energy Mater.* 2018, 1, 4766-4775.

III **Mohammad, I.**; Witter, R.; Fichtner, M.; Anji Reddy, M., Introducing Interlayer Electrolytes: Towards Room Temperature High Potential Solid State Rechargeable Fluoride Ion Batteries. *ACS Appl. Energy Mater.* 2019, 2, 1553−1562.

IV **Mohammad, I.**; Witter, R., Testing Mg as an anode against BiF_3 and SnF_2 cathodes for room temperature rechargeable fluoride ion batteries. *Materials Letters* 2019, 244, 159-162.

Author’s Contribution to the Publications

The contribution to the publications by author in this thesis is:

I Synthesis and ionic conductivity study of $Ba_{1-x}Sb_xF_{2+x}$ ($0.1 \le x \le 0.4$) compounds, XRD and EIS characterizations, solid-state FIB cells assembly, analysis of electrochemical results, and a leading role in writing and conceiving the idea of the project.

II Preparation of all battery components ($BaSnF_4$ as an electrolyte, BiF_3 as a cathode, and Sn and Zn as anodes), XRD and SEM characterizations, fabrication of FIB cells, analysis of galvano-static results, a significant role in writing, and contribution in conceiving the idea of the project.

III Preparation and ionic conductivity study of $La_{0.9}Ba_{0.1}F_{2.9}/BaSnF_4$ layers, SEM and EXD mapping analysis, EIS and XRD characterizations, cell preparation and electrochemical testing, a significant role in writing, and contribution in conceiving the idea of the project.

IV Synthesis and characterization of electrode materials such as $Mg+MgF_2$, BiF_3, and SnF_2, cell fabrication and testing, a leading role in writing and conceiving the idea of the project.

Abbreviations

ASSB	All-solid-state batteries
EDX	Energy dispersive X-ray spectroscopy
EIS	Electrochemical impedance spectroscopy
FIB	Fluoride-ion battery
LIB	Lithium-ion battery
SIB	Sodium-ion battery
SEM	Scanning electron microscopy
XRD	X-Ray Diffraction
RT	Room temperature
EV	Electric vehicles
HEV	Hybrid electric vehicles
PHEV	Plug-in hybrid electric vehicles
PVDF	Polyvinylidene fluoride
SBR	Styrene-butadiene rubber
1D	One-dimensional
2D	Two-dimensional
3D	Three-dimensional
LFP	$LiFePO_4$
LCO	$LiCoO_2$
NCM	$LiNi_xCo_yMn_zO_2$
CIB	Chloride ion battery
FSB	Fluoride shuttle battery
DC	Direct current
CV	Cyclic voltammogram
EC	Ethylene carbonate
DMC	Dimethyl carbonate
a.u.	atomic units
OCV	Open circuit voltage
Emf	Electromotive force
CNT	Carbon nano tubes
LTO	Lithium titanate
RT	Room temperature is assigned to 25 °C here
rpm	Revolutions per minutes

Introduction

Efficient electricity storage, i.e., batteries are considered to be the superior energy storage option in many contexts. Currently, lithium-ion batteries (LIBs) are the main power sources for portable electronics and have been introduced in the transportation sector to power electric vehicles (EVs) and also in smart grid applications. As the demand for portable devices such as mobile phones, electric vehicles, and intermittent renewable energy is of increasing interest, scientists are investigating alternative technologies based on different chemistries. Rechargeable battery systems based on cation transportation such as LIB, sodium-ion battery (SIB), lead-acid battery, nickel-metal hydride battery and hydrogen fuel cells, have been widely investigated. The electrochemical storage technology based on anion (negative) transport has been introduced recently and is an emerging hot topic. In the regard of an anion transport, batteries based on OH^-, F^-, Cl^-, and $AlCl_4^-$ have been investigated. Fluorine is the most electronegative element in the periodic table and has a high charge density. Also, the small size of fluoride ion facilitates fast ion transportation and kinetic diffusion. Therefore, it can be considered a stable and suitable ion as a charge carrier in the battery. An electrochemical cell based on F^- transport can be constructed by placing a fluoride ion conducting electrolyte between a metal and metal fluoride electrodes.

Fluorine combines with metals to form monovalent, bivalent or trivalent metal fluorides, which means metals can store multiple electrons per metal reversibly, and therefore, high theoretical capacities can be achieved. Apart from high voltage and specific energy promise, solid-state fluoride batteries (FIBs) can provide high thermal stability and better safety due to nonflammable nature of fluorides. The primary electrochemical cell based on fluoride ion transfer was demonstrated long time ago. However, not much progress has been made until the demonstration of rechargeable solid-state fluoride ion batteries [1]. Since then, significant development has been made to improve the performance of the FIBs, with a focus on electrolytes, electrode materials, and lowering the operating temperature. However, all efforts have managed just to demonstrate the proof of principle of FIBs. Their work does not to touch the heart of problem, no proper candidate for electrolyte, cathode or anode has been proposed so far. $La_{0.9}Ba_{0.1}F_{2.9}$ was used as solid electrolyte for demonstration of the first rechargeable FIB, since then no better solid electrolyte has been discovered [1]. Only handful of groups remained working in the field of FIBs.

So far, the highest specific capacity of 360 $mA \cdot h \cdot g^{-1}$ has been obtained for CuF_2 electrode, but this value was limited to high temperature (150 °C) and low current density (10 $\mu A \cdot cm^{-2}$), which is much inferior to LIB system [2]. Although the demonstration of rechargeable room temperature FIB employing liquid elecrolyte has been reported, but the cell delivered low voltage (≈0.2 V) and current (10 $\mu A \cdot cm^{-2}$), not enough for practical applications [3].

The focus of this thesis is centered on making progress with FIBs, first of all, explore a principal possibility to make a rechargeable solid-state fluoride ion battery that can operate at the room temperature. This presumes finding a suitable solid electrolyte with high ionic conductivity and wide electrochemical stability window. This thesis describes the synthesis of new electrode and solid-state electrolyte materials and study of their chemical and physical properties, followed by demonstration of their applications in fluoride ion batteries. In addition, this thesis explores new approaches to design and develop of advanced electrodes and electrolytes from currently existing compositions.

A new fluorite type nano-structured $Ba_{1-x}Sb_xF_{2+x}$ ($x \leq 0.4$) fluoride ion conductor was synthesized by mechanical milling. In addition, testing of $Ba_{0.7}Sb_{0.3}F_{2.3}$ as high capacity cathode material for rechargeable solid-state FIBs is discussed, by using $La_{0.9}Ba_{0.1}F_{2.9}$ as a solid electrolyte, and Ce as an anode (**I**). The thesis presents successful demonstration of the rechargeable solid-state FIB systems, which are working at ambient temperature, by employing $BaSnF_4$ as fluoride ion electrolyte, BiF_3 as a cathode, and Zn and Sn as anodes (**II**). The concept of interlayer electrolytes for FIBs using $La_{0.9}Ba_{0.1}F_{2.9}$ and $BaSnF_4$ is discussed here. Combining high conductive and electrochemically stable electrolyte layers enabled the demonstration of relatively high potential solid-state FIB working at RT. This fluoride ion battery was built using $La_{0.9}Ba_{0.1}F_{2.9}$ (90 µm)/$BaSnF_4$ (650 µm) as electrolyte, Ce as anode, and BiF_3 as cathode (**III**). The feasibility of using Mg as anode for rechargeable RT-FIBs is reported, by investigating the electrochemical performance of BiF_3/Mg+MgF_2 and SnF_2/Mg+MgF_2 electrochemical couples using $LiPF_6$ as fluoride ion transporting in EC and DMC organic solvents **(IV)**.

The thesis is based on four articles, published in international peer-reviewed journals and composed of three main chapters. Chapter 1 presents the literature overview of the batteries that contains different sections where principle and fundamentals of batteries, and rechargeable batteries with both cation and anion shuttles are described. In the end of chapter 1, the motivation and scope of the study is outlined. Chapter 2 covers experimental part that contains different sections where all materials which are used in the study, synthesis of different electrodes and electrolytes materials, and performed analytical methods are illustrated. Chapter 3 states the results and discussion part which categorized into five sections. Section 3.1 summarizes the results of SbF_3-doped BaF_2 compounds synthesized by ball milling method. Section 3.2 synopsis the results of demonstration of RT rechargeable solid-state FIBs using $BaSnF_4$. Results on interlayer electrolytes concept for solid-state FIBs are outlined in section 3.3. The outcomes on Mg as an anode against BiF_3 and SnF_2 cathodes for RT-FIBs are summarized in section 3.4. Section 3.5 summarizes the unpublished, yet important preparatory work leading to the development of RT-FIB.

1 Literature Overview

1.1 Battery fundamentals

Batteries are electrochemical devices that convert chemical energy into electric energy via redox reactions between positive and negative electrodes. The electrochemical redox reactions such as oxidation and reduction involve the transfer of electrons from one electrode material to the other through an external circuit. In case of a secondary system, the battery is recharged by consecutive reversible redox reaction. The major advantage of batteries is that they operate in a non-isothermal condition where Carnot limitation is not applied. Thus, batteries are considered as very efficient energy conversion devices [4-6].

A battery consists of several components such as anode, cathode, electrolyte, and separator as shown in Figure 1.1. The anode is the negative electrode where oxidation reaction occurs by releasing electrons which travel through an external circuit to the cathode. The cathode is the positive electrode where reduction reaction takes place by gaining electrons from the anode via an external circuit.

The electrolyte is an ionic conductor with negligibly small electronic conductivity, which facilitates the ion transfer between one electrode to another and separates the electrodes electronically to avoid short circuit. Usually, the electrolyte is a liquid solution containing dissolved salts, acids, alkalis to participate in the ionic conductivity. Batteries are also fabricated with ion-conducting polymers or solid electrolytes. A battery built by solid electrolyte is called all-solid-state (ASSB).

The basic building block of any battery is the electrochemical cell. Batteries are composed of one or more electrochemical cells connected in series or parallel or both to supply required power [7].

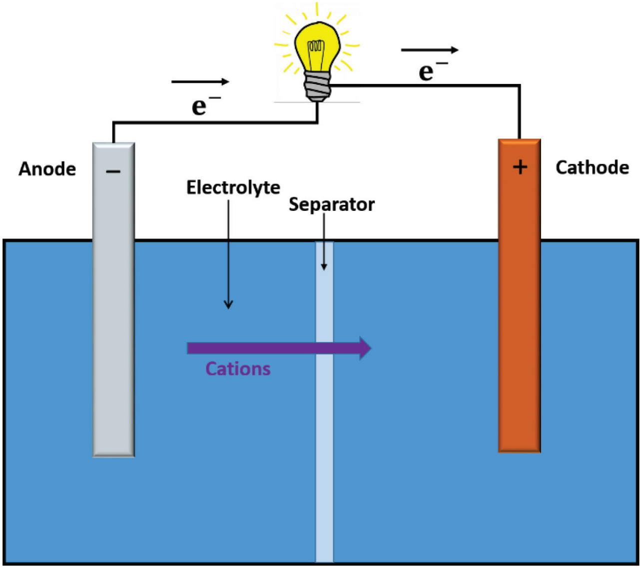

Figure 1.1. *Schematic of a battery during the discharge process.*

Each half-cell reaction is associated with standard cell potential $E°$, which can be calculated from the thermodynamic relations using material and reaction specific data as follow by Equation 1.1:

$$E° = -\frac{\Delta G}{z\,F} \tag{1.1}$$

where $E°$ is standard half-cell potential (V), ΔG is standard Gibbs free energy in "$\mathrm{kJ{\cdot}mol^{-1}}$", z is number of electrons transferred, and F is Faraday constant in "$\mathrm{C{\cdot}mol^{-1}}$".
The overall standard potential $\Delta E°$ of a redox reaction is obtained by subtracting standard cell potential of the anode ($E^{\circ(-)}$) from standard cell potential of the cathode ($E^{\circ(+)}$) using Equation 1.2:

$$\Delta E° = E^{\circ(+)} - E^{\circ(-)} \tag{1.2}$$

The value of potential difference between anode and cathode can be varied by choosing different electrode materials, but this value also depends upon other factors such as temperature and activity of working materials (mainly cathode) participating in the reaction. When conditions are other than standard, then the electrochemical potential of a half-cell can be calculated using Nernst Equation 1.3:

$$E = E° - \frac{RT}{zF}\ln\frac{a_{\mathrm{Red}}}{a_{\mathrm{ox}}} \tag{1.3}$$

where, E is potential, $E°$ is standard potential, R is ideal gas constant in "$\mathrm{mol^{-1}{\cdot}K^{-1}}$", T stands for absolute temperature in "$\mathrm{K^{-1}}$", z is a number of electrons transferred, F is Faraday constant, a_{Red} stands for the activity of substance being reduced and a_{Ox} stands for the activity of substance being oxidized. Activity is a measure of effective concentration of a species in a mixture.
The important characteristics of a battery are potential difference, capacity, power, and energy. The capacity of the battery is equal to the product of the total amount of charge, when fully discharged under a given condition, and time. The theoretical capacity q in "$\mathrm{mA{\cdot}h{\cdot}g^{-1}}$" is calculated by Faraday's law (Equation 1.4):

$$q = \frac{z\,F}{3600M} \tag{1.4}$$

where q is the capacity, M is molecular weight of active material in the unit of "$\mathrm{kg{\cdot}mol^{-1}}$", z is number electrons transferred, and F is Faraday constant.
The practical, specific capacity is capacity obtained by applying constant current until the battery reaches it cut off. The value of practical, specific capacity in "$\mathrm{mA\ h\ g^{-1}}$" can be calculated by following equation (Equation 1.5):

$$\text{practical, specific capacity} = \frac{j \times A \times t_{\mathrm{cutoff}}}{3600M} \tag{1.5}$$

where j is the current density in "$\mathrm{A{\cdot}m^{-2}}$", A is the area in "$\mathrm{m^2}$", and t_{cutoff} is the time to reach the cut off voltage in second, and M is the weight of active material in "kg".

Energy density is a very important feature of a battery because it determines the performance of the battery and it is the amount of specific energy stored in per unit mass or volume. The specific energy is the product of specific capacity and voltage, the energy in “Wh·kg^{-1}” of battery material can be derived as follows (Equation 1.6):

$$\text{Specific energy} = \frac{\int_0^{t_\text{cutoff}} V(t) \times j \times a \times \text{dt}}{3600 \times M} \tag{1.6}$$

where V is a voltage of the battery in volts, j is in “A·m^{-2}”, A is in “m^2”, and t_cutoff is in seconds, and M is in “kg”.

Power, another important factor in determining battery performance, is the energy that can be obtained per unit time. The average specific power of battery can be derived as follow (Equation 1.7):

$$\text{Specific power} = \frac{\int_0^{t_\text{cutoff}} V(t) \times j \times A \times \text{dt}}{M \times \int_0^{t_\text{cutoff}} \text{dt}} \tag{1.7}$$

V is in volts, j is in “A·m^{-2}”, A is in “m^2”, and t_cutoff is in seconds, and M is in “kg”.

Batteries can be divided into two major classes: primary and secondary. Primary batteries such as zinc-carbon, alkaline manganese, and lithium manganese dioxide cannot be recharged and must be replaced after reactants are depleted. Whereas the secondary batteries, for example, lead-acid, Ni-Cd, Ni-MH, and lithium ion are rechargeable and DC power source can bring reactants back to their charged state [8-12]. In the upcoming section, a detailed description of rechargeable lithium-ion batteries will be presented.

1.2 Rechargeable lithium-ion batteries

Batteries based on cation shuttles such as Li^+, Na^+, Ca^{2+}, and Mg^{2+} have been widely investigated [13-16]. In particular, Li-ion batteries (LIBs) are the best studied and best performing system among all cation shuttles-based batteries. LIBs can provide high energy density (250–693 Wh·L^{-1}), high voltage, low weight energy storage [17-19]. Secondary batteries such as lead-acid or Ni-MH have been already utilized for hybrid electric vehicles (HEV) and plug-in hybrid electric vehicles (PHEV). However, they cannot compete with secondary lithium-ion batteries in the regard of small size and high-power density. The other advantages of LIBs are relatively low self-discharge and absence of memory effect. However, the practical driving range of LIBs is still not competitive with conventional petrol, which can provide 80 times higher gravimetric and 20 times higher volumetric energy densities [20]. However, it should be noted that only about 30% of the liquid fuel energy can be converted in motion/electrical power. A disadvantage of lithium-ion batteries is that they fade when discharged below 2 V and may suffer a damage when overcharged, because they are not protected by a chemical mechanism to handle the over charge, unlike aqueous cell chemistries.

Commercial LIBs use lithium metal oxides materials as positive electrode (cathode), and lithiated carbon as negative electrode (anode). The most frequently used cathode and anode materials are $LiCoO_2$, and graphite, respectively. Typically, electrodes consist of the anode or cathode active material, carbon black to insure electronic conductivity, and binder to hold the electrode particles together and ensure a contact with the current collectors [17]. The positive electrode adheres to aluminum current collector, and the negative electrode adheres to the copper current collector. The positive and negative electrodes are separated by a thin electron-insulator separator (layer) sucked with electrolyte (generally liquid). The electrolyte is usually a liquid solution made by dissolving the lithium salt in an organic solvent which is a mixture of cyclic and linear aliphatic carbonates (ethylene carbonate, dimethyl carbonate, respectively). Lithium hexafluorophosphate ($LiPF_6$) is the most frequently used electrolyte among all available lithium salts [21]. The separator is a permeable membrane typically comprising either polymeric membrane (such as poly ethylene, poly propylene) or non-woven fabric mat (such as polyolefin, polyamide).

1.2.1 The operating principle of lithium-ion batteries

On charge, lithium ions are extracted from the cathode (lithium-containing, e.g. $LiCoO_2$), pass across the electrolyte and intercalated into the anode by an electrochemical reduction reaction at the anode. During discharge, an electrochemical oxidation occurs at the anode, lithium ions are de-intercalated and shuttled across the electrolyte to be re-intercalated into the cathode material, due to charge balance the equivalent number of electrons travel through the external circuit. Figure 1.2 illustrates the working mechanism of lithium-ion batteries. This technology is termed as "rocking chair" batteries due to their working principle [22].

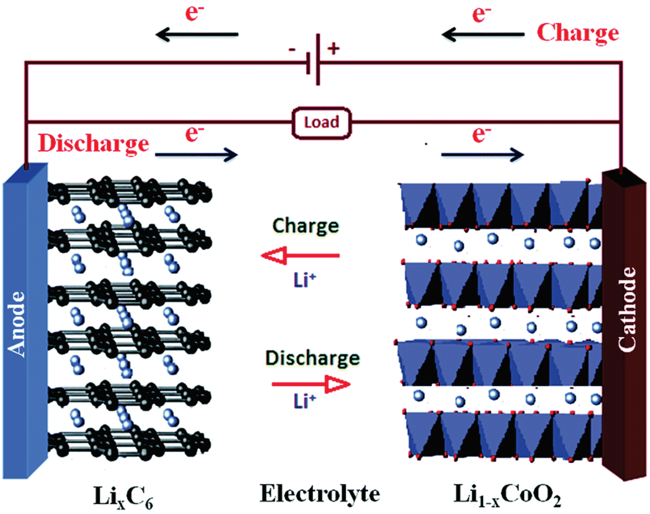

Figure 1.2 *Charge-discharge mechanism of lithium-ion batteries [23].*

The electrochemical reactions of electrodes during charge-discharge process can be expressed in a following way:

Cathode:

$$LiCoO_2 \rightleftarrows Li_{1-x}CoO_2 + xLi^+ + xe^-$$

Anode:

$$C_y + xLi^+ + xe^- \rightleftarrows Li_xC_y$$

Overall:

$$LiCoO_2 + C_y \rightleftarrows Li_xC_y + Li_{1-x}CoO_2.$$

1.2.2 Development of graphite anode material

The first commercial rechargeable lithium batteries were introduced in 1980s, using pure lithium metal as a negative electrode, but failed to make impact in the market due to the high safety risk [24]. The major disadvantage of lithium metal was the formation of dendrites during cycling, leading to a poor performance and eventually short circuit inside the battery, which can cause a fire and explosion inside the battery. Afterwards, scientists resolved this issue in the some extent by introducing lithium aluminum (Li−Al) alloy as an anode [25]. Later, many lithium metal alloys have been investigated as alternative anode materials, although they exhibit reduced energy densities as compared to the pure lithium metal [26]. Moreover, a major drawback of lithium metal alloy is the volume change during the insertion and de-insertion of lithium ions from alloy matrices, provoking the disintegration of the alloy by cracking and crumbling [27]. Thus, it was concluded that lithium metal alloys have short cycle life and low energy efficiency, which were the main obstacles to commercialize the lithium metal alloys as anode materials for lithium ion batteries. To address the drawbacks of lithium metal or lithium alloy anode, graphite carbon as anode material was discovered. Graphite carbon shows high structural stability during insertion and extraction of lithium ions [28-30]. The electrochemical intercalation of lithium into graphite results in the formation of LiC_6 which causes only about a 10% increase of the distance between the graphite layers [31]. Later, batteries with lithium titanate ($Li_4Ti_5O_{12}$ or LTO) anodes were introduced. LTO replaces graphite anode in LIBs and it forms into spinel structure [32-34]. In comparison to graphite-based LIBs, these systems can be recharge more quickly and provide higher currents when required.

1.2.3 The most common types of cathode materials

Common commercial rechargeable lithium ion batteries utilize lithium iron phosphates $LiFePO_4$ (LFP), layered oxides $LiMeO_2$ (Me=Ni, Co, Mn, etc.), and manganese spinel $LiMn_2O_4$ as cathode materials [35-41]. The crystal structure of different types of cathodes is displayed in Figure 1.3. *Olivine*−type cathode material LFP offers several benefits such as flat voltage profile, high theoretical capacity (170 $mA{\cdot}h{\cdot}g^{-1}$), and good thermal and cyclic performance. Further, LFP is low-priced and provides better safety. But, LFP faces slow insertion or extraction of lithium ions due to its 1D diffusion pathway [42]. The $LiMeO_2$ (Me=Ni, Co, Mn, etc.) compounds with α−$NaFeO_2$ type structure have been widely investigated as cathode materials for rechargeable LIBs. This structure exhibits a 2D lithium diffusion pathway, which enables easy insertion or extraction of lithium ions yielding high theoretical capacity. $LiCoO_2$ (LCO) was the first to be commercially available with relatively high capacity (274 $mA{\cdot}h{\cdot}g^{-1}$), low self-discharge and good cyclic performance. It remains a dominant cathode material at the commercial market. Later, $LiNiO_2$ has been discovered as cathode material for rechargeable LIBs, which shows higher capacity than that of LCO, but is more difficult to synthesize via usual synthesis routes [40]. Also, this material tends to decompose into partially ordered $Li_{1-x}Ni_{1+x}O_2$, after high temperature treatment [40]. Thereafter, $LiMnO_2$ has been investigated as alternatives to LCO and $LiNiO_2$ in addition to low cost and toxicity. However, during the electrochemical cycling, $LiMnO_2$ favors transforming into spinel, which results in poor performance [43]. An attempt to improve the performance of layered oxides it lead to the discovery of the $LiNi_xCo_yMn_zO_2$ (NCM) compound [44]. NCM is one of the best materials which offers a relatively high theoretical capacity of 160 $mA{\cdot}h{\cdot}g^{-1}$, and good performance. But, at higher voltage the problem of transition metal dissolution still persists, causing a rapid cell failure [45]. Spinel, $LiMn_2O_4$, was been introduced in commercial lithium ion batteries [41]. This material exhibits 3D lithium diffusion pathway and constitutes one of the most attractive cathode materials in terms of low cost, high natural abundance of Mn, and low toxicity. Its theoretical capacity is 148 $mA \cdot h \cdot g^{-1}$ providing the specific capacity about 100 to 120 $mA \cdot h \cdot g^{-1}$by charging up to 4.10–4.20 V against Li/Li^+.

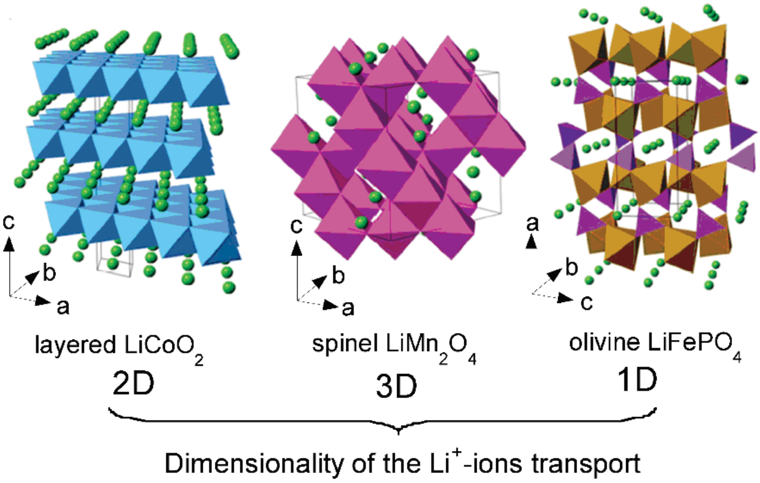

Figure 1.3. *Crystallographic structure of the most commonly used cathode materials, in which the* Li^+ *ions are diffuse through the 2-D (layered), 3-D (spinel) and 1-D (olivine) frameworks [46].*

1.3 Rechargeable Fluoride ion batteries

Besides positive ion shuttle batteries, new battery technologies based on a negative ion as charge carrier such as Cl^- and F^- have been reported recently [1, 47]. The chloride ion battery (CIB) was first demonstrated by Fichtner's group using ionic liquid or organic solvent-based electrolytes [47, 48]. Since then, development of the chloride system has progressed significantly [49-53]. The chlorine ion batteries offer a theoretical energy density up to 2500 $Wh \cdot L^{-1}$ for some selected electrodes combination [47]. The first proof of principle of chloride ion system was presented using a mixture of ionic liquids-based electrolyte, carbon composite of simple chloride salts such as $CoCl_2$, VCl_3, and $BiCl_3$ as cathodes and Li as the anode [47]. The cell with $BiCl_3$ as cathode showed good stability in the electrolyte and relatively low volume changes during electrochemical cycling. Recently, a solid-state chloride ion battery was constructed using gelatin PVDF−HF membrane as the electrolyte, CuF_2/C (carbon black) and PANI as cathodes and Zn metal sheet as an anode [54]. The CIB cell with PANI cathode delivered the discharge capacity of around 160 $mA \cdot h \cdot g^{-1}$, whereas CuF_2/C as cathode-based cell yielded the discharge capacity of around 150 $mA \cdot h \cdot g^{-1}$ at a constant current of 10 µA [54]. In contrast to chloride, fluoride ion has low weight and high charge density, hence it is good for fast ion transportation and kinetic diffusion. The electrochemical cell based on fluoride ion as charge transfer was already introduced 40 years ago [55-60]. However, the potential of FIBs was unnoticed until 2011, when Anji Reddy and Fichtner demonstrated FIBs operating at a relatively low 150 °C as compared to earlier 500 °C [1].

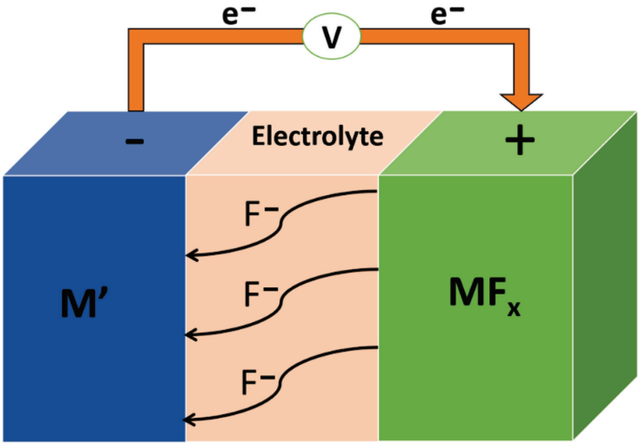

Figure 1.4. *Schematic diagram of fluoride ion battery during the discharge process.*

The reaction mechanism of chloride and fluoride ion batteries are the same. The representative sketch of fluoride ion battery is shown in Figure 1.4, which depicts the working principle of the FIB system. In the figure, metal fluoride MF_x is generally used as a cathode, whereas metal M is used as the anode. During discharge, electrons are generated in spontaneous redox reaction at the anode. These electrons move through an external circuit to combine with the cathode, where metal fluoride MF_x reduces to metal M. The released fluoride ions depart from the cathode and migrate through the electrolyte to react with metal M' of the anode to form $M'F_x$, assuring the electroneutrality. The charge process is reverse to the discharge. The electrochemical reaction of the battery during the discharge process can be expressed by following way,

Anode:

$$xF^- + M' \rightarrow M'F_x + xe^-$$

Cathode:

$$MF_x + xe^- \rightarrow M + xF^-$$

Overall:

$$MF_x + M' \rightarrow M + M'F_x$$

Using an appropriate combination of electrodes, theoretical energy densities for FIBs are estimated to more than 5000 $Wh{\cdot}L^{-1}$ [61]. The high energy density is due to the large change in free energy during the formation of the different metal fluorides, resulting in high theoretical voltages. Further, more than one electron can be reversibly stored when bivalent or trivalent metals react with several fluorides, yielding high theoretical specific capacities. For example, theoretical discharge capacities of BiF_3, CuF_2, and FeF_3 are estimated to 302, 528, and 712 $mA{\cdot}h{\cdot}g^{-1}$, respectively. Apart from high theoretical energy promises, fluoride ion batteries provide high thermal stability and better safety due to low-toxicity of metal fluorides. A couple of earlier examples of primary electrochemical cell based on fluoride ion transport have been already reported in the literature. Buakal constructed a FIB using doped-CaF_2 as a solid electrolyte, metal fluorides (NiF_2 or CuF_2) as cathode material, and metallic magnesium as anode material [56]. The FIB cells were investigated at relatively high temperatures of 400–500 °C [56]. However, no electrochemical data were reported about the reversibility of these cells. A FIB cell based on thin film technology was fabricated by Kennedy and Hunter employing PbF_2 as a solid electrolyte, Pb as anode material, and CuF_2 as cathode material [57]. The thin film based FIBs were possible to discharge about 30 to 40% of their theoretical capacity at voltage range of 0.4 to 0.5 V, however no reversibility of cells was reported [57]. Another primary cell was reported by Hagenmuller et al. using β-PbF_2 as a solid electrolyte, Pb as anode and BiF_3 as cathode [58]. J. Schoonman tried with $BiO_{0.09}F_{2.82}$ as cathode instead of BiF_3 and found similar outcomes [59]. Better results were reported by Potanin using doped LaF_3 and CeF_3 as solid electrolytes, doped PbF_2 and BiF_3 as cathodes, and La and Ce as anodes [60]. The PbF_2 based cell delivered a discharge capacity of 130 $mA{\cdot}h{\cdot}g^{-1}$, whereas the BiF_3 based cell exhibited a discharge capacity of 200 $mA{\cdot}h{\cdot}g^{-1}$ [60]. The higher capacities were obtained between voltage of 2.0 and 2.4 V, but again at relatively high operational temperature of 500 °C.

In the recent study mentioned above, Anji and Fichtner built rechargeable FIBs using tysonite-type $La_{0.9}Ba_{0.1}F_{2.9}$ as a solid electrolyte, several metal fluorides such as BiF_3, CuF_2, SnF_2, and $KBiF_4$ as cathodes, and Ce metal foil as an anode [1]. They have investigated the electrochemical property of FIB cells at a temperature of 150 °C. The first discharge capacity of 322 $mA{\cdot}h{\cdot}g^{-1}$ with an average discharge voltage of 2.5 V was obtained for Ce/CuF_2 couple, however no charge capacity was presented [1]. The Ce/BiF_3 system delivered a first discharge capacity of 190 $mA{\cdot}h{\cdot}g^{-1}$ at an average voltage of 2.15 V, and it showed a first recharge capacity of 131 mA h g^{-1}, meaning that 69% of the first discharge capacity could be recovered [1]. However, the capacities faded during the following cycles and it decreased to 50 $mA{\cdot}h{\cdot}g^{-1}$ after 38 cycles. Since then, various approaches have been employed to improve the performance of the FIBs, for example, testing batteries in discharge state, using Mg-MgF_2 composite as anode, employing thin film based (tysonite-type) electrolyte, demonstrating intercalation compounds as cathodes [62-66]. However, all these approaches have required the operational temperature of 150 °C or above to ensure the ionic conductivity of any significance. Up to date, only reports that have demonstrated fluoride ion batteries working at room temperature were using not solid, but liquid electrolytes [3, 67-69]. In a recent study, RT-FIB was investigated using poly (ethylene glycol) (PEG) based compound as liquid electrolyte, Mg as an anode, and BiF_3 as a cathode. The cell displayed high discharge capacity of 250 $mA{\cdot}h{\cdot}g^{-1}$, when applying current 10 μA [68]. Despite obtaining such a high first discharge capacity, the cell failed to deliver any reversible capacity. A new study demonstrated the rechargeable fluoride shuttle battery (FSB), compromising ionic liquid-based electrolyte, PbF_2 as the anode, and Bi as a cathode. The FSB cell was charged and discharged reversibly for few cycles, however the operating voltage was quite low (≈0.2 V) [3]. All above studies were completely based on conversion type electrode materials. Conversion, unlike intercalation materials break and create new chemical bonds during insersion and extraction of F^-. For example, BiF_3 as cathode reduced or converted to metallic Bi during discharge, releasing three fuoride ions via breaking three Bi-F bonds. However, conversion reactions at electrodes are known to have several issues such as capacity fading, low cyclability, and slow transport kinetics, which is associated with significant volume changes during the conversion and crystallization process. To reduce these issues, intercalation reaction based compounds such as $LaSrMnO_4$, La_2CoO_4, and $BaFeO_{2.5}$ as cathodes for FIBs have been investigated [64-66]. The key component of FIB is the electrolyte, which is a medium for fluoride ion shuttling between the electrodes. The electrolyte should possess a wide electrochemical stability window, in addition to the high ionic conductivity. In the upcoming section, few fluoride ion conductors will be presented.

1.3.1 Solid-state fluoride ion conductors

Fluoride ion conductors are known to possess high ionic conductivity. A variety of fluorides compounds such as fluorite-type (alkaline-earth fluorides), tysonite-type (rare-earth fluorides), lead-based fluorides (PbF_2 or $PbSnF_4$), and tin-based fluorides ($BaSnF_4$ or $SrSnF_4$) can be considered as solid electrolytes for FIBs. Among available metal fluorides, two types of fluorides with fluorite type-structure (e.g. CaF_2) and tysonite type struture (e.g. LaF_3) are known to possess high ionic conductivity, in addition to their wide electrochemical stability, which is commendable for battery application [70-81]. Mostly, alkaline-earth fluorides (MF_2, M = Mg, Ca, Ba) adopt a fluorite-type structure (space group, Fm-3m), while rare-earth metal fluorides (RF_3, R = La, Ce, Pr) crystallize into a tysonite-type structure (space group, P-3c1). In the case of fluorite type compound, fluoride ions conduction is mainly due to the migration of interstitial fluoride ions [76, 82, 83]. In tysonite-type compounds, the ionic conductivity is mainly dominated by the migration of fluoride vacancies [76, 84]. However, most of the reported studies on these compounds have been done on single crystals but for batteries application polycrystalline powders are more compatible due to shaping issues. Further, several studies have been reported that nanocrystalline fluorite type fluorides showed higher conductivity than the corresponding single crystals [82]. In contrast, nanocrystalline tysonite compounds displayed less conductivity as compared to the corresponding single crystals [84]. For polycrystalline materials, the conductivity that proceeds through migration of interstitial F^- ions in fluorite type fluorides, is dominated by the grain boundaries, but the conductivity that proceeds via migration of vacancies in the tysonite-type fluorides is partly obstructed by the presence of grain boundaries. The grain boundaries of both types of compounds are associated with different properties. This difference could be associated to the creation of different types of extrinsic defects. The defects created by aliovalent doping in tysonite and fluorite compounds are vacancies (e.g. LaF_3 by Ba) and interstitials F^- (e.g. BaF_2 by La), respectively. It has been establisehd that the vacancies created in tysonite type fluoride ($La_{0.9}Ba_{0.1}F_{2.9}$) are very mobile in the bulk but partially obstructed by the grain boundary barrier and have less effect on defects created at the grain boundaries. This behaviour is totally different to what was observed in fluorite type compounds ($Ba_{1-x}La_xF_{2+x}$) where the interstitials F^- are less mobile but influence greatly the vacancies present in the grain boundary region. The vacancies in the grain boundary could be accumulated by negatively charged interstitial F^- ions presented on surface of the bulk. Rongeat et al. have concluded that if the defects present in bulk (interstitial F^- ions) do not contribute directly to the conduction, then they probably influence the defects (vacancies) present in the grain boundaries [82].

The conductivity of both types of metal fluorides (fluorite and tysonite) could be increased by aliovalent doping. For example, Ivanov-Shits and coworkers synthesized $Ca_{1-x}R_xF_{2+x}$ and $Ba_{1-x}R_xF_{2+x}$ (R = rare-earth elements) compounds by doping of CaF_2 and BaF_2 with rare-earth metal fluorides (RF_3), respectively [70, 85]. They studied the ionic conductivity of doped fluorite structured compounds at temperatures range of

300–800 K. The maximum conductivity of 1.2 × 10^{-4} S·cm^{-1} and 1.9 × 10^{-4} S·cm^{-1} was obtained for $Ca_{0.65}Dy_{0.35}F_{2.35}$ and $Ba_{0.6}La_{0.4}F_{2.4}$ at 500 K, respectively [70, 85]. Sorokin's group further studied the ionic conductivity of doped fluorite-type materials in single crystal ($Sr_{1-x}R_xF_{2+x}$, $Ba_{1-x}R_xF_{2+x}$ and $Ca_{1-x}R_xF_{2+x}$) at temperatures range of 300–1100 K, and found similar results [71, 73]. Recently, Rongeat et al. have prepared nanocrystalline fluorite-type $Ba_{1-x}La_xF_{2+x}$ ($0 \le x \le 0.55$) solid solutions and they also obtained similar conductivity [82]. The maximum ionic conductivity of 1.9 × 10^{-4} S·cm^{-1} was obtained for nanocrystalline $Ba_{0.6}La_{0.4}F_{2.4}$ at 160 °C [82].

Tysonite-type doped compounds have been widely investigated, and they are considered as the best candidates for solid electrolytes of FIBs. Tysonite-type crystallographic lattice provides high ion conductivity that can be greatly improved by aliovalent cation substitution (Ba^{2+}, Sr^{2+}, and Ca^{2+}) [86-88]. Takahashi et al. synthesized CeF_3 based solid solutions by doping with different alkali metal fluorides such as CaF_2, SrF_2, BaF_2 and ThF_4 [78]. They found that the conductivity was increased by 5% for all divalent metal fluorides. However, a decrease in conductivity was observed for dopant ThF_4. For the single crystal, it is reported that tysonite doped compound could show high value of ionic conductivity even at room temperature [78]. For example, the ionic conductivity of pure LaF_3 single crystals is around 10^{-6} S·cm^{-1} at 298 K, but after doping with a little amount of BaF_2 the conductivity of $La_{0.95}Ba_{0.05}F_{2.95}$ single crystals increased to around 10^{-4} S·cm^{-1} at 298 K [79, 87]. In contrast to single crystals, polycrystalline materials (tysonite) do not show such high ionic conductivity at RT, where conduction is hindered by F^- ion transfer through the grain boundaries. Rongeat and coworkers studied the ionic conductivity of poly crystalline tysonite-type $La_{1-x}Ba_xF_{3-x}$ ($0 \le x \le 0.15$) compounds [84]. They found the highest ionic conductivity of 2.8 × 10^{-4} S·cm^{-1} at 160 °C for nanocrystalline $La_{0.9}Ba_{0.1}F_{2.9}$ and it was considered as the best electrolyte for solid-state FIBs [84]. This value of ionic conductivity was slightly less than the corresponding single crystal, which is usual in the case of tysonite type fluorides. Recently, Düvel et al. and other's investigated nanocrystalline tysonite-type compounds and obtained similar results [89].

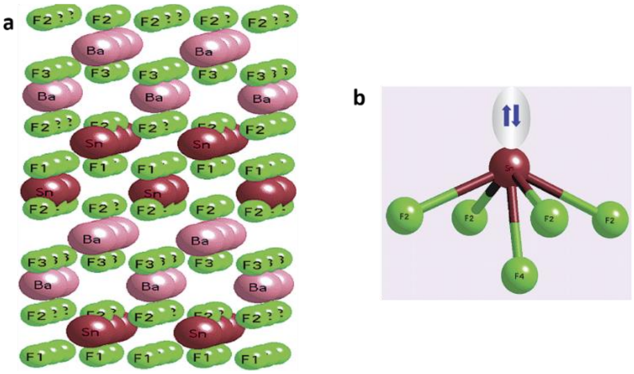

Figure 1.5. Layered structure of tetragonal $BaSnF_4$ displaying different cation layers and fluoride ions. (b) Sn coordination environment of $BaSnF_4$ showing lone pairs on Sn^{2+} pointing in the c-direction [90].

In contrast to tysonite-type fluorides, lead or tin-based compounds ($PbSnF_4$, $BaSnF_4$) show high ionic conductivity also as polycrystalline materials, [90-95]. The ionic conductivity of $PbSnF_4$ is about 10^{-3} S·cm^{-1}, whereas the ionic conductivity of $BaSnF_4$ and $SrSnF_4$ is about 10^{-4} S·cm^{-1}, respectively, at 298K [93, 95]. The high ionic conductivity in tin containing compound is due to effect of lone pair of electrons on Sn^{2+} atom, which strongly influences the fluoride sub-lattice and contributes to the high ionic conductivity in $BaSnF_4$ [90]. The crystal structure of tetragonal $BaSnF_4$ is given in Figure 1.5. This structure can be derived from the cubic fluorite-type structure by ordering the Sn and Bn cations in Sn-Sn, Ba-Sn, and Ba-Ba layers, along the c-direction of tetragonal cell. This ordering results in three different fluoride sites, termed as F1, F2, and F3, and they reside in Sn-Sn, Ba-Sn, and Ba-Ba layers, respectively. The stereoactive lone pair induces a repulsive interaction between the lone pair electron and negatively charged fluoride ion, which lead to depletion of the fluoride ions in the Sn−Sn and Sn−Ba layers of $BaSnF_4$ crystal structure (Tetragonal). Hence, all fluorides between Sn-Sn and Sn-Ba layers become mobile and are involved in conduction process. The local environment of F3 ions in the Ba−Ba layers is very similar to that of BaF_2 crystal, and they held rigidly in the lattice. Also, these compounds ($BaSnF_4$ and $PbSnF_4$) can be synthesized by mechanical milling and they exhibit ionic conductivity similar to the corresponding material synthesized by high temperature sintering. Polycrystalline materials with high room temperature conductivity can be considered as suitable electrolytes for RT-FIBs. However, these electrolytes have not been tested as solid electrolyte in practical FIBs.

The ionic conductivity of the compound is generally evaluated by impedance spectroscopy. The conductivity is determined by measuring the complex impedance using a blocking electrode arrangement. To measure the impedance, generally, an electrolyte material in the form of a disc or pressed pellet is prepared, connected between two equivalent electrodes. The resistance R of the electrolyte is obtained from complex impedance spectra (Nyquist plots), and the ionic conductivity is calculated by the following Equation 1.8:

$$\sigma = \frac{d}{AR} \tag{1.8}$$

where σ is the ionic conductivity, d is the pellet thickness, and A is the cross-sectional area of the pellet.

The relation between ionic conductivity and temperature is governed by the Arrhenius equation, which is given below (Equation 1.9):

$$\sigma \times T = \sigma_0 \times e^{-(E_a/kT)} \tag{1.9}$$

where E_a, k, and σ_0 correspond to activation energy, Boltzmann constant, and pre-exponential factor, respectively. After simplification of equation 1.8, $-E_a/k$ and $\ln(\sigma_0)$ correspond to slope and intercept, respectively.

1.4 Summary of literature overview and aim of the study

At present, lithium-ion batteries are superior among all power sources of portable electronics and being launched in the transportation sector to drive HEV, PHEV, also for a smart grid storage application. Generally, state-of-the-art LIBs use $LiCoO_2$, $LiNiCoAlO_2$, $LiFePO_4$, and $LiNi_xMn_yCo_zO_2$ compounds as positive electrodes. As the demand for electrochemical devices keeps increasing, factors like thermal instability and high cost of $LiCoO_2$ also geographically constrained and finite availability of Li need to be considered. This intensifies the search for alternative approaches. The systems such as Na^+, Mg^{2+}, Ca^{2+}, Zn^{2+}, Al^{3+}, and F^- have been introduced and studied consistently. The important properties of elemental fluorine such as high charge density, high electronegativity, and relatively low weight make F^- an attractive charge transporting and storing ion. FIB can be built by combining a suitable fluoride electrolyte with a metal and a metal fluoride electrode. So far, two types of rechargeable FIBs have been reported, the all solid-state FIB, which employs a solid-state electrolyte and operates at high temperature, and FIB working at room temperature, which uses a liquid electrolyte. Apart from providing high energy density, FIB offers a good thermal stability and better safety possibly at a lower price than LIB. This type of system is at the beginning of development and large improvement is still needed regarding the performance of electrodes and electrolytes to live up the potential. In addition to the fast transport of the ions between the electrodes, the electrolyte should feature also a large electrochemical stability window. The electrolyte and especially the interface should be stable against the chemical reactions occurring at anode and cathode materials. The metal fluorides with tysonite-type structures such as $La_{0.9}Ba_{0.1}F_{2.9}$ and $Ce_{0.975}Sr_{0.025}F_{2.975}$ are probably the best candidates for electrolytes for FIBs. However, in the nanocrystalline powder form they have failed to deliver enough conductivity so far. Nanocrystalline powders of Sn-based conductors such as $PbSnF_4$ and $BaSnF_4$ show a high conductivity at room temperature but they have not been introduced in batteries application.

Based on the literature overview on solid-state fluoride ion batteries and theoretical considerations the objectives of the present doctoral thesis were selected on following hypotheses:

1. For efficient and low-cost working cells, the selection of electrolyte is crucial. High ionic conductive and low-cost fluorides would be suitable choice for electrolyte. As mentioned earlier, some of tin-doped compounds ($BaSnF_4$ or $SrSnF_4$) possess high ionic conductivity at RT due to the effect of lone pair electrons of Sn^{2+}. Besides Sn^{2+}, there are other cations containing lone pair of electrons such as Sb^{3+}, Bi^{3+}, and Tl^{3+}, which can be considered to maintain a similar effect on ionic conductivity. However, the effect of these ions in their doped compounds has not been studied so far. In this context, SbF_3-doped BaF_2 compounds were synthesized in our group, assuming that Sb^{3+} carrying a lone pair of electrons, might strongly participate to increasing the ionic conductivity of BaF_2. Also, SbF_3 material is relatively inexpensive compared to other fluorides.

2. Solid-state FIB systems operate at higher temperatures like 150 °C or beyond. However, for many practical applications, batteries working at ambient temperature are required. Up to date, solid-state FIBs working at RT have not been demonstrated due to lack of inadequate choice of electrolyte and electrode materials. Here, polycrystalline $BaSnF_4$ was chosen as a solid electrolyte for demonstrating RT-FIB due to its high ionic conductivity. Although the ionic conductivity of polycrystalline $PbSnF_4$ is 1 order of magnitude higher compared to the $BaSnF_4$, it was decided to work with $BaSnF_4$ as Pb-free electrolyte. For constructing FIB cells, Sn and Zn were selected as anodes, considering their predicted electrochemical stability with $BaSnF_4$. BiF_3 as a cathode was chosen for FIBs due to its high ion conductivity and good electrochemical stability.

3. The feasibility of RT-FIBs could be demonstrated using $BaSnF_4$ as an electrolyte, Sn and Zn as anode, and BiF_3 as cathode, but at the cost of low cell voltage due to the low voltage redox couples (Sn/BiF_3 and Zn/BiF_3). The low operating voltage would lead to low energy density of battery. One way to increase the voltatge is the use of high electropositve metals (Ce, La, etc) as anodes, however they are not compatible with $BaSnF_4$ due to the limited electrochemical stability of $BaSnF_4$. Until now, there is no any fluoride conductor, which possesses high RT ionic conductivity as well as wide electrochemical stability window. To overcome both low electrochemical stability and low ionic conductivity for the electrolyte of fluoride ion battery, the interlayer electrolytes concept was proposed here. The interlayer electrolyte is composed of a thin layer of $La_{0.9}Ba_{0.1}F_{2.9}$ and thick layer of $BaSnF_4$. The electrochemical stability of $BaSnF_4$ can be enhanced by placing $La_{0.9}Ba_{0.1}F_{2.9}$ in contact with high electropositive anodes.
4. Reports of FIBs based on liquid electrolytes are scares. As mentioned above, one reports fabricated a FIB cell utilizing ionic based liquid as electrolyte. Although, the reversibility of FIB was demonstrated, but the cell voltage was quite low (≈0.2 V). Because they have built the FIB using low redox potential couple: PbF_2/Bi system. To build high voltage RT-FIBs, high redox couples such as Mg/BiF_3 and Mg/SnF_2 have been investigated here. In this work, FIB cells were constructed using $LiPF_6$ as electrolyte.

Therefore, **the aims of this thesis** are as follows:

1. To synthesize the fluorite-type $Ba_{1-x}Sb_xF_{2+x}$ ($0.1 \le x \le 0.4$) solid solutions by high energy ball milling method, and study their ionic conductivity using electrochemical impedance spectroscopy, establish and test the most conductive composition as cathode a material for rechargeable solid-state fluoride ion batteries.
2. To demonstrate the room-temperature rechargeable solid-state fluoride ion batteries using $BaSnF_4$ as solid electrolyte, Sn and Zn as anodes, and BiF_3 as cathode, and investigate the mechanism of electrochemical reaction by ex-situ XRD, and SEM studies.
3. To introduce interlayer electrolytes ($La_{0.9}Ba_{0.1}F_{2.9}$/$BaSnF_4$) concept for building high potential solid-state RT-FIBs, optimize the total ionic conductivity of the interlayer electrolyte by altering the thickness of the $La_{0.9}Ba_{0.1}F_{2.9}$ layer, and validate the compatibility of this electrolyte with high electropositive metals like Ce in FIB, while using optimized cathodes, in particular fluorite-type $Ba_{1-x}Sb_xF_{2+x}$ as studied in aim 1.
4. To demonstrate Mg as reversible anode material of rechargeable fluoride ion batteries employing $LiPF_6$ as liquid electrolyte, when SnF_2 and BiF_3 are used as cathodes, and investigate Mg/BiF_3 and Mg/SnF_2 electrode systems, by means of discharge-charge testing, cyclic voltammetry, and X-ray diffraction.

2 Experimental

Prior to use, all the materials (except SnF_2) were dried for 15 hours (h) at 200 °C under vacuum and stored into Ar filled glove box.

2.1 Materials

All materials were obtained from Sigma-Aldrich and Alfa-Aesar. A detailed description of all materials is given in below Table 2.1.

Table 2.1. *Description of materials.*

Materials	Formula	Purity	Supplier
Barium fluoride	BaF_2	99.9%	Sigma-Aldrich
Antimony fluoride	SbF_3	99.6%	Alfa-Aesar
Calcium fluoride	CaF_2	99.9%	Sigma-Aldrich
Potassium fluoride	KF	99.97%	Sigma-Aldrich
Silver fluoride	AgF	99%	Sigma-Aldrich
Cerium fluoride	CeF_3	99.9%	Alfa-Aesar
Strontium fluoride	SrF_2	99.995%	Sigma-Aldrich
Lead fluoride	PbF_2	99.6%	Alfa-Aesar
Cobalt fluoride	CoF_3	99%	Alfa-Aesar
Copper fluoride	CuF_2	99.5%	Alfa-Aesar
Lanthanum fluoride	LaF_3	anhydrous, 99.9%	Sigma-Aldrich
Carbon nanotubes	CNT	95%	Sigma-Aldrich
Cerium powder	Ce	99.9%	Alfa-Aesar
Zinc powder	Zn	99.9%	Sigma-Aldrich
Tin fluoride	SnF_2	99%	Alfa-Aesar
Bismuth trifluoride	BiF_3	anhydrous, 98%	Alfa-Aesar
Tin powder	Sn	99%	Sigma-Aldrich
Bismuth powder	Bi	99.9%	Sigma-Aldrich
Mg powder	Mg	99.8%	Sigma-Aldrich
Mn powder	Mn	99.3%	Alfa-Aesar
Fe powder	Fe	99%	Alfa-Aesar
Yttrium powder	Y	99.5%	Sigma-Aldrich
Calcium granular	Ca	99%	Sigma-Aldrich
Titanium	Ti	99 % (metal basis)	Alfa-Aesar
Misch metal powder	Ce:La 75:25 wt%	99%	Alfa-Aesar
Magnesium fluoride	MgF_2	99.99%	Sigma-Aldrich
Lithium hexafluorophosphate	$LiPF_6$	1.0 M $LiPF_6$ in EC/DMC = 50/50 (v/v)	Sigma-Aldrich

2.2 Synthesis

Mechanical milling was used for mixing and synthesis of electrode and electrolytes samples, respectively. $Ba_{1-x}Sb_xF_{2+x}$ (0.1 ≤ x ≤ 0.5) compounds were prepared by ball milling of a mixture of stoichiometric amounts of BaF_2 and SbF_3 for 18 h at 600 rpm under argon atmosphere [**I**]. $Ba_{0.7}La_{0.3}F_{2.3}$ was produced according to the previous report [82] by ball milling of a mixture of appropriate amounts of BaF_2 and LaF_3 for 18 h at 600 rpm [**I**]. $La_{0.9}Ba_{0.1}F_{2.9}$ was obtained in relation to the earlier study [84] by milling stoichiometric amounts of BaF_2 and LaF_3 for 12 h at 600 rpm under an Ar atmosphere [**I, III**]. Ball milling of these compounds was performed using vial (volume, 80 mL) and balls (20 balls, diameter of 10 mm) made of silicon nitride with a ball-to-powder weight ratio of 12:1. Tetragonal $BaSnF_4$ was synthesized by the same way as described in the past [92]. First, the cubic phase of $BaSnF_4$ was synthesized by ball milling the stoichiometric ratios of BaF_2 and SnF_2 for 12 h at 600 rpm [**II, III**]. And then, as-milled $BaSnF_4$ was annealed at 300 °C for 2 h under vacuum to obtain its tetragonal phase [**II, III**]. The mixing of electrode composites and synthesis of $BaSnF_4$ were performed using zirconium dioxide jars (volume, 80 mL) and 20 balls (diameter, 10 mm) with the ball to power weight ratio of 16:1. All Milling was performed using a planetary-type mill (FRITSCH Pulverisette 6). Composition and preparation of different electrodes are given in Table 2.2.

Table 2.2. *A description of electrode composites and their preparation.*

Electrode short name	**Composition (weight %)**	**Milling time and speed**	**Ref.**
$Ba_{0.7}Sb_{0.3}F_{2.3}$ (cathode)	90% $Ba_{0.7}Sb_{0.3}F_{2.3}$+ 10% CNTs	6 h and 100 rpm	[**I**]
Ce (anode)	90% Zn + 10% CNTs	3 h and 200 rpm	[**I**]
Zn (anode)	40% Zn + 50% $La_{0.9}Ba_{0.1}F_{2.9}$ +10% CNTs	12 h and 200 rpm	[**I**]
BiF_3 (cathode)	40% BiF_3 + 50% $BaSnF_4$+ 10% CNTs	6 h and 100 rpm	[**II, III**]
Sn (anode)	Step 1→ 84% Sn + 16% CNTs (C-Sn)	6 h and 300 rpm	[**II**]
	Step 2→ 60% C-Sn + 40% $BaSnF_4$	6 h and 100 rpm	
Zn (anode)	Step 1→ 84% Zn + 16% CNTs (C-Zn)	6 h and 300 rpm	[**II**]
	Step 2→ 60% C-Zn + 40% $BaSnF_4$	6 h and 100 rpm	
Ce (anode)	Step 1→ 84% Ce + 16% CNTs (C-Ce)	2 h and 200 rpm	[**III**]
	Step 2→ 60% C-Ce + 40% $La_{0.9}Ba_{0.1}F_{2.9}$	2 h and 100 rpm	
BiF_3 (cathode)	90% BiF_3 + 10% Carbon black	6 h and 600 rpm	[**IV**]
SnF_2 (cathode)	90% SnF_2 + 10% Carbon black	6 h and 600 rpm	[**IV**]
Mg (anode)	50% Mg + 40% MgF_2 + 10% Carbon black	6 h and 600 rpm	[**IV**]

2.3 Battery assembly and electrochemical testing

All-solid-state FIB cells were constructed in an Ar-filled glovebox. The three-layer pellet was assembled by pressing anode/electrolyte/cathode layers together. The layers were pressed for one minute applying a pressure of two tons using a desktop pressing tool (Specac). The diameter and thickness of the pressed pellets were approximately 7 mm and 0.8 mm, respectively. The three-layer pellets were then transferred into a modified

Swagelok cell specially designed and fabricated for working at elevated temperatures. The schematic photograph of modified Swagelok cell with battery components and band heater is given in Figure 2.1 [**I-III**].

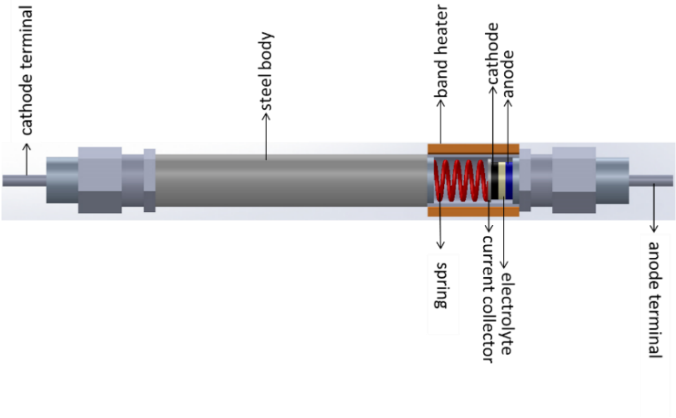

Figure 2.1. *Schematic sketch of the modified Swagelok cell.*

In paper [**I**], the galvanostatic charge-discharge profiles of solid-state FIB cells were obtained at temperatures of 150 °C. In paper [**III**], electrochemical investigation on FIB cells was carried out at 25 and 150 °C. In the case of paper [**II**], the electrochemical studies were done at different temperatures such as 25, 60, 100, and 150 °C. Galvano-static cycling of the cells was carried out using Arbin battery cycling unit [**I-III**]. The cyclic voltammetry measurement of cells was performed using a Biologic instrument [**II**]. The cells of paper [**I**] and [**III**] were cycled at current densities of 10 $\mu A \cdot cm^{-2}$, whereas the cells of paper [**II**] were cycled at different current densities such as 10, 20, and 40 $\mu A \cdot cm^{-2}$. In paper [**IV**], the FIB cells were assembled in the CR2023 case cell and their electrochemical analysis was done using Keysight DC power analyzer (N6705B). For all the cells, the specific capacity was calculated based on the weight of active material in the cathode composite. Typically, the total mass of the cathode composite used for the cell fabrication was approximately 5 mg. For all electrochemical tests, the anode amount was used in excess compared to the active material of cathode. Different types of FIB cells were constructed, and their detailed descriptions are given in Table 2.3.

Table 2.3. *Different types of FIB systems with their cycling current densities and temperatures.*

S.N.	**FIB system anode/electrolyte/cathode**	**Current density ($\mu A \cdot cm^{-2}$)**	**Temperature (°C)**	**Ref.**
1	$Ce/La_{0.9}Ba_{0.1}F_{2.9}/Ba_{0.7}Sb_{0.3}F_{2.3}$	10	150	[**I**]
2	$Zn/La_{0.9}Ba_{0.1}F_{2.9}/Ba_{0.7}Sb_{0.3}F_{2.3}$	10	150	[**I**]
3	$Sn/BaSnF_4/BiF_3$	10, 20	25, 60, 100,150	[**II**]
4	$Zn/BaSnF_4/BiF_3$	10, 40	25, 60, 150	[**II**]
5	$Ce/La_{0.9}Ba_{0.1}F_{2.9}/BaSnF_4/BiF_3$	10	25	[**III**]
6	$Ce/BaSnF_4/BiF_3$	10	25	[**III**]
7	$Mg+MgF_2/LiPF_6/BiF_3$	38	25	[**IV**]
8	$Mg+MgF_2/LiPF_6/SnF_2$	38	25	[**IV**]

2.4 Electrochemical impedance spectroscopy (EIS)

Ionic conductivity was evaluated by EIS analysis. EIS measurements were done using a Zahner IM6 electrochemical device. The frequency range was 8 MHz to 1 Hz, and the voltage amplitude was 10 mV. The measured EIS data were fitted using ZView and EC-Lab software's. Impedance measurements were performed on pellets pressed with a tow tons force for one minute and coated with gold which was sputtered on both sides used as ion-blocking electrodes. The thickness and diameter of the pellet were approximately 0.8 and 7 mm, respectively. For solid-state electrolytes, impedance spectra were recorded at different temperatures ranging from 25 °C to 200 °C [**I-III**]. The electronic conductivity of $Ba_{0.6}Sb_{0.4}F_{2.4}$ composition was measured by chronoamperometry at a constant voltage of 2.0 V using a Bio-Logic VMP 3 instrument [**I**].

2.5 Characterization Methods

The different methods and apparatus used for the characterization of electrode composites and electrolytes are summarized in Table 2.4.

Table 2.4. *Methods used for the characterization of electrode composites and electrolytes.*

Properties	**Characterization method**	**Apparatus**	**Ref.**
phase composition, cell parameter, crystallite size	XRD	STOE STADI P instrument with Mo Kα source	[**I-III**]
phase composition of both sides of battery pellet before and after discharge	ex-situ XRD	Bruker D8 Advance diffractometer Cu Kα radiation	[**II, III**]
Surface morphology, cross-sectional view, the average thickness of FIB and interlayer components,	SEM	ZEISS LEO 1530VP SEM	[**I-III**]
Surface morphology of cathode and anode sides of a battery pellet before and after discharge	ex-situ SEM	ZEISS LEO 1530VP field SEM	[**II**]
Elemental composition	EDX	LEO 1530VP SEM with field emission electron gun (Tungsten)	[**II, III**]
phase composition of cathode side of battery pellet before and after discharge	ex-situ XRD	AXS Bruker D5005 Advance instrument with Cu Kα radiation	[**IV**]

The XRD measurements were performed to identify the phase composition of synthesized electrode composites and electrolytes [**I-III**]. The cell parameters and average crystallite sizes were determined by performing Profile Matching refinements of the XRD patterns [**I-III**]. The refinement was done using Le Bail method with the FullProf software [96]. Instrumental broadening was taken into consideration using

LaB_6 as reference diffraction data. The sample contribution to X-ray line broadening was determined by using Thompson−Cox−Hastings pseudo-Voigt function that consists both size and strain-broadening terms for Lorentzian and Gaussian constituents [97]. The apparent crystallite size and the upper limit of micro strain of the sample were internally calculated using Langford's method with the FullProf software [98]. The reaction mechanism of FIBs was investigated by performing ex situ XRD measurements on the battery pellets before and after discharge [**II, III**]. In the paper [**IV**], the reaction mechanism of battery was investigated by XRD analysis on cathode before and after discharge. For recording XRD patterns, the pellets after electrochemical testing were transferred into dome type sample holders (Bruker AXS Inc.) equipped with a knife edge beam stop for low background and sealed inside an Ar-filled glovebox. The SEM analysis was performed on both sides of battery pellet to monitor the distribution of active material, a solid electrolyte, and CNT particles [**II**]. The average thickness of each component of FIB was determined by SEM analysis of a cross section of the battery pellet [**II, III**]. The EDX mapping analysis was carried on Sn and Zn composites to observe the distribution of active material, electrolyte, and CNT [**II**]. The SEM and corresponding EDX analysis of a cross section of the inter-layer electrolyte pellet [$La_{0.9}Ba_{0.1}F_{2.9}$ (20 mg)/$BaSnF_4$ (120 mg)] was performed to measure the average thickness of each component of pellet and to monitor the distribution of $BaSnF_4$ and $La_{0.9}Ba_{0.1}F_{2.9}$, respectively [**III**]. Similar to the interlayer electrolyte, SEM and corresponding EDX was also performed for the interlayer electrolyte-based FIB pellet [**III**]. Like ex situ XRD, ex situ SEM measurements were carried out on charged and discharged pellets [**II**].

3 Results and Discussion

The following sections 3.1-3.4 summarize the results of studies related to fluorite-type electrolyte and room temperature fluoride ion batteries. The results have been presented in papers [**I**], [**II**], [**III**], and [**IV**] and reflect what can be considered as a "publishable" outcome of a more extensive effort, comprising initial probing , selection of specific research targets and many failed experiments. This part, inevitable as such, is described briefly in section 3.5.

3.1 Synthesis and ionic conductivity study of SbF_3-doped BaF_2 solid solutions [I]

3.1.1 Synthesis and structure of $Ba_{1-x}Sb_xF_{2+x}$ ($0 \le x \le 0.5$) compounds

$Ba_{1-x}Sb_xF_{2+x}$ ($0 \le x \le 0.5$) samples were synthesized by mechanical milling of stoichiometric mixtures of BaF_2 and SbF_3. The XRD patterns of all compositions after 18 h of milling are given in Figure 3.1. The diffraction peaks corresponding to a fluorite-type structure which were obtained for all compositions except $Ba_{0.5}Sb_{0.5}F_{2.5}$, confirming the formation of solid solution (Figure 3.1a). The XRD pattern of $Ba_{0.5}Sb_{0.5}F_{2.5}$ compound displayed few extra peaks, besides the peaks corresponding to the fluorite-type structure (marked *) indicating the formation of an impure phase with $x > 4$. The peaks corresponding to dopant 0.3 and 0.4 were slightly shifted towards higher reflection angle compared to that of BaF_2, which was expected (Figure 3.1b). However, reflections corresponding to dopant 0.1 and 0.2 shifted towards lower angle compared to that of BaF_2. Corresponding cell parameter and crystallite size values were calculated by described profile matching refinement. As expected, a reduction of the cell dimension was observed for $Ba_{0.7}Sb_{0.3}F_{2.3}$ and $Ba_{0.6}Sb_{0.4}F_{2.4}$ samples in comparison to the BaF_2 crystal structure (Figure 3.1c). This decrease can be attributed to the insertion of the relatively smaller sized Sb^{3+} (ion radius of 0.76 Å in VI coordination in SbF_3) into the BaF_2 crystal network, where sizes of Ba^{2+} are 1.35 and 1.42 Å in VI and VIII coordination, respectively [99][93]. In contrast, $Ba_{0.9}Sb_{0.1}F_{2.1}$ and $Ba_{0.8}Sb_{0.2}F_{2.2}$ compositions show an increase in cell dimension (compared to BaF_2), which was unexpected. The increase in cell dimension is associated with the size of Sb^{3+} substituent and existing lone pair electrons on Sb^{3+}. These outcomes suggest that there is a strong interaction between the interstitial occupancy of fluoride ions, dopant cation size, and lone pair of electrons. The doping of $Ba_{1-x}Sb_xF_{2+x}$ was limited to $x < 0.5$, which is in contrast to the $Ba_{1-x}La_xF_{2+x}$ system, where higher doping like $x = 0.55$ was achieved [82]. This was unexpected considering the fact of smaller size of Sb^{3+} cation (0.76 Å in VI coordination) as comparted to La^{3+} cation (1.02 Å in VI coordination) which should allow a higher doping. This means even with smaller amount of SbF_3 the doping is occupying more interstitial sites of BaF_2 than that required by stoichiometry. This could be due to the effect of lone pair of electrons on Sb^{3+}, which would repel the fluoride ions and force them to occupy more interstitial sites. However, more structural characterizations are needed to demonstrate this hypothesis.

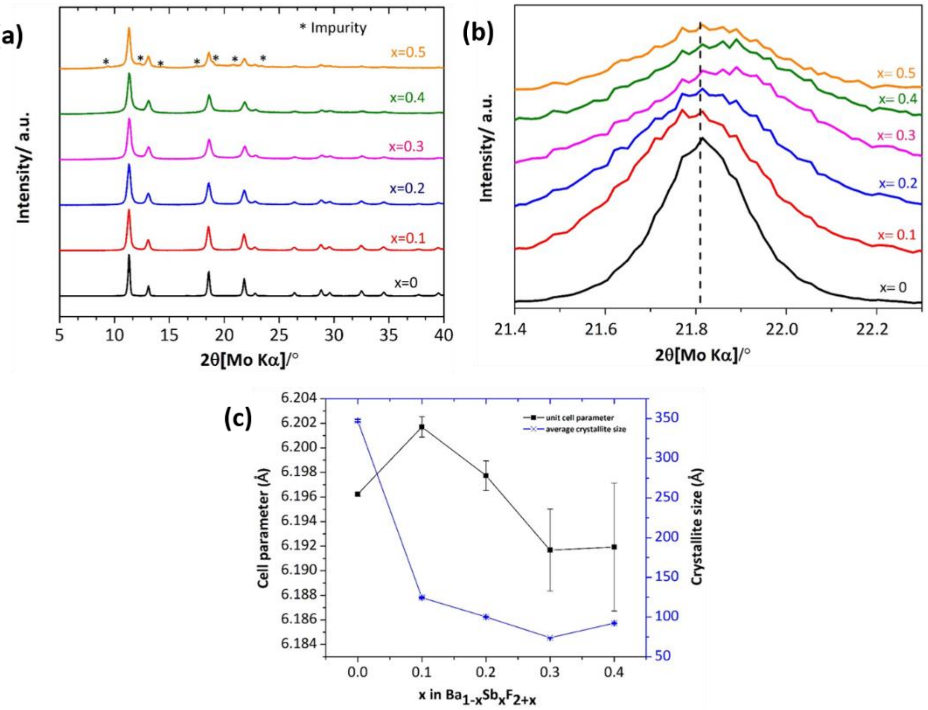

Figure 3.1. *(a) XRD patterns of $Ba_{1-x}Sb_xF_{2+x}$ ($0 \le x \le 0.5$) compounds (b) zooming of the reflection between 21.4 and 22.3 2θ values (c) cell parameter vs. crystallite size value plots of $Ba_{1-x}Sb_xF_{2+x}$ ($0 \le x \le 0.4$). (A modified version of Figure 1 from paper [I].)*

3.1.2 Ionic conductivity study of $Ba_{1-x}Sb_xF_{2+x}$ ($0 \le x \le 0.4$) compounds

Ionic conductivity and the total resistance of $Ba_{1-x}Sb_xF_{2+x}$ ($0 \le x \le 0.4$) compounds were measured using electrochemical impedance spectroscopy (EIS). Impedance spectra were recorded at different temperatures varying from 25 to 200 °C. Figure 3.2 shows the Nyquist plot of $Ba_{0.7}Sb_{0.3}F_{2.3}$ compound along with the corresponding equivalent circuit. The spectrum consists of a half-circle and tilted straight line at high frequency (MHz) and low frequency (Hz), respectively. The half-circle is related to bulk phenomena, whereas the straight line represents the charging of ionic species at the electrolyte−electrode interface [100, 101]. Similar impedance spectra were obtained for all compositions. The equivalent circuit for fitting the spectra is shown in the inset of Figure 3.2. It consists of a parallel assembly of a pure resistance (R1) with a constant phase element (CPE1), which is combined in series with a further constant phase element (CPE2). CPE1 arises from bulk and grain boundaries, whereas CPE2 appears from blocking electrodes. The total resistance (R1) and capacitances were calculated by fitting the impedance spectra with this equivalent circuit [85]. The ionic conductivity of $Ba_{1-x}Sb_xF_{2+x}$ compound was calculated from its total resistance using Equation 1.8. The values of ionic conductivity and equivalent circuit parameters for $Ba_{1-x}Sb_xF_{2+x}$ compounds are given in below Table 3.1.

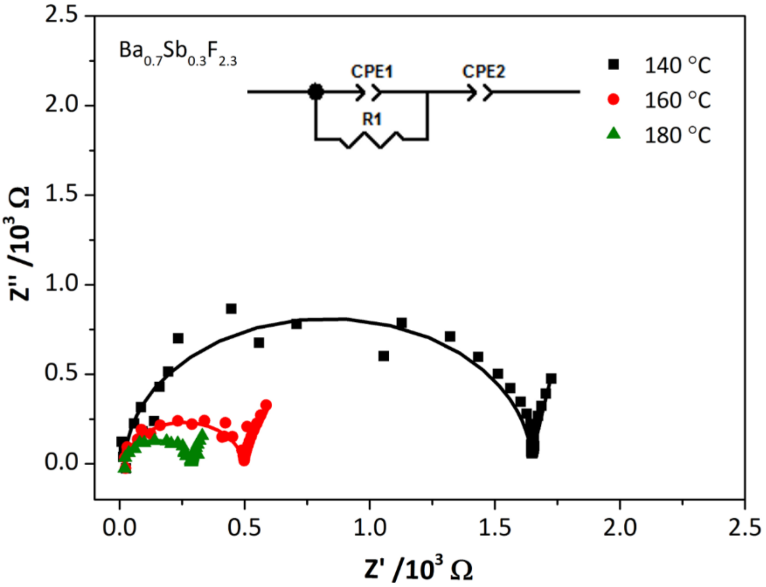

Figure 3.2. *EIS spectra of $Ba_{0.7}Sb_{0.3}F_{2.3}$ compound obtained at different temperatures (symbols) and the corresponding equivalent circuit used for fitting (lines). (A modified version of Figure 4 in paper [I].)*

Figure 3.3 displays the Arrhenius plots for the ionic conductivities of $Ba_{1-x}Sb_xF_{2+x}$ ($0 \le x \le 0.4$) compounds. Activation energies were calculated from the slope of their linear fits using Equation 1.9, values are given in Table 3.1. From Arrhenius plots, it can be observed that the ionic conductivity of $Ba_{1-x}Sb_xF_{2+x}$ compounds increases with the increase of dopant concentration and seem to reach a broad maximum at $0.2 \le x \le 0.4$. The ionic conductivity of $Ba_{0.6}Sb_{0.4}F_{2.4}$ sample is lower than that of $Ba_{0.7}Sb_{0.3}F_{2.3}$ and $Ba_{0.8}Sb_{0.2}F_{2.2}$ at lower temperatures. Whereas, at high temperature, the conductivity of $Ba_{0.8}Sb_{0.2}F_{2.2}$ is lower than that of $Ba_{0.7}Sb_{0.3}F_{2.3}$ and $Ba_{0.6}Sb_{0.4}F_{2.4}$. It seems that doping $x > 0.3$ does not increase the ionic conductivity further, which is in good agreement with structural considerations of interstitial F^- ions trapped in defects clusters [102]. The maximum ionic conductivity was obtained for the $Ba_{0.7}Sb_{0.3}F_{2.3}$ composition, which was 4.4×10^{-4} S·cm^{-1} at 160 °C (Table 3.1). In comparison to isostructural $Ba_{0.7}La_{0.3}F_{2.3}$ ($\sigma_{160\ °C} = 1.55 \times 10^{-4}$ S·cm^{-1}) [82], the ionic conductivity of $Ba_{0.7}Sb_{0.3}F_{2.3}$ is nearly doubling at 160 °C, which suggests that an additional contribution to the conductivity might be possibly introduced by the effect of lone pair electrons on Sb^{3+}. However, the exact role of these lone pairs is not known at moment, further investigations about lone pairs are required.

The impedance spectra of the polycrystalline samples look similar to reported polycrystalline fluorite-type compounds [82, 84, 103]. Here, the change in capacitance value was marginal while the resistance values depended upon sample composition as well as temperature. The capacitance values were almost similar for all compositions and slightly changed with temperature, based on the data extracted from the fits related to the equivalent circuit. For all compositions, capacitance value (CPE1) corresponding to the first semicircle was close to 10^{-10} F, and capacitance value (CPE2) corresponding to the straight line was in the range of 10^{-6}–10^{-5} F (Table 3.1). As expected for polycrystalline fluorite-like compound, the CPE1 value was consistent with grain boundaries phenomena (10^{-11}–10^{-8} F), and CPE2 value was consistent with sample−electrode interfaces phenomena (10^{-7}–10^{-5} F) [104]. In the case of fluorite type compounds, the capacitance corresponding to nano-particle bulk phenomena cannot be observed due to the absence of a second semi-circle which can be described by short-circuiting of bulk resistance by the lower resistance along the grain boundaries. Hence, the bulk contribution is transcended by grain boundaries contribution resulting in only one semicircle. Thus, ionic conductivities of the polycrystalline samples are mostly governed by diffusion of vacancies along the grain boundaries. Based on the data presented in Table 3.1, it can be considered that ionic conductivity of $Ba_{1-x}Sb_xF_{2+x}$ compounds is proceeded by diffusion of vacancies along the grain boundaries.

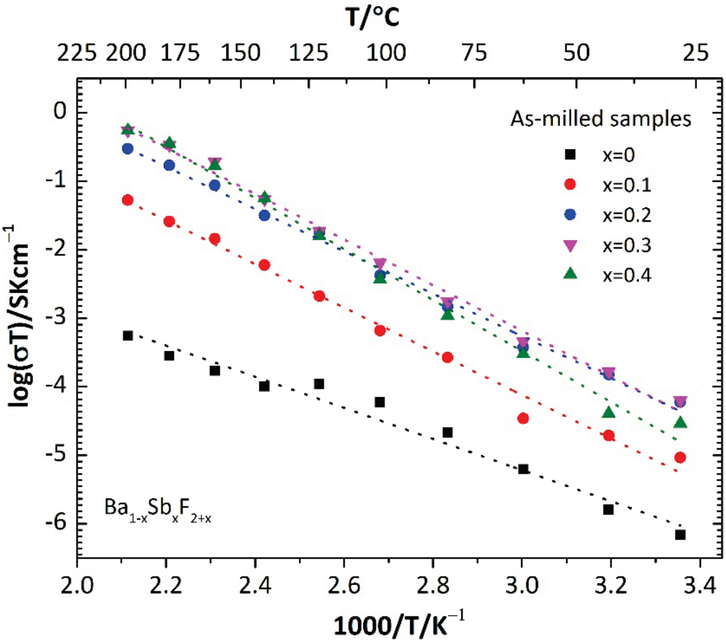

Figure 3.3. *Arrhenius plots of ionic conductivity of $Ba_{1-x}Sb_xF_{2+x}$ ($0 \leq x \leq 0.4$) compounds (symbols) and their fits (dotted lines).*

Table 3.1. *Values of activation energy, ionic conductivity and equivalent circuit parameters for $Ba_{1-x}Sb_xF_{2+x}$ (deviation of 0 to 2).*

Sample	**$Ba_{1-x}Sb_xF_{2+x}$**				
x	0	0.1	0.2	0.3	0.4
$R1_{160\,°C}$ (10^2 Ω)	5393.68	72.9	12.33	4.61	5.97
$σ_{160\,°C}$ (10^{-4} S·cm^{-1})	0.0039	0.333	1.98	4.41	3.89
E_a	0.45	0.63	0.61	0.66	0.73
$CPE1_{160\,°C}$ (10^{-10} F·s^{a-1})	3.52	7.85	2.91	10.78	3.05
$CPE2_{160\,°C}$ (10^{-10} F·s^{a-1})	1.95	4.62	5.83	10.14	31.89

Since the $Ba_{0.7}Sb_{0.3}F_{2.3}$ composition provided the highest ionic conductivity, it was selected to test as cathode material for FIB. Also, theoretical capacity of this compound was estimated to 450 mA·h·g^{-1} (based on SbF_3), which is relatively high in comparison to previously reported cathode compositions like BiF_3 (302 mA·h·g^{-1}) [1]. A FIB cell was constructed using $Ba_{0.7}Sb_{0.3}F_{2.3}$ as a cathode, $La_{0.9}Ba_{0.1}F_{2.9}$ as an electrolyte and Ce as an anode material. Figure 3.4 shows the electrochemical profiles of the cell for the first five cycles. The cell was cycled with a current density of 10 µA·cm^{-2} at a temperature of 150 °C. The cell delivered a first discharge capacity of 301 mA·h·g^{-1} at an average voltage of 1.7 V. This capacity value reaches 66% of the theoretical specific capacity of SbF_3 (450 mA·h·g^{-1}), only about one-thirds of the cathode was not involved in reaction. The first charge capacity amounts to 170 mA·h·g^{-1}, which means only 56% of the initial discharge capacity was recovered. In the following cycles, rapid capacity fading was observed. After 5 cycles, the discharge capacity was reduced to about 80 mA·h·g^{-1}. This considerable capacity fading is probably due to large volume and structural changes in the electrode materials [105].

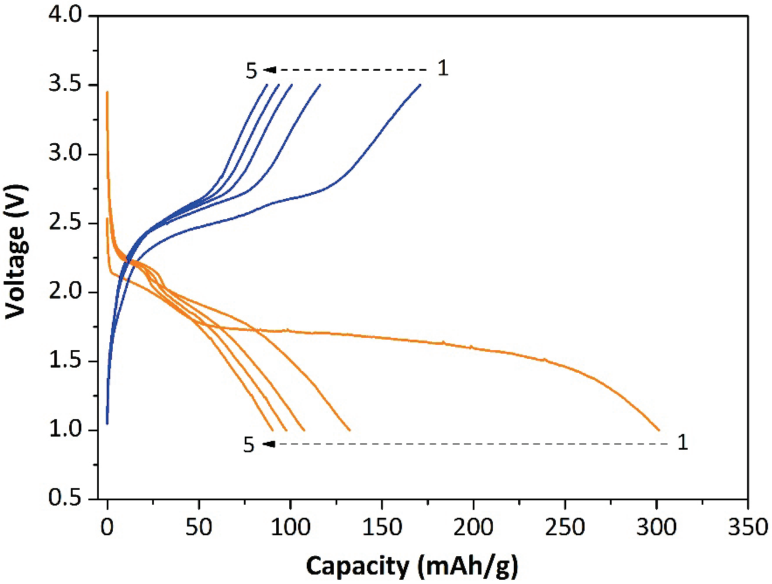

Figure 3.4. *Voltage-composition profiles of $Ba_{0.7}Sb_{0.3}F_{2.3}$/$La_{0.9}Ba_{0.1}F_{2.9}$/Ce cell obtained at 150 ℃ with a current density of 10 µA·cm^{-2}. (A modified version of Figure 7 in paper [I].)*

In summary, SbF_3-doped BaF_2 solid solutions were synthesized by ball milling, and their structural characterization was performed by XRD. All compositions (except x = 0.5) crystallize into pure fluorite-type structure. Their cell parameter and crystallite size values slightly differ from each other. The ionic conductivities of $Ba_{1-x}Sb_xF_{2+x}$ ($0 \leq x \leq 0.4$) solid solutions were studied by EIS. Comparable ionic conductivities were observed for $Ba_{0.7}Sb_{0.3}F_{2.3}$ and $Ba_{0.6}Sb_{0.4}F_{2.4}$ compositions. The $Ba_{0.7}Sb_{0.3}F_{2.3}$ compound shows the highest conductivity of 4.4×10^{-4} S·cm^{-1} at 160 °C. This value is a double of the $Ba_{0.7}La_{0.3}F_{2.3}$ electrolyte. This enhanced ionic conductivity might be due to the effect of lone pair electrons introduced by Sb^{3+}. $Ba_{0.7}Sb_{0.3}F_{2.3}$ was demonstrated as a principally well working cathode material for FIB using $La_{0.9}Ba_{0.1}F_{2.9}$ as solid electrolyte and Ce as anode. The FIB cell exhibited a first discharge and charge capacity of 301 and 170 mA·h·g^{-1}, respectively at 160 °C.

3.2 Demonstration of room temperature rechargeable solid-state FIBs [II]

3.2.1 Structure and ionic conductivity study of $BaSnF_4$ electrolyte

The synthesis of tetragonal (t)-$BaSnF_4$ electrolyte was done by milling BaF_2 and SnF_2, followed up by annealing the composition. After treatment at 300 °C for 2h, the cubic phase (as-milled $BaSnF_4$) fully transformed to the tetragonal phase (Figure 3.5a) with considerable narrowing of the diffraction peaks due to grain growth. The average crystallite size was found to be 25 nm for t-$BaSnF_4$ by Profile Matching refinement. The ionic conductivity of t-$BaSnF_4$ was evaluated by impedance spectroscopy. The complex spectra are displayed as Nyquist plots in Figure 3.5b. The ionic conductivity of the t-$BaSnF_4$ electrolyte was calculated from its total resistance determined by fitting the spectra. The ionic conductivity of t-$BaSnF_4$ was 3.5×10^{-4} S·cm^{-1} at RT, which is consistent with reported value, and is sufficient to apply in RT fluoride ion batteries [92]. Hence, t-$BaSnF_4$ was chosen as solid electrolyte for fabricating solid-state FIBs.

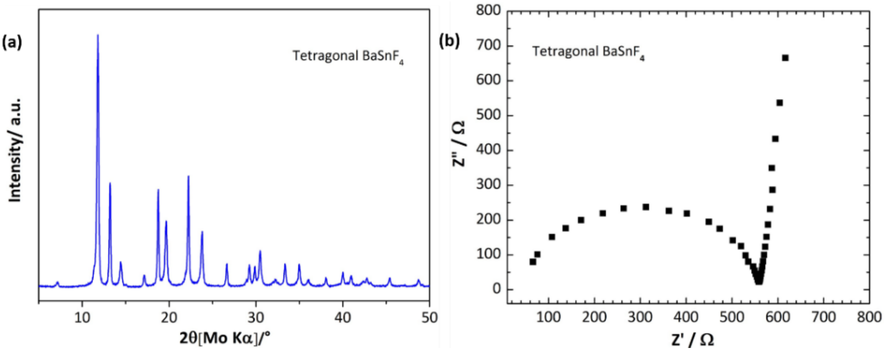

Figure 3.5. *(a) XRD pattern of tetragonal $BaSnF_4$, and (b) Nyquist plot of t-$BaSnF_4$ obtained at 25 ℃. (A modified version of Figure 2 in paper [II].)*

3.2.2 XRD and SEM characterizations of BiF_3, Sn, and Zn composites

BiF_3 was selected as a cathode by virtue of high fluoride ion conductivity, it provides high capacity and promising cycling behavior in the earlier reports [1, 106, 107]. Sn and Zn were expected to have a sufficient, although limited electrochemical stability in contact with $BaSnF_4$ electrolyte and were chosen for cathode. The synthesis of electrode composites is described in the previous experimental section (Table 2.2). Figure 3.6 shows the XRD patterns of t-$BaSnF_4$ and electrode composites (BiF_3, Sn and Zn). For each composite, XRD pattern contains reflexes of t-$BaSnF_4$ and active material peaks. No extra peaks are observable in the XRD patterns of the composite, indicating no chemical reaction occurred between the solid electrolyte and active material during mixing by mechanical milling. Figure 3.7 a-c displays the SEM images of BiF_3, Zn, and Sn composites which show a uniform distribution of electrolyte, active material and CNT. In the SEM images, the average length of CNT in BiF_3 composite was seen relatively larger as compared to the CNT in Sn and Zn composites. Because Sn and Zn composites were prepared using a higher milling speed as compared to BiF_3 composite, breaking of CNT in Sn and Zn cases occurred In the case of Sn composite, bigger particles of Sn were identified and marked with a red square (Figure 3.7c). Cross-sectional SEM measurement was done on a three-layer pellet of FIB and is shown in Figure 3.7d. Typical thicknesses of each FIB component layer were found to be 25, 650 and 85 µm, for cathode, electrolyte and anode respectively.

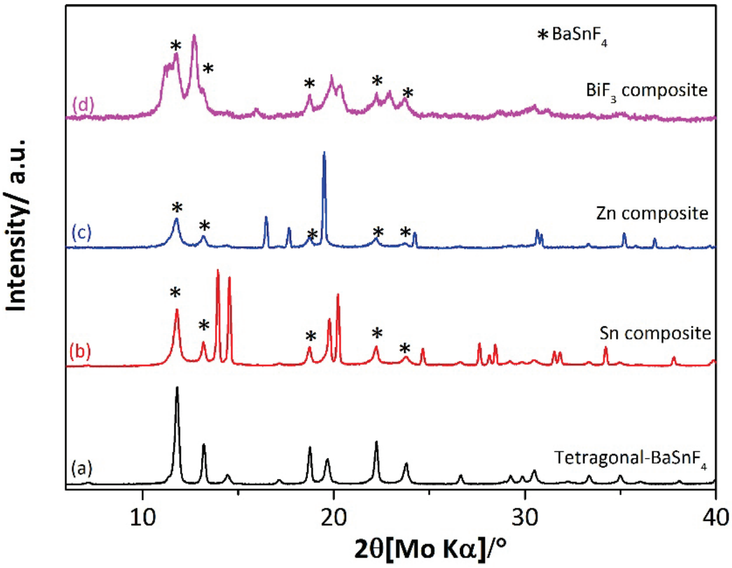

Figure 3.6. XRD patterns of BaSnF$_4$ and electrode composites: (a) Sn, (b) Zn, and (c) BiF$_3$. (A modified version of Figure 3 in paper [II]).

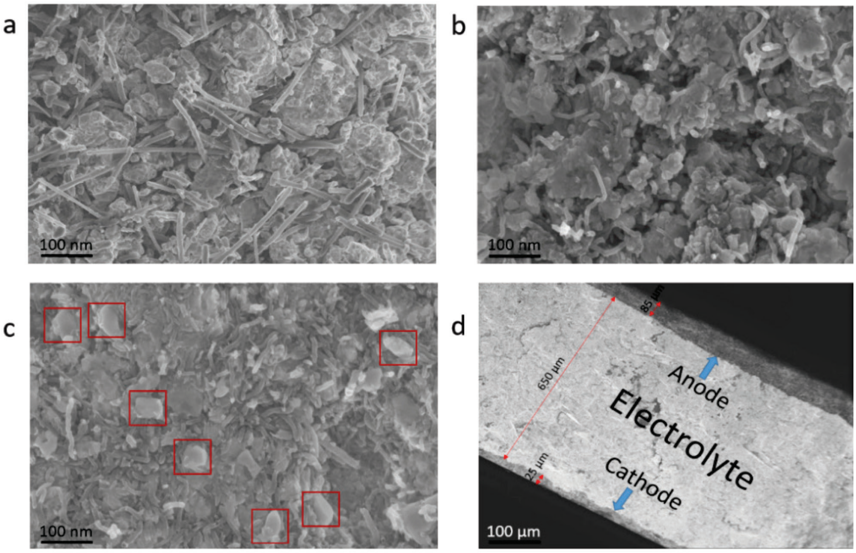

Figure 3.7. SEM images of electrode composites (a) BiF$_3$, (b) Zn, and (c) Sn. (d) cross-sectional view of a FIB cell pellet.

3.2.3 Electrochemical investigation of FIBs

Electrochemical properties of two types of FIB cells (Sn or Zn)/BaSnF$_4$/BiF$_3$ are presented here. The cyclic voltammograms (CVs) of the Sn/BaSnF$_4$/BiF$_3$ cell were scanned in the potential range of 0.05 to 1.2 V at 25 °C (Figure 3.8a). The CV profile consists of a cathodic peak and anodic peak. The cathode peak corresponds to the reduction of BiF$_3$ to Bi metal, whereas the anodic peak represents the oxidation of Bi metal to BiF$_3$. During the first cycle, cathodic and anodic peaks appeared at 0.1 and 0.58 V, respectively. In the subsequent cycle, both peak currents were gradually decreased, and their potentials shifted to the positive direction. However, the appearance of cathode and anode peaks indicates that bismuth fluoride reversibly reduces and oxidizes in the Sn/BaSnF$_4$/BiF$_3$ FIB cell. Galvanostatic discharge-charge was carried out at various temperatures. The cell, operated at 25 °C, delivered the first discharge capacity of 120 mA·h·g^{-1} (Figure 3.8b). This value is 40% of the theoretical specific capacity of BiF$_3$ (302 mA h g^{-1}), indicating incomplete reaction occurred at the cathode. The first charge capacity was 80 mA·h·g^{-1}, which is 66% of initial discharge capacity (120 mA·h·g^{-1}) and the following discharge/charge cycles capacities faded quickly. After 4 cycles, the discharge capacity reduced to 30 mA·h·g^{-1}. The capacity fading is a well-known phenomenon of conversion electrodes, where conversion reaction occurs during charge-discharge process [105, 108, 109]. It can be attributed to the volume changes in the electrode materials during charge-discharge process.

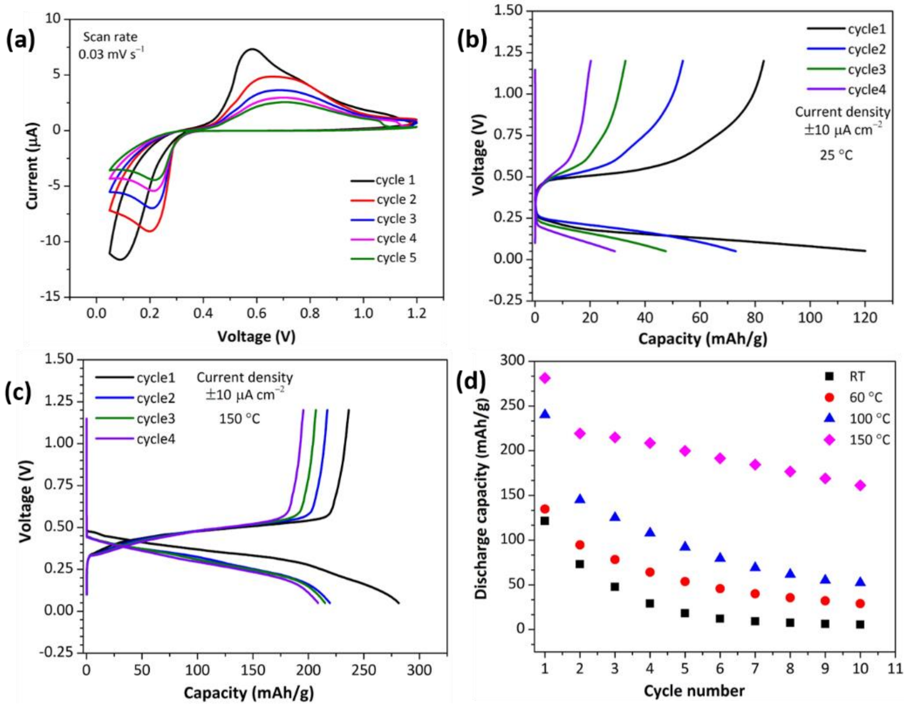

Figure 3.8. *Electrochemical analysis of Sn/BaSnF$_4$/BiF$_3$ cells. (a) Cyclic voltammogram profiles obtained at 25 ℃. Voltage-composition profiles obtained at (a) 25, and (e) 150 ℃. (f) Cycling performances obtained at different temperatures. (A modified version of Figure 5 in paper [II].)*

The large volume changes may weaken the electrode and electrolyte contact, resulting in an increase of the electrode−electrolyte interfacial resistance [110]. Nevertheless, a feasibility of room-temperature rechargeable solid-state fluoride battery was demonstrated. To study the Sn/$BaSnF_4$/BiF_3 system in detail, the cells were cycled at elevated temperatures such as 60, 100, and 150 °C. The cell operation at 150 °C delivered the highest discharge capacity of 281 mA·h·g^{-1} at the first cycle, which is 93% of theoretical specific capacity (302 mA·h·g^{-1}), see Figure 3.8c. The first charge capacity was 231 mA·h·g^{-1}, meaning 82% of initial capacity could be recovered. Since cycling at 25, 60, and 100 °C showed measurably inferior performance (Figure 3.8d), this system constitutes a promising future testbed.

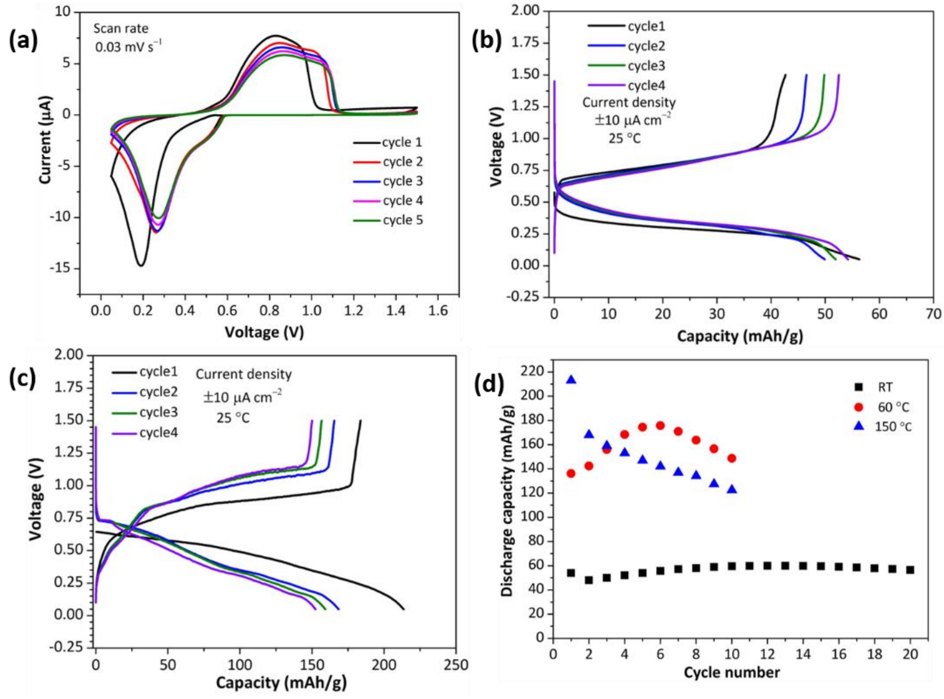

Figure 3.9. *Electrochemical analysis of Zn/$BaSnF_4$/BiF_3 cells. (a) Cyclic voltammogram profiles obtained at 25 ℃. Voltage-composition profiles obtained at (b) 25, and (c) 150 °C. (d) Cycling performances obtained at different temperatures. (A modified version of Figure 6 in paper [II].)*

The electrochemical results on the second system, Zn/$BaSnF_4$/BiF_3 cell are displayed in Figure 3.9. Similar to the Sn based FIB system, the CV profile of Zn/$BaSnF_4$/BiF_3 consists of cathodic and anodic peak confirming the reduction of BiF_3 and oxidation of Bi, respectively (Figure 3.9a). The current related to cathodic and anodic peaks decayed gradually with increasing cycle number, but not nearly as much as in Sn case. The electrochemical charge-discharge profiles of Zn/$BaSnF_4$/BiF_3 cells were obtained at temperatures of 25, 60, and 150 °C. The cell at 25 °C exhibits a first discharge and charge capacity of 56 and 43 mA·h·g^{-1}, respectively (Figure 3.9b). Here, the discharge capacity was considerably less than the theoretical capacity of BiF_3 (302 mA·h·g^{-1}), representing incomplete reaction occurred. In contrast to Sn based cell, the Zn system delivered low discharge capacity. At subsequent discharging and charging, capacities were found to increase slightly. After 20 cycles the discharge capacity reached about 61 mA·h·g^{-1}. This is in contrast to the rapid capacity fading observed with the Sn based cell. It seems with increased cycling number more Zn material is getting activated contributing to the capacity. The cells showed also very stable cycling. When the Zn cell cycled at 150 °C, the first discharge and charge capacity raised to 213 and 183 mA·h·g^{-1}, respectively (Figure 3.9c). Despite applying a relatively high current (4 times higher than 25 °C) at 150 °C, it delivered the maximum capacity for the Zn based cell. Unlike the 25 °C case, no increase in capacity was observed by follow up cycles. High temperature (150 °C) obviously led to the activation of Zn particles with no further increase of capacity with cycling. Similar to Sn case, the cyclic performance of cell improves when temperature increases (Figure 3.9d). This could be due to an increase in ionic conductivity of all battery components at higher temperatures and decrease of resistance of the electrode–electrolyte interface. At high temperature, fast movement of electrons and ions make sufficient contact with active materials by mass and/or electron transfer, which increases the utilization of active material, increasing the capacity. Also, the low interfacial resistance at high temperature facilitates further fluoride transfer across the electrode-electrolyte interface, adding to the reactivity of active material and capacity.

3.2.4 Ex-situ investigation of Sn/$BaSnF_4$/BiF_3 and Zn/$BaSnF_4$/BiF_3 cells

To understand the mechanism of conversion reaction at electrodes, ex-situ XRD measurements were carried out on three-layer pellets before and after discharge. The Zn/$BaSnF_4$/BiF_3 cell was discharged at 150 °C applied for recording the XRD pattern. Figure 3.10a shows XRD patterns of cathode side (BiF_3) of the pellet before and after discharge. Before discharge, BiF_3 and t-$BaSnF_4$ phases were clearly observed. After discharge, BiF_3 peaks vanished, indicating a complete reaction. In the pattern, new peaks appeared which can be attributed to Bi metal verifying the reduction of BiF_3 to Bi (Figure 3.10a). XRD patterns of anode side (Zn) of the pellet (Zn/$BaSnF_4$/BiF_3) before and after discharge are shown in Figure 3.10b. Before discharge, peaks corresponding to Zn and t-$BaSnF_4$ were observed. After discharge, new peaks appeared (marked with +), which were indexed to the ZnF_2 phase, demonstrating the oxidation of Zn metal at the anode (Figure 3.10b). In the XRD pattern, peaks corresponding to Zn phase were seen after discharge, meaning an excess amount of Zn was used.

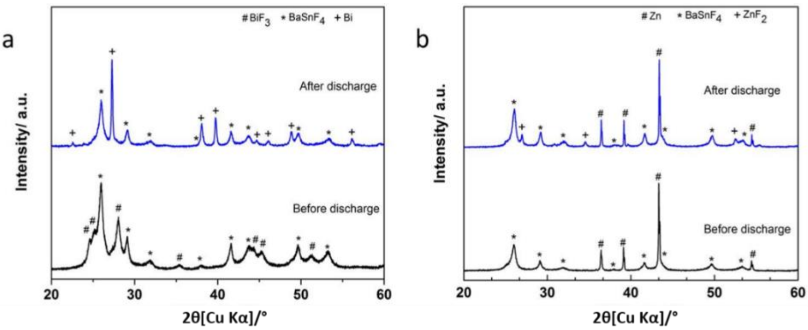

Figure 3.10. *XRD patterns of Zn/$BaSnF_4$/BiF_3 battery pellet before and after discharge (a) BiF_3 side and (b) Zn side (A modified version of Figure 8 in paper [II]).*

To see the morphological changes at electrode surfaces during cycling, ex-situ SEM experiments were carried out on the three-layer pellet before and after discharge.

To perform SEM measurements, Sn/$BaSnF_4$/BiF_3 and Zn/$BaSnF_4$/BiF_3 discharged and charged cells at 150 °C were prepared. SEM images of the Sn anodes from pristine to second discharge (including first charge and discharge) are given in Figure 3.11a-d. SEM image of the pristine Sn composite consists of pyramid-shaped particles which correspond to Sn metal Figure 3.11a). After first discharge, tetragonal-shaped particles were observed at the surface which can be attributed to the formation of SnF_2 (Figure 3.11b). Spherical types of particles at different sizes were observed after the first charge, indicating the morphological changes at the surface (Figure 3.11c). After second discharge the tetragonal shaped crystals re-appeared, which demonstrates the structural changes of particles at Sn electrode during cycling (Figure 3.11d). SEM images of Zn anode before and after discharge looked very similar to each other (Figure 3.11e,f). Unlike Sn electrode, Zn crystals were not visible in the pristine state of Zn electrode. After discharge, similar morphology was observed in comparison to the pristine state. This suggests that Zn and the oxidized ZnF_2 particles are not as large as in the case of Sn-SnF_2, which could be the reason for better reversibility of Zn/$BaSnF_4$/BiF_3 as compared to the Sn/$BaSnF_4$/BiF_3 system. The bigger particles can lead to delamination of elecronic and ionic additives from active materials degrading the performance of cell.

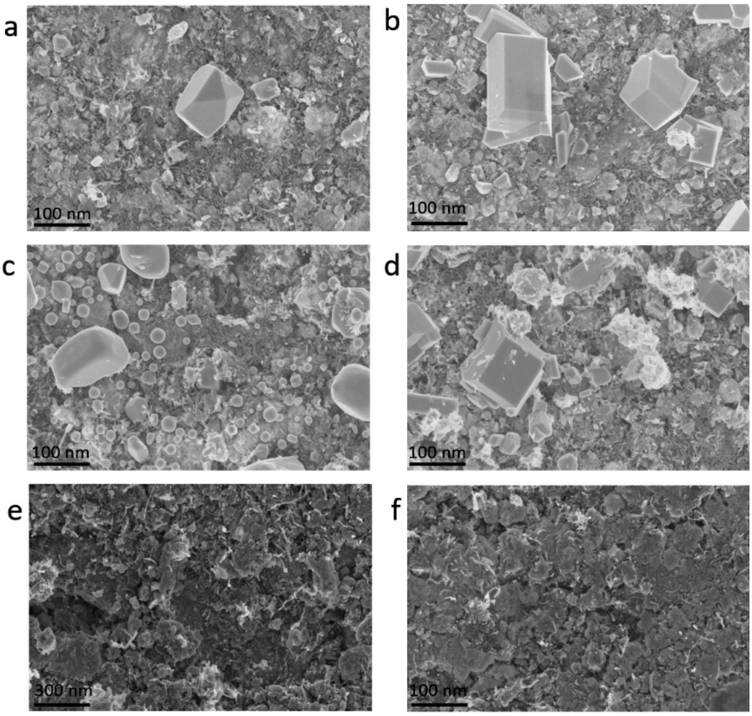

Figure 3.11. SEM images of Sn side of Sn/$BaSnF_4$/BiF_3 battery pellet (a) pristine state, (b) after first discharge, (c) after the first charge, (d) after second discharge. SEM images of Zn anode: (e) pristine state and (f) after discharge.

To summarize this section, room temperature rechargeable solid-state FIBs were demonstrated by using $BaSnF_4$ as solid electrolyte. The structural and morphological characterizations of electrodes and electrolyte were done by XRD and SEM techniques.

The ionic conductivity of the electrolyte was evaluated by EIS. The high ionic conductivity of polycrystalline t-$BaSnF_4$ enabled the demonstration of RT-FIBs. Two types of FIB systems such as Sn/$BaSnF_4$/BiF_3 and Zn/$BaSnF_4$/BiF_3 were fabricated and their electrochemical properties investigated at different temperatures ranging from 25 to 150 °C. Mostly, the current density of 10 $\mu A \cdot cm^{-2}$ was applied on FIB cells to perform discharge and charge process. At RT, the Sn/$BaSnF_4$/BiF_3 cell delivered a first discharge capacity of 120 $mA \cdot h \cdot g^{-1}$, whereas Zn/$BiSnF_4$/BiF_3 cell exhibited a first discharge capacity of 56 $mA \cdot h \cdot g^{-1}$. The cells delivered low average voltage due to the low voltage redox couples (Sn/BiF_3 and Zn/BiF_3). The Sn based cells showed high capacity, but rapid capacity fading upon cycling. On the other hand, Zn based cells displayed less first capacity but better cycling performance. The rapid capacity fading in the case of Sn might be due to the increase of cell resistance during cycling and the large particle size of Sn. Ex-situ XRD and SEM measurements were performed on electrodes before and after charge in order to understand the reaction mechanism.

3.3 Introducing interlayer electrolytes concept for solid-state FIBs [III]

3.3.1 Structure and ionic conductivity study of $La_{0.9}Ba_{0.1}F_{2.9}$ and $BaSnF_4$

XRD patterns with corresponding refinements of poly crystalline $La_{0.9}Ba_{0.1}F_{2.9}$ and $BaSnF_4$ compound are shown in Figure 3.12. For $La_{0.9}Ba_{0.1}F_{2.9}$, all peaks corresponding to a tysonite-type phase were observed, confirming the formation of a solid solution (Figure 3.12a). In the XRD pattern of $BaSnF_4$, reflections corresponding to the tetragonal phase were observed (Figure 3.12b). This indicates that cubic $BaSnF_4$ was fully transformed into its tetragonal phase by annealing. The average crystallite size of $La_{0.9}Ba_{0.1}F_{2.9}$ and t-$BaSnF_4$ was 12 and 20 nm determined by profile matching. These values are in good agreement with the earlier reports [84, 92]. The ionic conductivity and activation energy of $La_{0.9}Ba_{0.1}F_{2.9}$ and t-$BaSnF_4$ were measured using EIS. The ionic conductivity of $La_{0.9}Ba_{0.1}F_{2.9}$ and t-$BaSnF_4$ was 4×10^{-7} and 3.5×10^{-4} $S \cdot cm^{-1}$ at 25 °C, respectively. The activation energy (E_a) calculated for $La_{0.9}Ba_{0.1}F_{2.9}$ and $BaSnF_4$ was 0.48 and 0.34 eV, respectively. These values for both compounds were close to reported values [84, 92].

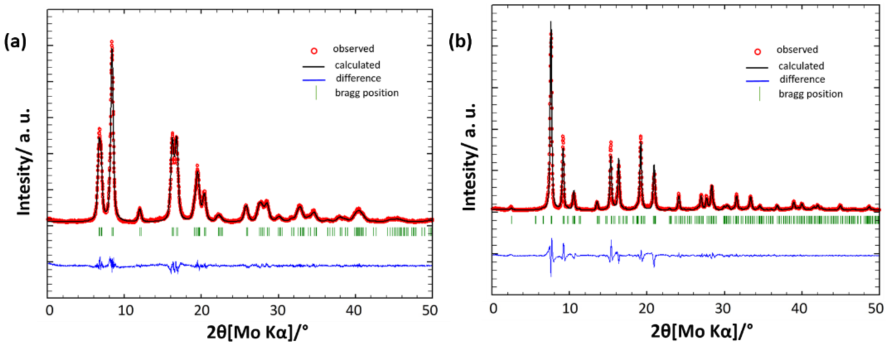

Figure 3.12. *Profile matched XRD patterns of (a) $La_{0.9}Ba_{0.1}F_{2.9}$ and (b) tetragonal $BaSnF_4$ (A modified version of Figure 1 in paper [III]).*

3.3.2 SEM and EDX analysis of Interlayer Electrolytes

Interlayer electrolyte pellets were prepared by uniaxial pressing $La_{0.9}Ba_{0.1}F_{2.9}$ and $BaSnF_4$ layers together using a desktop press. Figure 3.13 shows the cross-sectional SEM image and EDX maps obtained for inter-layer electrolyte pellet ($La_{0.9}Ba_{0.1}F_{2.9}$ (20 mg)/$BaSnF_4$ (120 mg)). The cross-sectional SEM image measured the thickness of each layer of interlayer electrolytes. The thickness of 90 µm and 650 µm was obtained for the $La_{0.9}Ba_{0.1}F_{2.9}$ and $BaSnF_4$ layer, respectively (Figure 3.13a). Also, SEM shows that both layers stick uniformly to each other, which is necessary for ion diffusion. Represented EDX maps show that the F element is distributed across the pellet (Figure 3.13b), while Sn and La are observed in respective layers (Figure 3.13c,d). Further, SEM image and EDX maps show that $La_{0.9}Ba_{0.1}F_{2.9}$ and $BaSnF_4$ layers did not intermix while preparing the pellet by pressing.

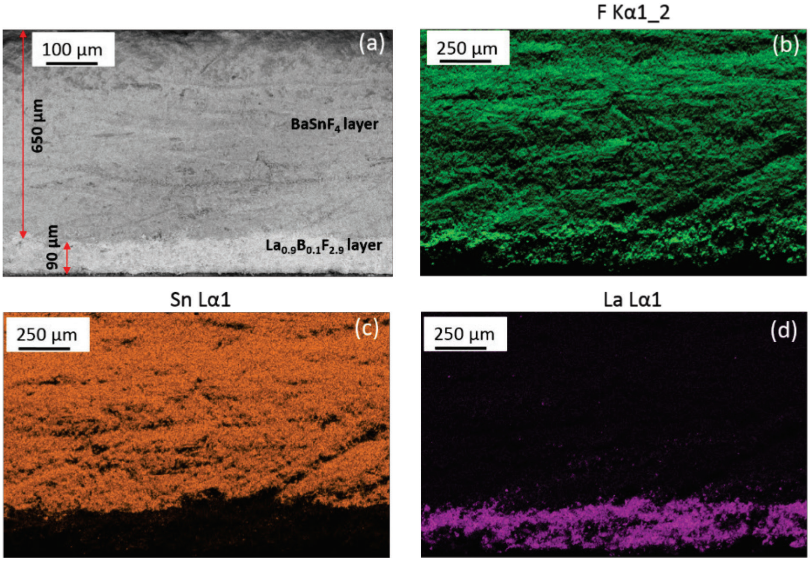

Figure 3.13. *Cross-sectional SEM image (a) of $La_{0.9}Ba_{0.1}F_{2.9}$ (20 mg)/$BaSnF_4$ (120 mg) pellet and its EDX maps (b–d) of F, Sn, and La.*

3.3.3 Ionic conductivity study of interlayer electrolytes

The ionic conductivities of interlayer electrolytes were analyzed using EIS. To perform EIS measurements, three interlayer pellets were prepared using different amounts of $La_{0.9}Ba_{0.1}F_{2.9}$ component such as 70, 20, and 10 mg. Figure 3.14a,b show the Nyquist plots of $La_{0.9}Ba_{0.1}F_{2.9}$ (70 mg)/$BaSnF_4$ (70 mg), $La_{0.9}Ba_{0.1}F_{2.9}$ (20 mg)/$BaSnF_4$ (120 mg), and $La_{0.9}Ba_{0.1}F_{2.9}$ obtained at 25 °C. For all the electrolytes, similar impedance spectra were observed. The plotted data can be characterized by a depressed semicircle at high frequency and a tilted straight line at low frequency. The semicircle is attributed to the combined contribution of both the bulk and grain boundary phenomena, and a straight line corresponds to electrode/electrolyte interface phenomena [104]. For the interlayer electrolyte, the impedance spectra are expected to exhibit two semicircles corresponding to $BaSnF_4$ and $La_{0.9}Ba_{0.1}F_{2.9}$ layers. Also, no semicircle was observed for the interface of $BaSnF_4$ and $La_{0.9}Ba_{0.1}F_{2.9}$ layers, indicating no significant resistance across the interface.

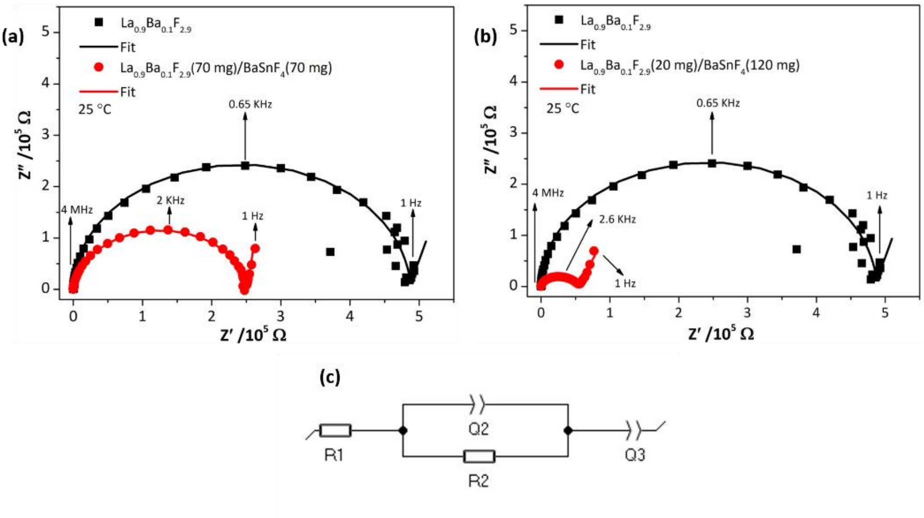

__Figure 3.14.__ Nyquist plots (symbols) and the corresponding fit (lines) of (a) $La_{0.9}Ba_{0.1}F_{2.9}$ (70 mg)/$BaSnF_4$ (70 mg) and $La_{0.9}Ba_{0.1}F_{2.9}$, and (b) $La_{0.9}Ba_{0.1}F_{2.9}$ (20 mg)/$BaSnF_4$ (120 mg) and $La_{0.9}Ba_{0.1}F_{2.9}$ are shown. In (c) the equivalent circuit used to fit the EIS spectra is depicted (A modified version of Figure 4 in paper [III]).

__Table 3.2.__ Values of Ionic conductivity and fitting parameters of the Nyquist plots obtained at 25 °C for $La_{0.9}Ba_{0.1}F_{2.9}$, and $La_{0.9}Ba_{0.1}F_{2.9}$ (70 or 20 mg)/$BaSnF_4$ (70 or 120 mg) (deviation 0 to 2).

Sample	**$La_{0.9}Ba_{0.1}F_{2.9}$**	**$La_{0.9}Ba_{0.1}F_{2.9}$ (70 mg)/$BaSnF_4$ (70 mg)**	**$La_{0.9}Ba_{0.1}F_{2.9}$ (20 mg)/$BaSnF_4$ (120 mg)**
R2 (10^3 Ω)	75.91	244.54	57.79
σ (10^{-4} S·cm^{-1})	0.004	0.008	0.035
Q2 (10^{-9} F·s^{a-1})	5.62	0.283	63.39
Q3 (10^{-6} F·s^{a-1})	5.21	2.67	3.38

R2 corresponds to total resistance (bulk and grain boundary). Q2 and Q3 represent capacitance associated with R2 (either bulk or grain boundary), and capacitance of the blocking electrodes, respectively.

From the Nyquist plots it can be observed that the diameter of semicircle for $La_{0.9}Ba_{0.1}F_{2.9}$ (70 mg)/$BaSnF_4$ (70 mg) electrolyte is smaller than that of pure $La_{0.9}Ba_{0.1}F_{2.9}$ electrolyte (Figure 3.14a). In the case of $La_{0.9}Ba_{0.1}F_{2.9}$ (20 mg)/$BaSnF_4$ (120 mg), the diameter of semicircle becomes much smaller compared to pure $La_{0.9}Ba_{0.1}F_{2.9}$ (Figure 3.14b). This correlates resistance with $La_{0.9}Ba_{0.1}F_{2.9}$-layer thickness. The ionic conductivity of electrolyte was calculated from its total resistance (R2) determined by fitting the spectrum with equivalent circuit (Figure 3.14c). The values of Ionic conductivity and fitting parameters of the Nyquist plots for interlayer and $La_{0.9}Ba_{0.1}F_{2.9}$ electrolytes are given in the above Table 3.2. The ionic conductivity of the $La_{0.9}Ba_{0.1}F_{2.9}$ (70 mg)/$BaSnF_4$ (70 mg) was found to be 0.8×10^{-6} S·cm^{-1} at 25 °C, which is twice than that of pure $La_{0.9}Ba_{0.1}F_{2.9}$ (0.4×10^{-6} S·cm^{-1}). The calculated ionic conductivity of $La_{0.9}Ba_{0.1}F_{2.9}$ (20 mg)/$BaSnF_4$ (120 mg) was 0.35×10^{-5} S·cm^{-1} at 25 °C, which is about 10 times better than compared to that of pure $La_{0.9}Ba_{0.1}F_{2.9}$. On fitting the Nyquist plot, the capacitances associated with Q2 and Q3 were in the range of 10^{-8}–10^{-10} and 10^{-6} F, respectively (Table 3.2). Based on these values, the semicircle (high frequency) can be attributed to the grain boundaries phenomena (10^{-11}–10^{-8} F), whereas the straight line corresponds to the electrolyte−electrode interface phenomena (10^{-7}–10^{-5} F) [104].

To further enhance the ionic conductivity of the interlayer electrolyte, $La_{0.9}Ba_{0.1}F_{2.9}$ amount was reduced to 10 mg. Figure 3.15a-c illustrates the Nyquist plots of $La_{0.9}Ba_{0.1}F_{2.9}$ (10 mg)/$BaSnF_4$ (130 mg) electrolyte obtained at 25, and 150 °C. Similar impedance profiles were observed at the all temperatures, but they were considerably different compared to spectra obtained from interlayer electrolyte pellets containing a higher amount of $La_{0.9}Ba_{0.1}F_{2.9}$ (20 or 70 mg) (Figure 3.14). In the 10 mg case, the Nyquist plot consists of two depressed semicircles (at high and intermediate frequency) and a tilted straight line (at low frequency). The equivalent circuit used for fitting the data is given in Figure 3.15c. The ionic conductivity of this thinner interlayer electrolyte was calculated from its total resistance (R2+R3) contributed from bulk, grain boundary, and interface. The total resistance of interlayer electrolyte was determined by fitting impedance spectra with the corresponding equivalent circuit. The values of ionic conductivities and fitting parameters of Nyquist plots for $La_{0.9}Ba_{0.1}F_{2.9}$ (10 mg)/$BaSnF_4$ (130 mg) are provided in below Table 3.3. The conductivity value increases significantly when rising the temperature. The total ionic conductivity of $La_{0.9}Ba_{0.1}F_{2.9}$ (10 mg)/$BaSnF_4$ (130 mg) electrolyte was found to be 0.89×10^{-5} S·cm^{-1} at 25 °C, which is approximately 22 times higher compared to $La_{0.9}Ba_{0.1}F_{2.9}$ (4×10^{-7} S·cm^{-1} at 25 °C). This value is sufficient for demonstrating RT high potential solid-state FIBs. At 60 °C, related ionic conductivity reached to 2.8×10^{-4} S·cm^{-1}, which is close to the room temperature conductivity of pure $BaSnF_4$ (3.5×10^{-4} S·cm^{-1}).

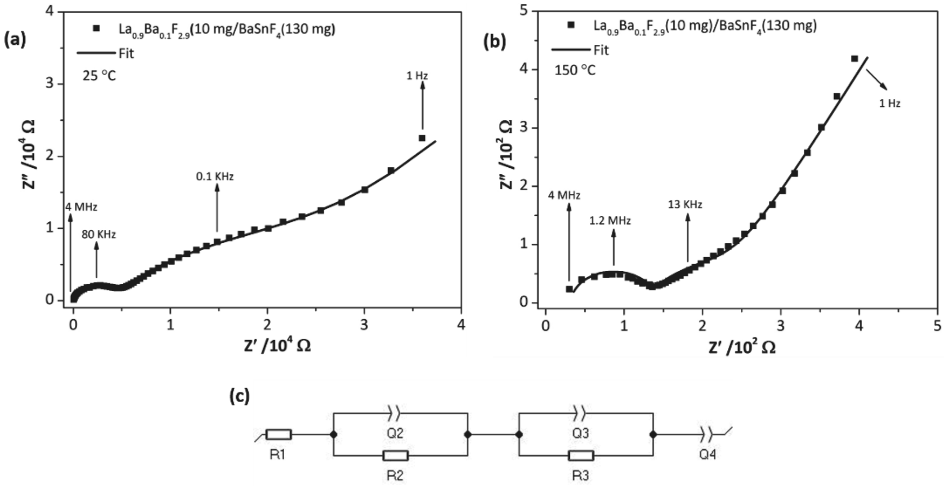

Figure 3.15. *Nyquist plots (symbols) and corresponding fit (line) for $La_{0.9}Ba_{0.1}F_{2.9}$ (10 mg)/$BaSnF_4$ (130 mg) electrolyte obtained at (a) 25 ℃ and (b) 150 ℃ are given. In (c) the equivalent circuit used to fit the EIS spectra is shown (A modified version of Figure 5 in paper [III]).*

From data fitting, the capacitances associated with Q2 and Q3 were in the range of 10^{-9} and 10^{-6} F, respectively, and the capacitance related to Q4 was in the range of 10^{-6} F (Table 3.3), which is consistent with electrolyte-electrode phenomena [104]. Based on the values of Q2 and Q3, the first semi-circle (at high frequency) was ascribed to the grain boundary and second semi-circle (intermediate frequency) was assigned to the interfacial contribution. The appearance of this second circle indicates that the interfacial resistance contribution was not suppressed here unlike to the $La_{0.9}Ba_{0.1}F_{2.9}$ (70 or 20 mg)/$BaSnF_4$ (70 or 120 mg) case. According to capacitance values, it becomes evident that the contribution from interfacial resistance becomes more noticeable as the thickness of the $La_{0.9}Ba_{0.1}F_{2.9}$ electrolyte is reduced.

Table 3.3. *Values of ionic conductivity and fitting parameters of Nyquist plots for $La_{0.9}Ba_{0.1}F_{2.9}$ (10 mg)/$BaSnF_4$ (130 mg) are given (deviation 0 to 2).*

Sample	**$La_{0.9}Ba_{0.1}F_{2.9}$ (10 mg)/$BaSnF_4$ (130 mg)**			
Temperature	25 °C	60 °C	100 °C	150 °C
R2+R3 (10^3 Ω)	23.38	1.16	0.51	0.09
σ (10^{-4} S·cm^{-1})	0.089	1.80	4.00	23.90
Q2 (10^{-9} F·s^{a-1})	0.98	1.01	1.31	2.10
Q3 (10^{-6} F·s^{a-1})	0.72	0.44	1.44	2.22
Q4 (10^{-6} F·s^{a-1})	3.95	5.06	6.24	6.70
R2 and R3 correspond to total resistance (bulk and grain boundary) and interfacial resistance respectively. Q2, Q3, and Q4 represent capacitance associated with R2 (bulk and grain boundary), R3 (interface), and the blocking electrodes, respectively.				

3.3.4 FIB cell assembly and testing

To demonstrate the compatibility of interlayer electrolyte with high electropositive metal like Ce, a FIB cell was built using $La_{0.9}Ba_{0.1}F_{2.9}$ (20 mg)/$BaSnF_4$ (120 mg) as an electrolyte, BiF_3 as a cathode, and Ce as an anode. Battery pellet was fabricated by pressing Ce, $La_{0.9}Ba_{0.1}F_{2.9}$, $BaSnF_4$, and BiF_3 layer together using a desktop press. The voltage-composition profiles of Ce/$La_{0.9}Ba_{0.1}F_{2.9}$/$BaSnF_4$/BiF_3 cell are shown in Figure 3.16a. The cell shows an open circuit voltage of 2.6 V at room temperature. The cell delivered a first discharge capacity of 27 mA·h·g^{-1} at an average voltage of 1.4 V. The first charge capacity amounts to 23 mA·h·g^{-1} at an average voltage of 1.7 V. During the second or subsequent cycle, the discharge and charge profiles show high average voltage plateau. In the following cycling, quick capacity fading was observed, resulting in 3 mA·h·g^{-1} after five cycles (Figure 3.16a). The possible reason for getting low capacity and reduced performance is due to insufficient ionic conductivity of anode and electrolyte at RT.

Figure 3.16b shows voltage-composition profiles of the Ce/$BaSnF_4$/BiF_3 cell obtained at RT. The OCV of Ce/$BaSnF_4$/BiF_3 was around 1.2 V, which is 2.4 V less than that of interlayer electrolyte-based FIB. During discharge, cell voltage immediately dropped to 0 V with almost zero capacity. The reason for obtaining low OCV and immediate voltage drop is due to direct contact between Ce and $BaSnF_4$. The interfacial reaction between Ce and $BaSnF_4$ would result into formation of CeF_3, BaF_2, and Sn at Ce/$BaSnF_4$ interface.

Despite low capacity, relatively high potential FIBs working at RT was demonstrated employing interlayer electrolyte. The feasibility of RT-FIB with high electropositive anode like Ce was not possible either using $La_{0.9}Ba_{0.1}F_{2.9}$ or $BaSnF_4$ electrolyte This is due to the low ionic conductivity (RT) of $La_{0.9}Ba_{0.1}F_{2.9}$ electrolyte or limited electrochemical stability of $BaSnF_4$ electrolyte. The low ionic conductivity and electrochemical stability issues were resolved by combining $La_{0.9}Ba_{0.1}F_{2.9}$ and $BaSnF_4$ electrolytes.

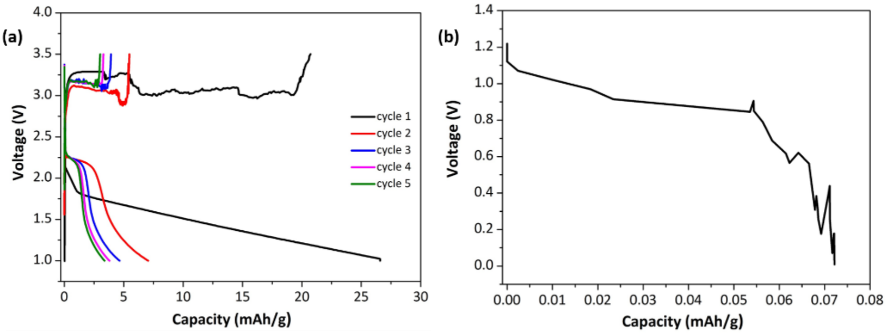

***Figure 3.16**. Voltage-composition profiles of (a) Ce/$La_{0.9}Ba_{0.1}F_{2.9}$/$BaSnF_4$/BiF_3 and (b) Ce/ $BaSnF_4$/BiF_3 cells obtained at 25 ℃ with a current density of ±10 μA·cm^{-2} (A modified version of Figure 7 in paper [III]).*

To sum up, the concept of interlayer electrolytes for FIBs was introduced, which enabled the demonstration of rechargeable high potential solid-state FIB performance at a room temperature. The interlayer electrolyte consisted of a thin layer of $La_{0.9}Ba_{0.1}F_{2.9}$ and thick layer of $BaSnF_4$ electrolyte. The interlayer electrolyte was achieved by pressing thin $La_{0.9}Ba_{0.1}F_{2.9}$ and thick $BaSnF_4$ layers together using desktop pellet press. Applying a very thin layer of $La_{0.9}Ba_{0.1}F_{2.9}$, the total conductivity of the interlayer electrolyte was significantly increased while it physically isolated the less stable and highly conductive electrolyte ($BaSnF_4$) from the anode (Ce). The total ionic conductivity of the interlayer electrolyte was optimized by varying the thickness of the $La_{0.9}Ba_{0.1}F_{2.9}$ layer. The interlayer electrolyte containing thinner $La_{0.9}Ba_{0.1}F_{2.9}$ layer (45 μm) shows high ionic conductivity of 0.89×10^{-5} S·cm^{-1} at RT, which is more than one order of magnitude higher compared to the pure $La_{0.9}Ba_{0.1}F_{2.9}$ (0.4×10^{-6} S·cm^{-1}). EIS, cross-sectional SEM, and EDX measurements were performed on interlayer electrolytes to determine the conductivity, layer thickness, and elemental mapping, respectively.

3.4 Testing Mg as an anode against BiF_3 and SnF_2 cathodes for RT-FIBs [IV].

3.4.1 Electrochemical investigation of FIB cells employing $LiPF_6$ electrolyte

Two types of FIB cells such as Mg+MgF_2/$LiPF_6$/BiF_3 and Mg+MgF_2/$LiPF_6$/SnF_2 were constructed. Cyclic voltammogram (CV) profiles of Mg+MgF_2/$LiPF_6$/BiF_3 cell obtained at 25 °C are given in the Figure 3.17a. During first scan in the negative direction (from 3 to 0 V), the cathodic peak was observed at around 1.0 V, which correspond to the reduction of BiF_3 into Bi metal. In the following cycles, the peak currents were gradually decreased, and their potential shifted to lower values. During scan from 0 to 3 V, the anodic peak was observed at around 2.5 V, corresponds to the oxidation of Bi metal into BiF_3. In the following cycles, the anodic current decreased and potential shifted in positive direction. The decrease and potential shift of anodic current with cycling could correspond to the loss of active material. Nevertheless, the peaks of CV profiles demonstrated the reversible oxidation and reduction of BiF_3 in Mg+MgF_2/$LiPF_6$/BiF_3 cell. Figure 3.17b shows galvanostatic discharge−charge curves of Mg+MgF_2/$LiPF_6$/BiF_3 cell obtained at 25 °C with current density of 38 μA·cm^{-2}. The first discharge capacity amounts to 142 mA·h·g^{-1}, which is 47% of the theoretical capacity of BiF_3 (302 mA·h·g^{-1}), indicating partial conversion of BiF_3 to Bi. The first charge capacity was 80 mA·h·g^{-1}, which is 56% of initial discharge capacity. This indicates that only half of the initial capacity could be recovered during first cycle. In subsequent cycles, capacity faded quickly and decreased to 24 mA·h·g^{-1} after 10 cycles.

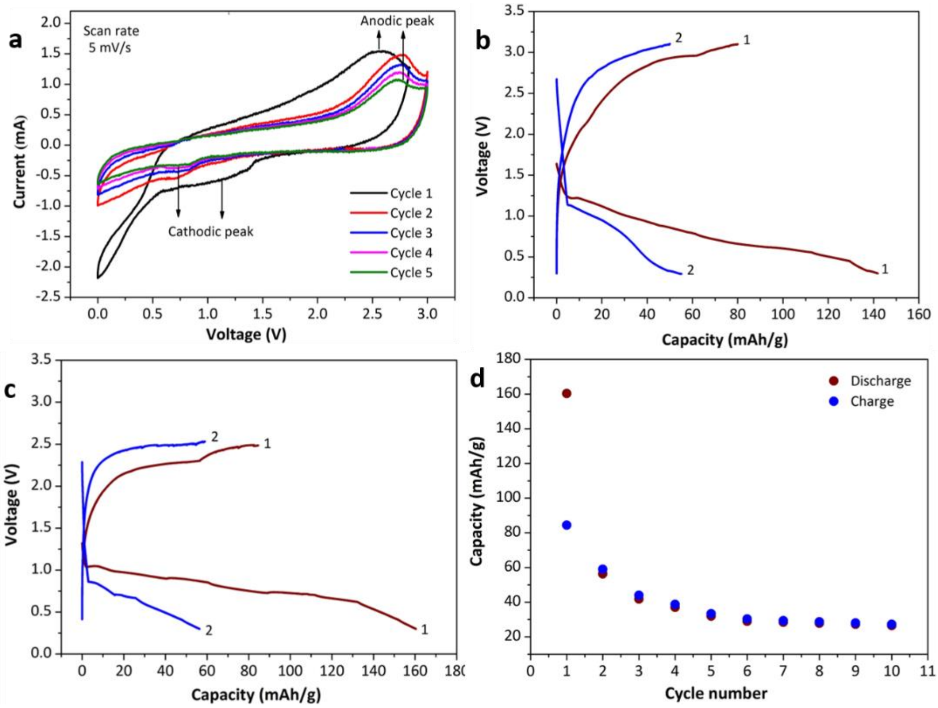

Figure 3.17. *(a) Cyclic voltammogram and (b) galvanostatic discharge-charge profiles of* $Mg+MgF_2/LiPF_6/BiF_3$ *cell. (c) galvanostatic discharge-charge profiles and (d) cyclic performance of* $Mg+MgF_2/LiPF_6/SnF_2$ *cell (A modified version of Figure 1 and 2 in paper [IV]).*

Electrochemical analysis and cyclic performance of $Mg+MgF_2/LiPF_6/SnF_2$ cell obtained at 25 °C with current density of 38 µA·cm^{-2} are given in Figure 3.17c, d. During first cycle, the cell delivered the discharge and charge capacity of 160 and 85 mA·h·g^{-1}, respectively (Figure 3.17c). The discharge capacity was 46% of the theoretical capacity (342 mA·h·g^{-1}), suggesting incomplete reaction occurred at cathode. The charge capacity was 53% of the first discharge capacity, indicating partial conversion of Sn to SnF_2. Further, both discharge and charge capacity gradually reduced as number of cycles were increased. After 10 cycles, discharge capacity reached to 27 mA·h·g^{-1} (Figure 3.17d). Both cells displayed similar capacity and cyclic performance. The exact reason of capacity fading is not known now, further studies are needed. The reversible volume changes at electrodes during the charge-discharge process might be a possible reason for capacity fading [108]. In addition, the oxidized product of Mg anode is very poor ionic conductor i. e. MgF_2, which would act as passivation layer for F^- diffusion. The passivation layer of MgF_2 at the anode might also contribute to the capacity fading [68]. Nevertheless, reversible fluorination/defluorination of magnesium anode against BiF_3 and SnF_2 cathodes was demonstrated using $LiPF_6$ as electrolyte.

3.4.2 XRD patterns of BiF_3 and SnF_2 cathodes before and after discharge

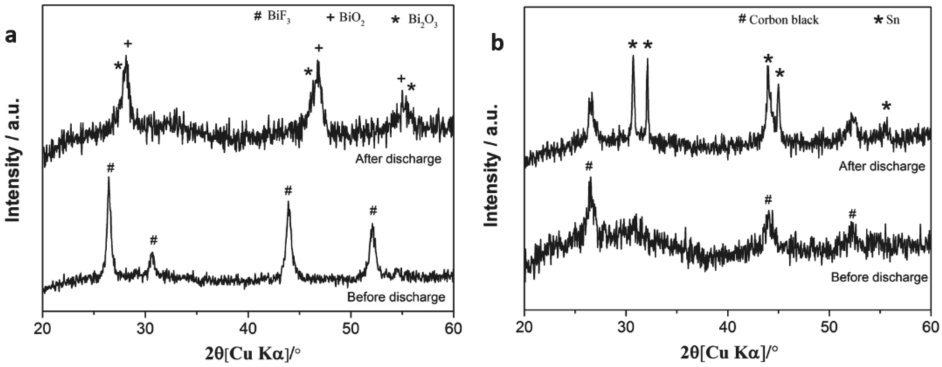

***Figure 3.18**. XRD patterns of (a) BiF_3 and (b) SnF_2 cathodes before and after discharge.*

To investigate the reaction mechanism for presented FIB systems, XRD measurements were carried out on the cathode pellets before and after discharge. Figure 3.18a shows XRD patterns of BiF_3 composite before and after discharge. Before discharge, peaks corresponding to nano crystalline phase of BiF_3 were observed. After full discharge, BiF_3 peaks vanished completely, demonstrating the complete reduction of BiF_3. In the pattern, reflections corresponding to Bi metal (reduced product of BiF_3) were not visible. This means metallic Bi might be available in the amorphous form. In addition, new diffraction peaks with less intensities were observed, which can be indexed to BiO_2 and Bi_2O_3 phases were observed (Figure 3.18). The formation of bismuth oxides might have resulted from chemical reaction of Bi metal and oxide impurities. The XRD patterns of SnF_2 cathode is displayed in the Figure 3.18b. Before discharge, carbon black phase and a broad peak (centered at a 2θ value of 30°) was observed. The broad signal was assigned to amorphous SnF_2, which was obtained after ball milling. After discharge, few new reflections were observed (marked with *), which were assigned to Sn metal, confirming the reduction of SnF_2 at cathode (Figure 3.18).

In summary, the reversible discharge and charge behavior of Mg as anode was demonstrated in FIBs employing $LiPF_6$ as electrolyte. In addition, relatively high potential rechargeable RT-FIBs was presented. The FIB cells were constructed using $Mg+MgF_2$ as anode, $LiPF_6$ as fluoride transporting electrolyte, and BiF_3 and SnF_2 as cathodes. Cyclic voltammogram profiles showed the reversible oxidation and reduction of BiF_3 in the $Mg+MgF_2/LiPF_6/BiF_3$ cell. Both types of FIB cells exhibited similar capacity and cyclic behavior. Reaction mechanism of electrochemical reaction was investigated by XRD measurements.

3.5 Other work towards the development of RT-FIBs

The topics, highlighted in the Theses are a selection from much more extensive work which did not produce impressive results, yet were unavoidable in scouting a huge landscape of FIB development. Here we briefly list other activities and analyze deviations from expected performance, giving valuable hindsight for subsequent focus:

1. Polycrystalline $La_{0.9}Ba_{0.1}F_{2.9}$ shows the high ionic conductivity mainly due to its tysonite type structure, whereas $BaSnF_4$ exhibits the high ionic conductivity due to the effect of the lone pair of electrons of Sn^{2+}. To introduce the benefit of both tysonite structure and lone pair of electrons in single compound, doping of tysonite type fluorides (LaF_3 and CeF_3) with SnF_2 or PbF_2 was attempted by mechanical milling. After trying several amounts of dopant such as x = 0.025, 0.095, and 0.075, not a single solid solution with tysonite structure was obtained. Also, various ball milling times and speeds were used, but all failed to dissolve even the smallest (x = 0.025) amount of SnF_2 or PbF_2 in the LaF_3 or CeF_3 compound. To further enhance the ionic conductivity of $BaSnF_4$, doping with KF and CaF_2 was tried by ball milling. In addition, SbF_3 doping with CaF_2 and SrF_2 was also attempted. In some cases, it was found that if ionic radii of dopant cation are equal or bigger than that of host cation, then solid state formation of was not possible. A detailed description of attempted synthesis of various compounds are given in below Table 3.4.

***Table 3.4**. A description of various compounds synthesized by ball milling method.*

Compound	**Ball milling speed (rpm)**	**Ball milling time (hours)**
$La_{1-x}Sn_xF_{3-x}$ ($0.025 \le x \le 0.075$)	300, 400, 500, 600	6, 12, 18, 24, 48
$La_{1-x}Pb_xF_{3-x}$ ($0.025 \le x \le 0.075$)	400, 600	12, 24, 48
$Ce_{1-x}Sn_xF_{3-x}$ ($0.025 \le x \le 0.075$)	500, 600	24, 36
$Ce_{1-x}Pb_xF_{3-x}$ ($0.025 \le x \le 0.075$)	600	12, 24
$Ba_{1-x}K_xSnF_{4-x}$ ($0.1 \le x \le 0.3$)	600	18
$CaSnF_4$	600	18
$Ba_{0.9}La_{0.1}SnF_{4.1}$	600	18
$Ca_{1-x}Sb_xF_{2+x}$ ($0.1 \le x \le 0.3$)	600	18
$Sr_{1-x}Sb_xF_{2+x}$ ($0.1 \le x \le 0.5$)	600	18

2. Up to date, only tin-based compounds like $BaSnF_4$ can be considered as suitable solid electrolyte for FIBs working as ambient temperature. The limited electrochemical stability of this electrolyte prohibits the use of high electropositive metal as an anode while fabrication for FIB. The usage of low electropositive metal anode against cathode like BiF_3 would result to low operating potential, which would lead to a low specific energy. To get high specific energy, cell voltage must be maximized, which can be achieved by the usage of high redox potential couples. In this thesis, other several redox couples were tested to build an efficient FIB using $BaSnF_4$ as electrolyte. However, none of them performed in FIB cell configuration according to their theoretical estimation. A detailed description of various redox couples tested during my thesis work period are given in Table 3.5.

Table 3.5. *A description of FIB cells employing $BaSnF_4$ constructed by usage of various redox couples.*

Cell No.	**Anode composite**	**Electrolyte**	**Cathode composite**	**OCV (V)**	**Emf (V)**
1	Zn	$BaSnF_4$	SbF_3	0.6	0.78
2	Sn	$BaSnF_4$	SbF_3	0.5	0.23
3	Zn	$BaSnF_4$	CuF_2	0.58	1.3
4	Sn	$BaSnF_4$	CuF_2	0.5	1.2
5	Zn	$BaSnF_4$	AgF	1	1.49
6	Sn	$BaSnF_4$	AgF	0.9	1.53
7	Mn	$BaSnF_4$	BiF_3	0.6	1.2
8	Fe	$BaSnF_4$	BiF_3	0.3	0.51

3. To build high potential RT-FIBs, high electropositive metal like Ce as anode was tested against BiF_3. Two types of FIB cells such as $Ce/BaSnF_4/BiF_3$ and Ce/ $La_{0.9}Ba_{0.1}F_{2.9}/BiF_3$ were constructed. The cell utilizing $BaSnF_4$ showed less OCV (1.2 V) and nearly zero capacity due to chemical reaction between Ce and $BaSnF_4$. The direct contact of Ce with $BaSnF_4$ would result to formation of CeF_3, BaF_2, and Sn metal at the interface. On other hand, cell utilizing $La_{0.9}Ba_{0.1}F_{2.9}$ showed an OCV of 2.5 V which is close to the theoretical emf of Ce/BiF_3 couple (2.83 V), but voltage immediately dropped to zero when applying any current between -1 to -4 µA. This immediate fading was due to poor ionic conductivity of $La_{0.9}Ba_{0.1}F_{2.9}$ at RT (4×10^{-7} $S{\cdot}cm^{-1}$). One way to enhance the electrochemical stability of $BaSnF_4$ layer may be by placing BaF_2-doped LaF_3 in contact with electrodes. Applying low ionic conductive $La_{0.9}Ba_{0.1}F_{2.9}$ layer on $BaSnF_4$ would increase the ionic conductivity of whole pellet as compared to pure $La_{0.9}Ba_{0.1}F_{2.9.}$ After optimizing the thickness of $La_{0.9}Ba_{0.1}F_{2.9}$ layer, $La_{0.9}Ba_{0.1}F_{2.9}$ (<45 µm)/$BaSnF_4$ (<700 µm) electrolyte exhibited an ionic conductivity of $0.89{\cdot}10^{-5}$ $S{\cdot}cm^{-1}$ at RT, which is sufficient to demonstrate the RT-FIB. To validate the interlayer electrolyte approach, a FIB cell was assembled using $La_{0.9}Ba_{0.1}F_{2.9}$ (< 45 µm)/$BaSnF_4$ (<700 µm) as electrolyte, Ce as anode, and BiF_3 as cathode. The cell showed an OCV of 1.5 V, which is around half of the theoretical emf of Ce/BiF_3 couple, and it dropped immediately to 0 V on cycling. This indicates that Ce particles might have penetrated the $La_{0.9}Ba_{0.1}F_{2.9}$ (<45 µm) layer during pressing the pellet and they have chemically reacted with less stable $BaSnF_4$. Another high electropositive metal like Mg was tested as anode against BiF_3 cathode using $La_{0.9}Ba_{0.1}F_{2.9}$ (90 µm)/$BaSnF_4$ (650 µm) as electrolye. The Mg based cell showed an OCV of 2.5 V which is close to the theoretical emf of Mg/BiF_3 couple. However, the cell delivered a very low discharge capacity (0.3 $mA{\cdot}h{\cdot}g^{-1}$), meaning that only a very thin layer of Mg might have reacted to form its discharge product: MgF_2. The formation of MgF_2 on the surface might block the further conversion of Mg to MgF_2 (at RT) as MgF_2 itself is a poor fluoride ion conductor. The FIB cells constructed by usage of high electropositive metals as anodes against BiF_3 are listed in Table 3.6.

Table 3.6. *A description of FIB cells utilizing high elecropositive metals anode anodes against BiF_3 cathode.*

Cell No.	**Anode**	**Electrolyte**	**Cathode**	**OCV (V)**	**Emf (V)**
1	Ce	$BaSnF_4$	BiF_3	1.2	2.83
	Ce	$La_{0.9}Ba_{0.1}F_{2.9}$	BiF_3	2.5	2.83
2	Ce	$La_{0.9}Ba_{0.1}F_{2.9}$ (45 µm)/$BaSnF_4$ (700 µm)	BiF_3	1.5	2.83
3	Mg	$La_{0.9}Ba_{0.1}F_{2.9}$ (90 µm)/$BaSnF_4$ (650 µm)	BiF_3	2.5	2.67
4	Ti	$La_{0.9}Ba_{0.1}F_{2.9}$ (90 µm)/$BaSnF_4$ (650 µm)	BiF_3	0.9	1.12
5	Ce-La	$La_{0.9}Ba_{0.1}F_{2.9}$ (90 µm)/$BaSnF_4$ (650 µm)	BiF_3	0.3	2.83
6	Ca	$La_{0.9}Ba_{0.1}F_{2.9}$ (90 µm)/$BaSnF_4$ (650 µm)	BiF_3	2.3	2.6
7	Y	$La_{0.9}Ba_{0.1}F_{2.9}$ (90 µm)/$BaSnF_4$ (650 µm)	BiF_3	1.3	2.79

4. Mg anode was also tested against CuF_2 and CoF_3 cathodes for RT-FIB using $LiPF_6$ as electrolyte. Both Mg/CuF_2 and Mg/CoF_3 couples showed similar OCV and discharge capacity of around 0.9 V and 50 $mA\cdot h\cdot g^{-1}$, respectively. However, the charge capacity was not observed in either case. In contrast to Mg/BiF_3 and Mg/SnF_2 systems, the electrochemical performance of Mg/CuF_2 and Mg/CoF_3 was very poor. The very low ionic conductivity of CuF_2 and CoF_3 cathodes might be responsible for their poor performance. A FIB cell in discharged state was also assembled using $LiPF_6$ as an electrolyte, Bi as a cathode and MgF_2 an anode. The OCV of the cell was 0.3 V, which increased to 1 V after charging several hours. This value is still less than the theoretical emf of MgF_2/Bi couple (2.67 V), indicating slow oxidation of Bi during the charge due to inactivity of Bi particles, which might be covered by oxide impurities. As a result, the cell failed to deliver any reasonable discharge capacity.

Conclusion

Results from this dissertation can be summarized as follow:

1. A new SbF_3-doped BaF_2 fluoride ion conductor was investigated. $Ba_{1-x}Sb_xF_{2+x}$ ($0 \leq x \leq 0.5$) compounds were synthesized by doping of BaF_2 with SbF_3 via ball milling process. All compounds were crystallized into single phase fluorite type crystal structure (except $x = 0.5$). The solubility limit of SbF_3 into BaF_2 crystal was found to be $x < 0.5$, beyond this concentration an impure phase was observed. All compositions (except $Ba_{0.9}Sb_{0.1}F_{2.1}$) exhibit similar ionic conductivity at higher temperatures. The conduction phenomena in polycrystalline $Ba_{1-x}Sb_xF_{2+x}$ was found to arise from migration of vacancies through grain boundaries. The highest ionic conductivity was obtained for sample $Ba_{0.7}Sb_{0.3}F_{2.3}$, which amounts to 4.4×10^{-4} $S\cdot cm^{-1}$ at 160 °C. Despite of similar crystal structures, the ionic conductivity of $Ba_{0.7}Sb_{0.3}F_{2.3}$ was higher than that of $Ba_{0.7}La_{0.3}F_{2.3}$. This enhancement in the conductivity of $Ba_{1-x}Sb_xF_{2+x}$ seems to be the effect of the lone pair of electrons of the Sb^{3+} ion. The $Ba_{0.7}Sb_{0.3}F_{2.3}$ composition was tested as cathode material for fluoride ion batteries using $La_{0.9}Ba_{0.1}F_{2.9}$ as electrolyte and Ce as anode. The FIB cell was able to deliver high capacity and voltage for several cycles at 150 °C. Future work will focus on determining the exact role of lone pair, which might be helpful for further ionic conductivity enhancement.

2. Highly conductive tetragonal structured $BaSnF_4$ enabled the demonstration of room temperature rechargeable FIBs. Two types of FIB cells were fabricated using $BaSnF_4$ as electrolyte, BiF_3 as cathode, and Sn and Zn as anodes. At 25 °C, the $Sn/BaSnF_4/BiF_3$ cell delivered a first discharge and charge capacity of 120 and 80 $mA\cdot h\cdot g^{-1}$, respectively. In the subsequent cycle's capacity faded and reduced to 30 $mA\cdot h\cdot g^{-1}$ after only four cycles. On the other hand, the Zn variety cell exhibited lower initial discharge and charge capacities of 56 and 43 $mA\cdot h\cdot g^{-1}$ at RT. In contrast to Sn based cell, capacity increased to 61 $mA\cdot h\cdot g^{-1}$ after 20 cycles. The rapid capacity fading of Sn anode cell upon cycling correlated with the increase of cell resistance during cycling. Also, SEM images of Sn anode before and after discharge show the presence of bigger Sn-particles, probably being another physical reason for the resistance increase. Rising the temperature, the performance of both systems improves. Although this thesis could demonstrate the feasibility of RT-FIB system, the cell delivered low energy density due to their low cell voltage. Future study will aim the devolopement of appropriate cathode and anode materials, which would provide high cell voltage and specific capacity.

3. The interlayer electrolytes concept was introduced and developed for high performance FIBs in order to overcome the chemical incompatibility of anode and electrolyte, in this case highly electropositive metal like Ce as an anode, and $BaSnF_4$ as a solid electrolyte. The “isolating” interlayer electrolyte is made of a thin layer of $La_{0.9}Ba_{0.1}F_{2.9}$, about 3 order of magnitude less conductive that $BaSnF_4$. $La_{0.9}Ba_{0.1}F_{2.9}$ (<45 µm)/$BaSnF_4$ (<700 µm) electrolyte exhibited an ionic conductivity of 0.89×10^{-5} $S\cdot cm^{-1}$ at RT, which is approximately 22 times higher than pure $La_{0.9}Ba_{0.1}F_{2.9}$ (4×10^{-7} $S\cdot cm^{-1}$) but about 39 times smaller compared to pure

$BaSnF_4$ (3.5×10^{-4} S·cm^{-1}). This interlayer electrolyte concept enabled the demonstration of relatively high potential FIBs at RT, not possible either with $La_{0.9}Ba_{0.1}F_{2.9}$ or $BaSnF_4$ electrolyte alone. The actual FIB cell was constructed using $La_{0.9}Ba_{0.1}F_{2.9}$ (90 µm)/$BaSnF_4$ (650 µm). During the first cycle, the discharge and charge profile displayed the high average voltage of 1.4 and 3.2 V, respectively. Despite obtaining discharge and capacity of 27 and 24 mA·h·g^{-1} during first cycle, respectively, capacity faded to 3 mA·h·g^{-1} after only five cycles, do not render this implementation a practical battery, an important proof of interlayer principle was demonstrated paving many routes to high performance FIB. In Future study, much thinner $La_{0.9}Ba_{0.1}F_{2.9}$ layer (≈100 nm or less) will be applied on $BaSnF_4$ by improved coating methods to achieve high ionic conductivities similar to that of pure $BaSnF_4$.

4. The electrochemical performance of Mg as anode against BiF_3 and SnF_2 cathodes was investigated using a principally different electrolyte class-$LiPF_6$. In addition, RT-FIBs with relatively high voltage of around 1 V was demonstrated. CV analysis showed the reversible oxidation and reduction behavior of BiF_3 cathode in $LiPF_6$ electrolyte. The Mg+MgF_2/$LiPF_6$/BiF_3 cell delivered a first discharge capacity of 142 mA·h·g^{-1}, whereas the Mg+MgF_2/$LiPF_6$/SnF_2 exhibited even higher first discharge capacity of 160 mA·h·g^{-1} and relatively high current density of 38 µA·cm^{-2}. Both cells showed rapid cyclic fading, resulting the discharge capacities of BiF_3 and SnF_2 based cell reduced to 25 and 26 mA·h·g^{-1} after 10 cycles. Nevertheless, this thesis study demonstrated a feasibility of reducing need for rare earth elements in FIBs and deployment of PF_6^- electrolyte systems with a further perspective of double carrier (Li and F) cells. Future work will center on testing high electropositive anodes like Ca for FIBs using PF_6^- systems as electrolytes.

5. An unpublished work of my thesis has provided a better insight to understanding the main problem regarding development of FIBs. After trying several types of doping experiments, it was found that homo or hetrovalent doping was possible only if ionic radii of dopant cation was much smaller that of the host cation. This finding led to the discovery of a good fluoride ion conductive fluorite type $Ba_{1-x}Sb_xF_{2+x}$ compound, where ionic radii of Sb^{3+} (0.76 Å) is much smaller than Ba^{2+} (1.42 Å). It was concluded that the feasibility of RT solid-state FIB lies in the development of electrolyte with a sufficient ionic conductivity (RT) and high electrochemical stability. Also, cathode and anode (discharge product) materials should possess significant ion conductivity at RT, which helped to demonstrate the rechargeable room temperature solid-state FIB for the first time. High ion conductive $BaSnF_4$ as an electrolyte was not compatible with high electropositive metals like Ce as anode due to its limited electrochemical stability. Despite the compatibility of $La_{0.9}Ba_{0.1}F_{2.9}$ electrolyte with Ce anode, demonstration of high voltage RT-FIB was not feasible due to its low ion conductivity. These results guided to the development of novel interlayer electrolyte concept for FIBs.

References

[1] M. Anji Reddy and M. Fichtner, "Batteries based on fluoride shuttle," *Journal of Materials Chemistry,* vol. 21, pp. 17059-17062, 2011.

[2] D. T. Thieu, M. H. Fawey, H. Bhatia, T. Diemant, V. S. K. Chakravadhanula, R. J. Behm, C. Kübel, and M. Fichtner, "CuF_2 as Reversible Cathode for Fluoride Ion Batteries," *Advanced Functional Materials,* vol. 27, p. 1701051, 2017.

[3] K.-i. Okazaki, Y. Uchimoto, T. Abe, and Z. Ogumi, "Charge–Discharge Behavior of Bismuth in a Liquid Electrolyte for Rechargeable Batteries Based on a Fluoride Shuttle," *ACS Energy Letters,* vol. 2, pp. 1460-1464, 2017.

[4] M. Winter and R. J. Brodd, "What Are Batteries, Fuel Cells, and Supercapacitors?," *Chemical Reviews,* vol. 104, pp. 4245-4270, 2004.

[5] D. Linden and T. B. Reddy, *Handbook of batteries*. New York, N.Y.: McGraw-Hill, 2002.

[6] M. S. Whittingham, R. F. Savinell, and T. Zawodzinski, "Introduction: Batteries and Fuel Cells," *Chemical Reviews,* vol. 104, pp. 4243-4244, 2004.

[7] O. Haas and E. J. Cairns, "Chapter 6. Electrochemical energy storage," *Annual Reports Section "C" (Physical Chemistry),* vol. 95, pp. 163-198, 1999.

[8] K. R. Bullock, "Lead/acid batteries," *Journal of Power Sources,* vol. 51, pp. 1-17, 1994.

[9] B. Scrosati, "The present status of battery technology," *Renewable Energy,* vol. 5, pp. 285-294, 1994.

[10] M. A. Fetcenko, S. R. Ovshinsky, B. Reichman, K. Young, C. Fierro, J. Koch, A. Zallen, W. Mays, and T. Ouchi, "Recent advances in NiMH battery technology," *Journal of Power Sources,* vol. 165, pp. 544-551, 2007.

[11] V. Etacheri, R. Marom, R. Elazari, G. Salitra, and D. Aurbach, "Challenges in the development of advanced Li-ion batteries: a review," *Energy & Environmental Science,* vol. 4, pp. 3243-3262, 2011.

[12] J. B. Goodenough and K.-S. Park, "The Li-Ion Rechargeable Battery: A Perspective," *Journal of the American Chemical Society,* vol. 135, pp. 1167-1176, 2013.

[13] J. M. Tarascon and M. Armand, "Issues and challenges facing rechargeable lithium batteries," *Nature,* vol. 414, p. 359, 2001.

[14] I. Hasa, D. Buchholz, S. Passerini, B. Scrosati, and J. Hassoun, "High Performance $Na_{0.5}[Ni_{0.23}Fe_{0.13}Mn_{0.63}]O_2$ Cathode for Sodium-Ion Batteries," *Advanced Energy Materials,* vol. 4, p. 1400083, 2014.

[15] A. Ponrouch, C. Frontera, F. Bardé, and M. R. Palacín, "Towards a calcium-based rechargeable battery," *Nature Materials,* vol. 15, p. 169, 2015.

[16] Z. Zhao-Karger, X. Zhao, D. Wang, T. Diemant, R. J. Behm, and M. Fichtner, "Performance Improvement of Magnesium Sulfur Batteries with Modified Non-Nucleophilic Electrolytes," *Advanced Energy Materials,* vol. 5, p. 1401155, 2015.

[17] M. Armand and J. M. Tarascon, "Building better batteries," *Nature,* vol. 451, p. 652, 2008.

[18] P. G. Bruce, B. Scrosati, and J.-M. Tarascon, "Nanomaterials for Rechargeable Lithium Batteries," *Angewandte Chemie International Edition,* vol. 47, pp. 2930-2946, 2008.

[19] G. E. Blomgren, "The Development and Future of Lithium Ion Batteries," *Journal of The Electrochemical Society,* vol. 164, pp. A5019-A5025, 2017.

[20] J. Wang, Y. Li, and X. Sun, "Challenges and opportunities of nanostructured materials for aprotic rechargeable lithium–air batteries," *Nano Energy,* vol. 2, pp. 443-467, 2013.

[21] J. B. Goodenough and Y. Kim, "Challenges for Rechargeable Li Batteries," *Chemistry of Materials,* vol. 22, pp. 587-603, 2010.

[22] J. Broadhead, D. W. Murphy, and B. C. H. Steele, *Materials for advanced batteries*: Plenum Press, 1980.

[23] S. Yuvaraj, R. K. Selvan, and Y. S. Lee, "An overview of $AB_2O_4^-$ and $A_2BO_4^-$ structured negative electrodes for advanced Li-ion batteries," *RSC Advances,* vol. 6, pp. 21448-21474, 2016.

[24] M. S. Whittingham, "Electrical Energy Storage and Intercalation Chemistry," *Science,* vol. 192, p. 1126, 1976.

[25] D. Fauteux and R. Koksbang, "Rechargeable lithium battery anodes: alternatives to metallic lithium," *Journal of Applied Electrochemistry,* vol. 23, pp. 1-10, 1993.

[26] J. O. Besenhard, P. Komenda, A. Paxinos, E. Wudy, and M. Josowicz, "Binary and ternary Li-alloys as anode materials in rechargeable organic electrolyte Li-batteries," *Solid State Ionics,* vol. 18-19, pp. 823-827, 1986.

[27] J. Yang, M. Winter, and J. O. Besenhard, "Small particle size multiphase Li-alloy anodes for lithium-ionbatteries," *Solid State Ionics,* vol. 90, pp. 281-287, 1996.

[28] K. Sawai, Y. Iwakoshi, and T. Ohzuku, "Carbon materials for lithium-ion (shuttlecock) cells," *Solid State Ionics,* vol. 69, pp. 273-283, 1994.

[29] S. Megahed and B. Scrosati, "Lithium-ion rechargeable batteries," *Journal of Power Sources,* vol. 51, pp. 79-104, 1994.

[30] S. Ma, J. Li, X. Jing, and F. Wang, "A study of cokes used as anodic materials in lithium ion rechargeable batteries," *Solid State Ionics,* vol. 86-88, pp. 911-917, 1996.

[31] R. Yazami and P. Touzain, "A reversible graphite-lithium negative electrode for electrochemical generators," *Journal of Power Sources,* vol. 9, pp. 365-371, 1983.

[32] E. Ferg, R. J. Gummow, A. de Kock, and M. M. Thackeray, "Spinel Anodes for Lithium-Ion Batteries," *Journal of The Electrochemical Society,* vol. 141, pp. L147-L150, 1994.

[33] T. Ohzuku, A. Ueda, and N. Yamamoto, "Zero-Strain Insertion Material of $Li[Li_{1/3}Ti_{5/3}]O_4$ for Rechargeable Lithium Cells," *Journal of The Electrochemical Society,* vol. 142, pp. 1431-1435, 1995.

[34] J. Christensen, V. Srinivasan, and J. Newman, "Optimization of Lithium Titanate Electrodes for High-Power Cells," *Journal of The Electrochemical Society,* vol. 153, pp. A560-A565, 2006.

[35] A. K. Padhi, K. S. Nanjundaswamy, and J. B. Goodenough, "Phospho-olivines as Positive-Electrode Materials for Rechargeable Lithium Batteries," *Journal of The Electrochemical Society,* vol. 144, pp. 1188-1194, 1997.

[36] M. S. Whittingham, "Lithium Batteries and Cathode Materials," *Chemical Reviews,* vol. 104, pp. 4271-4302, 2004.

[37] R. Alcantara, P. Lavela, J. L. Tirado, E. Zhecheva, and R. Stoyanova, "Recent advances in the study of layered lithium transition metal oxides and their application as intercalation electrodes," *Journal of Solid State Electrochemistry,* vol. 3, pp. 121-134, 1999.

[38] J. Molenda, P. Wilk, and J. Marzec, "Structural, electrical and electrochemical properties of $LiNiO_2$," *Solid State Ionics,* vol. 146, pp. 73-79, 2002.

[39] M. Mohan Rao, M. Jayalakshmi, O. Schäf, U. Guth, H. Wulff, and F. Scholz, "Electrochemical behaviour of solid lithium nickelate ($LiNiO_2$) in an aqueous electrolyte system," *Journal of Solid State Electrochemistry,* vol. 4, pp. 17-23, 1999.

[40] Y. S. Lee, Y. K. Sun, and K. S. Nahm, "Synthesis and characterization of $LiNiO_2$ cathode material prepared by an adiphic acid-assisted sol–gel method for lithium secondary batteries," *Solid State Ionics,* vol. 118, pp. 159-168, 1999.

[41] D. K. Kim, P. Muralidharan, H.-W. Lee, R. Ruffo, Y. Yang, C. K. Chan*,* H. Peng, R. A. Huggins, and Y. Cu*i*, "Spinel $LiMn_2O_4$ Nanorods as Lithium Ion Battery Cathodes," *Nano Letters,* vol. 8, pp. 3948-3952, 2008.

[42] Y. Zhang, Y. Li, X. Xia, X. Wang, C. Gu, and J. Tu, "High-energy cathode materials for Li-ion batteries: A review of recent developments," *Science China Technological Sciences,* vol. 58, pp. 1809-1828, 2015.

[43] M. Gu, I. Belharouak, J. Zheng, H. Wu, J. Xiao, A. Genc*, et al.*, "Formation of the Spinel Phase in the Layered Composite Cathode Used in Li-Ion Batteries," *ACS Nano,* vol. 7, pp. 760-767, 2013.

[44] K. M. Shaju and P. G. Bruce, "Macroporous $Li(Ni_{1/3}Co_{1/3}Mn_{1/3})O_2$: A High-Power and High-Energy Cathode for Rechargeable Lithium Batteries," *Advanced Materials,* vol. 18, pp. 2330-2334, 2006.

[45] H. Zheng, Q. Sun, G. Liu, X. Song, and V. S. Battaglia, "Correlation between dissolution behavior and electrochemical cycling performance for $LiNi_{1/3}Co_{1/3}Mn_{1/3}O_2$-based cells," *Journal of Power Sources,* vol. 207, pp. 134-140, 2012.

[46] M. C. Julien, A. Mauger, K. Zaghib, and H. Groult, "Comparative Issues of Cathode Materials for Li-Ion Batteries," *Inorganics,* vol. 2, 2014.

[47] X. Zhao, S. Ren, M. Bruns, and M. Fichtner, "Chloride ion battery: A new member in the rechargeable battery family," *Journal of Power Sources,* vol. 245, pp. 706-711, 2014.

[48] X. Zhao, Z. Zhao-Karger, D. Wang, and M. Fichtner, "Metal Oxychlorides as Cathode Materials for Chloride Ion Batteries," *Angewandte Chemie International Edition,* vol. 52, pp. 13621-13624, 2013.

[49] X. Zhao, Q. Li, Z. Zhao-Karger, P. Gao, K. Fink, X. Shen*, et al.*, "Magnesium Anode for Chloride Ion Batteries," *ACS Applied Materials & Interfaces,* vol. 6, pp. 10997-11000, 2014.

[50] P. Gao, X. Zhao, Z. Zhao-Karger, T. Diemant, R. J. Behm, and M. Fichtner, "Vanadium Oxychloride/Magnesium Electrode Systems for Chloride Ion Batteries," *ACS Applied Materials & Interfaces,* vol. 6, pp. 22430-22435, 2014.

[51] P. Gao, M. A. Reddy, X. Mu, T. Diemant, L. Zhang, Z. Zhao-Karger*, et al.*, "VOCl as a Cathode for Rechargeable Chloride Ion Batteries," *Angewandte Chemie International Edition,* vol. 55, pp. 4285-4290, 2016.

[52] X. Zhao, Q. Li, T. Yu, M. Yang, K. Fink, and X. Shen, "Carbon incorporation effects and reaction mechanism of FeOCl cathode materials for chloride ion batteries," *Scientific Reports,* vol. 6, p. 19448, 2016.

[53] F. Chen, Z. Y. Leong, and H. Y. Yang, "An aqueous rechargeable chloride ion battery," *Energy Storage Materials,* vol. 7, pp. 189-194, 2017.

[54] F. Gschwind, D. Steinle, D. Sandbeck, C. Schmidt, and E. von Hauff, "Facile Preparation of Chloride-Conducting Membranes: First Step towards a Room-Temperature Solid-State Chloride-Ion Battery," *ChemistryOpen,* vol. 5, pp. 525-530, 2016.

[55] W. Baukal, "Solid-electrolyte cell," DE2017128A, 1971.

[56] W. Baukal, R. Knodler, and W. Kuhn, "Overview of the Applications of Solid Electrolytes," *Chem. Ing. Tech,* vol. 50, pp. 245-249, 1978.

[57] J. H. Kennedy and J. C. Hunter, "Thin-Film Galvanic Cell Pb/PbF_2/PbF_2, CuF_2/Cu," *Journal of The Electrochemical Society,* vol. 123, pp. 10-14, 1976.

[58] P. Hagenmuller, J.-M. Réau, C. Lucat, S. Matar, and G. Villeneuve, "Ionic conductivity of fluorite-type fluorides," *Solid State Ionics,* vol. 3-4, pp. 341-345, 1981.

[59] J. Schoonman, "A Solid-State Galvanic Cell with Fluoride-Conducting Electrolytes," *Journal of The Electrochemical Society,* vol. 123, pp. 1772-1775, 1976.

[60] A. A. Potanin, "Solid State Chemical Current Source Based on Ionic Conductor of the Lanthanum Trifluoride Type," *Ross. Khim. Zh,* vol. 45, pp. 58-63, 2001.

[61] A. A. Potanin, "Solid-state secondary power supply," WO2006112756A1, 2006.

[62] C. Rongeat, M. Anji Reddy, T. Diemant, R. J. Behm, and M. Fichtner, "Development of new anode composite materials for fluoride ion batteries," *Journal of Materials Chemistry A,* vol. 2, pp. 20861-20872, 2014.

[63] L. Zhang, M. Anji Reddy, P. Gao, and M. Fichtner, "Development of dense solid state thin-film electrolyte for fluoride ion batteries," *Journal of Alloys and Compounds,* vol. 684, pp. 733-738, 2016.

[64] M. A. Nowroozi, K. Wissel, J. Rohrer, A. R. Munnangi, and O. Clemens, "$LaSrMnO_4$: Reversible Electrochemical Intercalation of Fluoride Ions in the Context of Fluoride Ion Batteries," *Chemistry of Materials,* vol. 29, pp. 3441-3453, 2017.

[65] M. A. Nowroozi, S. Ivlev, J. Rohrer, and O. Clemens, "La_2CoO_4: a new intercalation based cathode material for fluoride ion batteries with improved cycling stability," *Journal of Materials Chemistry A,* vol. 6, pp. 4658-4669, 2018.

[66] O. Clemens, C. Rongeat, M. A. Reddy, A. Giehr, M. Fichtner, and H. Hahn, "Electrochemical fluorination of perovskite type $BaFeO_{2.5}$," *Dalton Transactions,* vol. 43, pp. 15771-15778, 2014.

[67] F. Gschwind, Z. Zao-Karger, and M. Fichtner, "A fluoride-doped PEG matrix as an electrolyte for anion transportation in a room-temperature fluoride ion battery," *Journal of Materials Chemistry A,* vol. 2, pp. 1214-1218, 2014.

[68] F. Gschwind and J. Bastien, "Parametric investigation of room-temperature fluoride-ion batteries: assessment of electrolytes, Mg-based anodes, and BiF_3-cathodes," *Journal of Materials Chemistry A,* vol. 3, pp. 5628-5634, 2015.

[69] Z. Zhang, X. Hu, Y. Zhou, S. Wang, L. Yao, H. Pan*, et al.*, "Aqueous rechargeable dual-ion battery based on fluoride ion and sodium ion electrochemistry," *Journal of Materials Chemistry A,* vol. 6, pp. 8244-8250, 2018.

[70] A. K. Ivanov-Shits and N. I. Sorokin, "Parameters of bulk and electrode impedance of single crystal superionic conductors $Ca_{1-x}R_xF_{2+x}$ ($0.2 \leqslant x < 0.4$, R=Rare earths)," *Solid State Ionics,* vol. 36, pp. 7-13, 1989.

[71] N. I. Sorokin and M. W. Breiter, "Anionic conductivity and thermal stability of single crystals of solid solutions based on strontium fluoride," *Solid State Ionics,* vol. 104, pp. 325-333, 1997.

[72] N. I. Sorokin and M. W. Breiter, "Anionic conductivity and thermal stability of single crystals of solid solutions based on calcium fluoride," *Solid State Ionics,* vol. 116, pp. 157-165, 11999.

[73] N. I. Sorokin and M. W. Breiter, "Anionic conductivity and thermal stability of single crystals of solid solutions based on barium fluoride," *Solid State Ionics,* vol. 99, pp. 241-250, 1997.

[74] Y. Saito and J. Maier, "Ionic Conductivity Enhancement of the Fluoride Conductor CaF_2 by Grain Boundary Activation Using Lewis Acids," *Journal of The Electrochemical Society,* vol. 142, pp. 3078-3083, 1995.

[75] W. Puin, S. Rodewald, R. Ramlau, P. Heitjans, and J. Maier, "Local and overall ionic conductivity in nanocrystalline CaF_2," *Solid State Ionics,* vol. 131, pp. 159-164, 2000.

[76] A. Düvel, B. Ruprecht, P. Heitjans, and M. Wilkening, "Mixed Alkaline-Earth Effect in the Metastable Anion Conductor $Ba_{1-x}Ca_xF_2$ ($0 \leq x \leq 1$): Correlating Long-Range Ion Transport with Local Structures Revealed by Ultrafast ^{19}F MAS NMR," *The Journal of Physical Chemistry C,* vol. 115, pp. 23784-23789, 2011.

[77] M. V. Subrahmanya Sarma and S. V. Suryanarayana, "Ionic conductivity of CaF_2-SrF_2 mixed crystals," *Solid State Ionics,* vol. 42, pp. 227-232, 1990.

[78] T. Takahashi, H. Iwahara, and T. Ishikawa, "Ionic Conductivity of Doped Cerium Trifluoride," *Journal of The Electrochemical Society,* vol. 124, pp. 280-284, 1977.

[79] N. I. Sorokin, E. A. Krivandina, Z. I. Zhmurova, B. P. Sobolev, M. V. Fominykh, and V. V. Fistul', "Superionic conductivity of the heterovalent solid solutions $R_{1-x}M_xF_{3-x}$(R=REE, M=Ca, Ba) with tysonite-type structure," *Physics of the Solid State,* vol. 41, pp. 573-575, 1999.

[80] B. P. Sobolev, "Nonstoichiometry in inorganic fluorides: I. Nonstoichiometry in MF_m-RF_n ($m<n\leq4$) systems," *Crystallography Reports,* vol. 57, pp. 434-454, 2012.

[81] N. I. Sorokin, N. A. Ivanovskaya, and B. P. Sobolev, "Ionic conductivity of cold-pressed ceramics from grinding of $R_{0.95}M_{0.05}F_{2.95}$ solid electrolytes (R = La, Nd; M = Ca, Sr, Ba) synthesized by reaction in melt," *Crystallography Reports,* vol. 59, pp. 248-251, 2014.

[82] C. Rongeat, M. A. Reddy, R. Witter, and M. Fichtner, "Nanostructured Fluorite-Type Fluorides As Electrolytes for Fluoride Ion Batteries," *The Journal of Physical Chemistry C,* vol. 117, pp. 4943-4950, 2013.

[83] F. Wang and C. P. Grey, "Probing the Defect Structure of Anion-Excess $Ca_{1-x}Y_xF_{2+x}$ (x = 0.03−0.32) with High-Resolution ^{19}F Magic-Angle Spinning Nuclear Magnetic Resonance Spectroscopy," *Chemistry of Materials,* vol. 10, pp. 3081-3091, 1998.

[84] C. Rongeat, M. Anji Reddy, R. Witter, and M. Fichtner, "Solid Electrolytes for Fluoride Ion Batteries: Ionic Conductivity in Polycrystalline Tysonite-Type Fluorides," *ACS Applied Materials & Interfaces,* vol. 6, pp. 2103-2110, 2014.

[85] A. K. Ivanov-Shits, N. I. Sorokin, P. P. Fedorov, and B. P. Sobolev, "Specific features of ion transport in nonstoichiometric fluorite-type $Ba_{1-x}R_xF_{2+x}$ (R=La−Lu phases," *Solid State Ionics,* vol. 31, pp. 269-280, 1989.

[86] N. I. Sorokin, E. A. Krivandina, Z. I. Zhmurova, B. P. Sobolev, and M. V. Fominykh, "Superionic conductivity of the heterovalent solid solutions R1−x MxF3−x (R= REE, M= Ca, Ba) with tysonite-type structure," *Physics of the Solid State,* vol. 41, pp. 573-575, 1999.

[87] J. Schoonman, G. Oversluizen, and K. E. D. Wapenaar, "Solid electrolyte properties of LaF3," *Solid State Ionics,* vol. 1, pp. 211-221, 1980.

[88] B. Dieudonné, J. Chable, F. Mauvy, S. Fourcade, E. Durand, E. Lebraud*, et al., Exploring the* $Sm_{1-x}Ca_xF_{3-x}$ *Tysonite Solid Solution as Solid State Electrolyte: Relationships Between Structural Features and F- Ionic Conductivity* vol. 119, 2015.

[89] A. Düvel, J. Bednarcik, V. Šepelák, and P. Heitjans, "Mechanosynthesis of the Fast Fluoride Ion Conductor $Ba_{1-x}La_xF_{2+x}$: From the Fluorite to the Tysonite Structure," *The Journal of Physical Chemistry C,* vol. 118, pp. 7117-7129, 2014.

[90] S. Chaudhuri, F. Wang, and C. P. Grey, "Resolving the Different Dynamics of the Fluorine Sublattices in the Anionic Conductor $BaSnF_4$ by Using High-Resolution MAS NMR Techniques," *Journal of the American Chemical Society,* vol. 124, pp. 11746-11757, 2002.

[91] R. Kanno, K. Ohno, H. Izumi, Y. Kawamoto, T. Kamiyama, H. Asano*, et al.,* "Neutron diffraction stufy of the high-fluoride-ion conductor, $PbSnF_4$, prepared under an HF atmosphere," *Solid State Ionics,* vol. 70-71, pp. 253-258, 1994.

[92] F. Preishuber-Pflügl, V. Epp, S. Nakhal, M. Lerch, and M. Wilkening, "Defect-enhanced F– ion conductivity in layer-structured nanocrystalline $BaSnF_4$ prepared by high-energy ball milling combined with soft annealing," *physica status solidi c,* vol. 12, pp. 10-14, 2015.

[93] N. I. Sorokin, "SnF_2-Based Solid Electrolytes," *Inorganic Materials,* vol. 40, pp. 989-997, 2004.

[94] A. V. Chadwick, E. S. Hammam, D. Vanderputten, and J. H. Strange, "Studies of ionic transport in MF_2-SnF_2 systems," *CRYSTAL LATTICE DEFECTS AND AMORPHOUS MATERIALS,* vol. 15, pp. 303-308, 1987.

[95] M. M. Ahmad, Y. Yamane, and K. Yamada, "Structure, ionic conduction, and giant dielectric properties of mechanochemically synthesized $BaSnF_4$," *Journal of Applied Physics,* vol. 106, p. 074106, 2009.

[96] A. Le Bail, "Whole powder pattern decomposition methods and applications: A retrospection," *Powder Diffraction,* vol. 20, pp. 316-326, 2005.

[97] P. Thompson, D. E. Cox, and J. B. Hastings, "Rietveld refinement of Debye–Scherrer synchrotron X-ray data from Al_2O_3," *Journal of Applied Crystallography,* vol. 20, pp. 79-83, 1987.

[98] J. I. Langford, "A rapid method for analysing the breadths of diffraction and spectral lines using the Voigt function," *Journal of Applied Crystallography,* vol. 11, pp. 10-14, 1978.

[99] R. D. Shannon, "Revised effective ionic radii and systematic studies of interatomic distances in halides and chalcogenides," *Acta crystallographica section A: crystal physics, diffraction, theoretical and general crystallography,* vol. 32, pp. 751-767, 1976.

[100] W. Meier, C. Apblett, D. Ingersoll, A. McDaniel, and J. F. Ihlefeld, "Preparation and Processing Temperature Effects on Ion Conductivity in Solution Derived Sodium Zirconium Phosphate ($NaZr_2P_3O_{12}$) Thin Films," *Journal of The Electrochemical Society,* vol. 161, pp. A364-A367, 2014.

[101] T. J. Udovic, M. Matsuo, A. Unemoto, N. Verdal, V. Stavila, A. V. Skripov*, et al.*, "Sodium superionic conduction in $Na_2B_{12}H_{12}$," *Chemical Communications,* vol. 50, pp. 3750-3752, 2014.

[102] J. P. Laval, A. Mikou, B. Frit, and G. Roult, "Short-range order in heavily doped CaF2:Ln3+ fluorites: A powder neutron diffraction study," *Solid State Ionics,* vol. 28-30, pp. 1300-1304, 1988.

[103] A. K. Ivanov-Shits and I. V. Murin, "Ionika tverdogo tela," *Solid-State Ionics), St. Petersburg: S.-Peterburg. Univ,* vol. 1, 2000.

[104] J. T. S. Irvine, D. C. Sinclair, and A. R. West, "Electroceramics: Characterization by Impedance Spectroscopy," *Advanced Materials,* vol. 2, pp. 132-138, 1990.

[105] M. A. Nowroozi and O. Clemens, *Insights on the Behavior of Conversion Based Anode Materials for Fluoride Ion Batteries by Testing Against an Intercalation-Based Reference Cathode* vol. 1, 2018.

[106] A. Grenier, A. G. Porras Gutierrez, H. Groult, and D. Dambournet, "Modified coin cells to evaluate the electrochemical properties of solid-state fluoride-ion batteries at 150 °C," *Journal of Fluorine Chemistry,* vol. 191, pp. 23-28, 2016.

[107] H. Bhatia, D. T. Thieu, A. H. Pohl, V. S. K. Chakravadhanula, M. H. Fawey, C. Kübel*, et al.*, "Conductivity Optimization of Tysonite-type $La_{1-x}Ba_xF_{3-x}$ Solid Electrolytes for Advanced Fluoride Ion Battery," *ACS Applied Materials & Interfaces,* vol. 9, pp. 23707-23715, 2017.

[108] L. Li, F. Meng, and S. Jin, "High-Capacity Lithium-Ion Battery Conversion Cathodes Based on Iron Fluoride Nanowires and Insights into the Conversion Mechanism," *Nano Letters,* vol. 12, pp. 6030-6037, 2012.

[109] J. Cabana, L. Monconduit, D. Larcher, and M. R. Palacín, "Beyond Intercalation-Based Li-Ion Batteries: The State of the Art and Challenges of Electrode Materials Reacting Through Conversion Reactions," *Advanced Materials,* vol. 22, pp. E170-E192, 2010.

[110] M. Hammad Fawey, V. S. K. Chakravadhanula, M. A. Reddy, C. Rongeat, T. Scherer, H. Hahn*, et al.*, "In situ TEM studies of micron-sized all-solid-state fluoride ion batteries: Preparation, prospects, and challenges," *Microscopy Research and Technique,* vol. 79, pp. 615-624, 2016.

Acknowledgements

This thesis is based on the experimental work carried out at NMR Institute MTÜ, School of Information Technology, Tallinn University of Technology and Helmholtz Institute Ulm (HIU), Germany. I would like to express my sincere gratitude to my supervisor Associate Professor Raiker Witter for his guidance, support, and motivation during my whole doctoral study.

I want to thank to my co-supervisor Dr. Ago Samoson, Lead Scientist, School of Information Technologies, for allowing me to accomplish my doctoral thesis under support of the NMR Institute MTÜ.

I want to thank Professor Kalju Meigas, Director of the School of Information Technologies: Department of Health Technologies, for giving me possibility to carry out this doctoral thesis.

I want to thank Professor Tonis Kanger, Dean of the School of Science: Department of Chemistry and Biotechnology: Division of Chemistry, for enrolling me as PhD student in the study program of Chemistry and Biotechnology.

I am very thankful to the co-authors and colleagues at the Helmholtz Institute Ulm. I want to sincerely thank Professor Maximillian Fitchtner, Deputy Director of Helmholtz Institute Ulm for giving me opportunity to carry out my research at Solid State Chemistry group of HIU for 10 months.

I want to thank Dr. Anji Reddy Munnangi for his supervision of my work during my visit at HIU. I want to thank Dr. Johann Chable for his help in X-ray diffraction, Impedance spectroscopy and XRD refinement.

I am grateful and thankful to all colleagues at NMR Institute MTÜ. I want to thank Mr. Palanivel Molaiyan, Mr. Meelis Rohtmäe, Mr. Andres Oss, Dr. Kalju Vanatalu, and Ms. Steffi Witter for their assistance during my doctoral study.

My warmest thanks I would like to express to my family and friends for their encouragement and steady support.

I would like to acknowledge Estonian Ministry of Education through PUT126 (Smart spinning) and PUT 1534 (Structural Biology of Viscous Systems), The European Union through the European Regional Development Fund (Dora Plus Action 1), European Social Fund for project MTT68 (Microwave and Scale enhanced NMR of Micro-Drops, -Leaflets, Cells and Nanoparticles), and TUT state stipend.

Abstract

Development of Room Temperature Rechargeable Solid-State Fluoride Ion Batteries

Rechargeable solid-state fluoride ion batteries emerged as suitable candidates of post-lithium technologies for electrochemical energy storage devices. Fluoride ion batteries (FIBs) offer high specific energy, thermal stability, and safety at possibly low price. Current, research on FIBs is in early stage of growth and a number of issues still need to be resolved regarding improvement the performance of electrodes and electrolytes. The aim of this thesis was to develop rechargeable solid-state fluoride ion batteries working at room temperature. In addition, the thesis focused on the development of new electrode and electrolyte materials for fluoride ion batteries.

First section of study describes the synthesis and the characterization of new nanocrystalline fluorite type $Ba_{1-x}Sb_xF_{2+x}$ ($0.1 \leq x \leq 0.4$) compound. SbF_3-doped BaF_2 solid solutions were synthesized by mechanical milling, and their crystal structures were investigated by XRD measurements. The ionic conductivities of the solid solutions were obtained by impedance spectroscopy. Among all doped BaF_2 compounds, $Ba_{0.7}Sb_{0.3}F_{2.3}$ showed highest conductivity of 4.4×10^{-4} S·cm^{-1} at 160 °C. This value turned out to be higher than that of isostructural $Ba_{0.7}La_{0.3}F_{2.3}$. The enhanced conductivity in the SnF_2-doped BaF_2 compound might be an effect of the lone pair of electrons of Sb^{3+}. Additionally, electrochemical testing was carried out for the FIB cell using $Ba_{0.7}Sb_{0.3}F_{2.3}$ as cathode, Ce as anode and $La_{0.9}Ba_{0.1}F_{2.9}$ as the solid electrolyte separator.

Rechargeable solid-state FIBs working at room temperature was demonstrated using $BaSnF_4$ electrolyte which is described in the second section. Tetragonal $BaSnF_4$ was obtained by annealing of ball milled $BaSnF_4$ at 300 °C, and its ionic conductivity was investigated by impedance spectroscopy. $BaSnF_4$ provided an ionic conductivity of 3.5×10^{-4} S·cm^{-1} at RT, which is sufficient for RT FIB performance. Fluoride ion batteries were built using BiF_3 as cathode, and Zn and Sn as anodes. Two types of FIB systems such as $Sn/BaSnF_4/BiF_3$ and $Zn/BaSnF_4/BiF_3$ were investigated. The electrochemical analysis of FIB cells was carried out at various temperatures (25, 60, 100, and 150 °C) and current densities (10, 20 and 40 µA·cm^{-2}). At 25 °C, the Sn anode-based FIB cell delivered high capacity, whereas the Zn based system showed stable cycling performance. *Ex situ* XRD, SEM and EIS analyses were carried out on these FIB cells to investigate the mechanism of redox reaction.

The design and development of interlayer electrolytes for high potential FIBs is discussed in the third section. The interlayer electrolyte consists of a thin layer of $La_{0.9}Ba_{0.1}F_{2.9}$ and thick layer of $BaSnF_4$. Previously, FIBs were built utilizing $BaSnF_4$ as solid electrolyte, and Sn and Zn metals (low electropositive metals) as anodes due to limited electrochemical stability of $BaSnF_4$, which resulted in low operating voltage. To build high operating voltage FIBs, high electropositive metals (Ce, Mg, La) should be used as anodes, which are compatible with electrolytes like $La_{0.9}Ba_{0.1}F_{2.9}$, but ionic conductivity of these electrolytes is too low to be used for any kind of room-temperature FIBs. To mitigate both low electrochemical stability and low ionic conductivity, the interlayer electrolyte concept was derived. The use of low conductive $La_{0.9}Ba_{0.1}F_{2.9}$ as thin layer enhances the total conductivity of the pellet (compared to

pure $La_{0.9}Ba_{0.1}F_{2.9}$) while it physically isolates the less stable and highly conductive electrolyte ($BaSnF_4$) from the anode. The idea of using interlayer electrolyte enabled the demonstration of relatively high voltage FIBs working at room temperature, which was not feasible either with $BaSnF_4$ or $La_{0.9}Ba_{0.1}F_{2.9}$ electrolytes alone. The total conductivity of interlayer electrolyte was optimized by varying the thickness of $La_{0.9}Ba_{0.1}F_{2.9}$ layer. $La_{0.9}Ba_{0.1}F_{2.9}$ (<50 µm)/$BaSnF_4$ (<700 µm) which gave an ionic conductivity of $0.89 \cdot 10^{-5}$ $S \cdot cm^{-1}$ at RT, which is more than 1 order of magnitude higher compared to pure $La_{0.9}Ba_{0.1}F_{2.9}$ (0.4×10^{-6} $S \cdot cm^{-1}$). Furthermore, a relatively high potential solid-state FIB working at RT was demonstrated using $La_{0.9}Ba_{0.1}F_{2.9}$ (90 µm)/ $BaSnF_4$ (650 µm) as electrolyte, Ce as anode, and BiF_3 as cathode.

In the final section, the demonstration of Mg as reversible anode for rechargeable FIBs by using $LiPF_6$ as electrolyte is illustrated. The discharge and charge behavior of Mg was investigated in Mg/BiF_3 and Mg/SnF_2 electrode systems. Further, the electrochemical analyses of Mg+MgF_2/$LiPF_6$/BiF_3 and Mg+MgF_2/$LiPF_6$/SnF_2 cells were carried out and performed at a current density of 38 $\mu A \cdot cm^{-2}$. Both cells displayed similar capacity and cyclic performance. Discharge-charge testing, CV, and XRD results proved the fluorination/defluorination at the Mg anode applying a PF_6^- electrolyte systems.

Kokkuvõte

Toatemperatuuriliste fluoriidioon akude väljaarendamine

Tahkefaasilised fluoriidioon akud kerkisid esile liitiumijärgses ajastus kui ühed sobivad energiasalvestuse seadmete kandidaadid. Fluorioon akud (FIBs) võimaldavad kõrget erienergiat, temperatuurilist stabiilsust ning ohutust ja seda võimalikult madala hinnaga. Praegusel ajal on FIBs alane uurimistöö kasvufaasi alguses ning terve rida teemasid, mis puudutavad elektrolüütide ja elektroodide võimekuse parandamist, vajavad jätkuvalt edasiarendamist. Käesoleva väitekirja eesmärgiks oli välja arendada toatemperatuuril töötavad fluoriidioon akud. Lisaks keskenduti fluoriidioon akude elektroodide ja elektrolüütide uute materjalide väljatöötamisele.

Uurimistöö esimeses peatükis kirjeldatakse uut tüüpi nanokristallilise fluoriiti $Ba_{1-x}Sb_xF_{2+x}$ ($0.1 \leq x \leq 0.4$) tüüpi ainesegude sünteesi ja iseloomustamist. SbF_3-legeeritud BaF_2 tahke lahus sünteesiti mehhaanilise jahvatamisega ja selle kristallstruktuuri uuriti XRD mõõtmistega. Tahkete lahuste ioonset juhtivust hinnati impedants-spektroskoopia abil. Kõikidest legeeritud BaF_2 ainesegudest oli $Ba_{0.7}Sb_{0.3}F_{2.3}$ suurima juhtivusega 4.4×10^{-4} S·cm^{-1}, mis mõõdeti 160 °C juures. See juhtivuse väärtus on kõrgem isegi kui isostruktuursel $Ba_{0.7}La_{0.3}F_{2.3}$. SnF_2-legeeritud BaF_2 ainesegu suurenenud juhtivus võib olla tingitud Sb^{3+} üksiku elektronpaari efektist. Lisaks viidi läbi FIB elektrokeemilised testimised kasutades katoodina $Ba_{0.7}Sb_{0.3}F_{2.3}$, anoodina Ce ning tahke elektrolüüdina $La_{0.9}Ba_{0.1}F_{2.9}$.

Tahkefaasilise FIB töötamise demonstreerimist toatemperatuuril kasutades $BaSnF_4$ elektrolüüti on kirjeldatud teises peatükis. Tetragonaalne $BaSnF_4$ saadi kuubilise $BaSnF_4$ lõõmutamisel 300 °C juures (kuulveskis jahvatamisel) ning selle ioonset juhtivust uuriti impedants-spektroskoopia abil. $BaSnF_4$ ioonseks juhtivuseks mõõdeti 3.5×10^{-4} S·cm^{-1} toatemperatuuril, mis on piisav, et ehitada toatemperatuuril töötav FIB. Ehitati fluorioon akud kasutades katoodina BiF_3 ning anoodina Zn ja Sn. Uuriti kahte tüüpi FIB süsteeme: Sn/$BaSnF_4$/BiF_3 ning Zn/$BaSnF_4$/BiF_3. FIB rakkude elektrokeemiline analüüs viidi läbi erinevatel temperatuuridel (25, 60, 100, ning 150 °C) ja voolu tihedustel (10, 20 ning 40 µA·cm^{-2}). 25 °C juures ilmnes Sn anoodiga FIB rakkudel kõrge mahtuvus samal ajal kui Zn anoodiga FIB rakkudel oli parem tsükliline stabiilsus. Ex situ XRD, SEM ja analüüsid viidi läbi selleks, et uurida redoks reaktsiooni mehhanismi.

Kolmandas peatükis on toodud arutlus vahekihtide elektrolüütide disainimisest javäljatöötamisest kõrge potentsiaaliga FIBs jaoks. Vahekihi elektrolüüt koosneb õhukesest $La_{0.9}Ba_{0.1}F_{2.9}$ kihist ja paksust $BaSnF_4$ kihist. Enne seda ehitati FIBs kasutades tahke elektrolüüdina $BaSnF_4$ ning anoodina metallilisi Sn ja Zn (madala elektropositiivsusega metallid) piiratud $BaSnF_4$ elektrokeemilise stabiilsuse tõttu, mis põhjustas madala tööpinge. Kõrge tööpingega FIB ehitamiseks tuleb anoodina kasutada kõrge elektropositiivsusega metalle (Ce, Mg, and La), mis sobiksid elektrolüütidega nagu $La_{0.9}Ba_{0.1}F_{2.9}$ kuid nende elektrolüütide ioonjuhtivus on liiga madal, et neid oleks võimalik kuidagi rakendada toatemperatuurilistes FIAdes. Et vältida nii madalat elektrokeemilist stabiilsust kui ka madalat ioonjuhtivust võeti kasutusele vahekihi elektrolüüdi kontseptsioon. Kasutades madala juhtivusega $La_{0.9}Ba_{0.1}F_{2.9}$ õhukese kihina suurendas kogu pelleti juhtivust (võrrelduna puhta $La_{0.9}Ba_{0.1}F_{2.9}$-ga) kuna see samal ajal füüsiliselt isoleeris anoodist vähem stabiilse ja hästi juhtiva elektrolüüdi ($BaSnF_4$). Idee kasutada vahekihi elektrolüüti võimaldas demonstreerida suhteliselt kõrge pingega FIBs töötamist toatemperatuuril, mis ei oleks võimalik ainult eraldi elektrolüütidega $BaSnF_4$

ega $La_{0.9}Ba_{0.1}F_{2.9}$ korral. Vahekihi elektrolüüdi summaarset juhtivust optimeeriti varieerides $La_{0.9}Ba_{0.1}F_{2.9}$ kihi paksust. $La_{0.9}Ba_{0.1}F_{2.9}$ (<50 µm)/$BaSnF_4$ (<700 µm) ioonjuhtivus toatemperatuuril oli 0.89×10^{-5} $S \cdot cm^{-1}$, mis on rohkem kui suurusjärk suurem kui puhtal $La_{0.9}Ba_{0.1}F_{2.9}$ (0.4×10^{-6} $S \cdot cm^{-1}$). Enamgi veel, demonstreeriti suhteliselt kõrge potentsiaaliga tahkefaasilise FIB töötamist toatemperatuuril kasutades elektrolüüdina $La_{0.9}Ba_{0.1}F_{2.9}$ (90 µm)/ $BaSnF_4$ (650 µm), anoodiks Ce ning katoodiks BiF_3.

Viimases peatükis demonstreeritakse Mg kasutamist pööratava anoodina taaslaetavates FIBs kasutades illustratsiooniks elektrolüüdina $LiPF_6$. Mg käitumist tühjenemisel ja laadimisel uuriti Mg/BiF_3 ning Mg/SnF_2 elektroodide süsteemis. Seejärel viidi läbi Mg+MgF_2/$LiPF_6$/BiF_3 ja Mg+MgF_2/$LiPF_6$/SnF_2 rakkude analüüs voolutihedusel 38 $\mu A \cdot cm^{-2}$. Mõlemad rakud näitasid üles sarnast mahtuvuslikku ja tsüklilist võimekust. Tühjenemise-laadimise testimised, CV ja XRD tulemused tõendasid fluorineerumise/defluorineerumise toimumist Mg anoodil.

Appendix

Publication I

Mohammad, I.; Chable, J.; Witter, R.; Fichtner, M.; Reddy, M. A., Synthesis of Fast Fluoride-Ion-Conductive Fluorite-Type $Ba_{1-x}Sb_xF_{2+x}$ ($0.1 \leq x \leq 0.4$): A Potential Solid Electrolyte for Fluoride-Ion Batteries. *ACS Appl. Mater. Interfaces* 2018, *10,* 17249-17256.

https://pubs.acs.org/doi/pdf/10.1021/acsami.8b04108

ACS APPLIED MATERIALS & INTERFACES

Research Article

Cite This: *ACS Appl. Mater. Interfaces* 2018, 10, 17249−17256

www.acsami.org

Synthesis of Fast Fluoride-Ion-Conductive Fluorite-Type $Ba_{1-x}Sb_xF_{2+x}$ ($0.1 \leq x \leq 0.4$): A Potential Solid Electrolyte for Fluoride-Ion Batteries

Irshad Mohammad,[†,‡] Johann Chable,[‡] Raiker Witter,[†,§] Maximilian Fichtner,[‡,§] and M. Anji Reddy*[,‡]

[†]Technomedicum, Tallinn University of Technology, Ehitajate tee 5, 19086 Tallinn, Estonia
[‡]Helmholtz Institute Ulm (HIU) for Electrochemical Energy Storage, Helmholtz Str. 11, 89081 Ulm, Germany
[§]Institute of Nanotechnology (INT), Karlsruhe Institute of Technology (KIT), Hermann-von-Helmholtz-Platz 1, 76344 Eggenstein-Leopoldshafen, Germany

Supporting Information

ABSTRACT: Toward the development of high-performance solid electrolytes for fluoride-ion batteries, fluorite-type nanostructured solid solutions of $Ba_{1-x}Sb_xF_{2+x}$ ($x \leq 0.4$) were synthesized by high-energy ball-milling method. Substitution of divalent Ba^{2+} by trivalent Sb^{3+} leads to an increase in interstitial fluoride-ion concentration, which enhances the ionic conductivity of the $Ba_{1-x}Sb_xF_{2+x}$ ($0.1 \leq x \leq 0.4$) system. Total ionic conductivities of 4.4×10^{-4} and 3.9×10^{-4} S cm^{-1} were obtained for $Ba_{0.7}Sb_{0.3}F_{2.3}$ and $Ba_{0.6}Sb_{0.4}F_{2.4}$ compositions at 160 °C, respectively. In comparison to isostructural $Ba_{0.3}La_{0.7}F_{2.3}$, the ionic conductivity of $Ba_{0.7}Sb_{0.3}F_{2.3}$ is significantly higher, which is attributed to the presence of an electron lone pair on Sb^{3+}. Introduction of such lone pairs seems to increase fluoride-ion mobility in solid solutions. In addition, $Ba_{0.7}Sb_{0.3}F_{2.3}$ was tested as a cathode material against Ce and Zn anode using $La_{0.9}Ba_{0.1}F_{2.9}$ as the electrolyte. $Ba_{0.3}Sb_{0.7}F_{2.3}$/$La_{0.9}Ba_{0.1}F_{2.9}$/Ce cell showed high discharge and charge capacities of 301 and 170 mA h g^{-1}, respectively, in the first cycle at 150 °C.

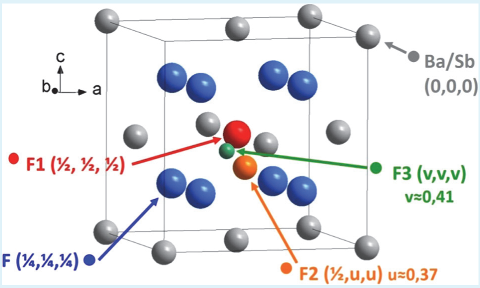

KEYWORDS: *fluoride-ion batteries, fluoride-ion conductors, ionic conductivity, fluorite-type fluorides, solid electrolyte, solid-state batteries*

INTRODUCTION

Batteries based on cation transport (Li^+, Na^+, and Mg^{2+}) are well known and widely investigated.[1−3] Solid-state batteries based on anion transport have been introduced recently and generated significant interest due to their high specific energy and flexibility in electrode compositions. Batteries based on fluoride transport were reported long ago.[4−6] However, it was largely overlooked until the recent demonstration of high-energy-density rechargeable fluoride-ion batteries (FIB).[7] Since then significant improvements have been made toward the development of FIBs, with focus on electrolyte[8−10] and electrode materials.[11,12] So far, FIBs have been operated at a temperature of 150 °C or above. Lower operating temperatures of FIBs are not possible at the moment due to the low ionic conductivity of the solid electrolytes at room temperature (RT). These limitations necessitate the search for fluoride-ion-transporting solid electrolytes with higher RT conductivities. In this way, several efforts were made to reduce the operating temperature of FIBs, e.g., by developing a less resistive dense thin-film-based electrolyte.[13,14]

Mainly two types of crystal structures are known to show high fluoride-ion conductivity: fluorite-type (MF_2, M = Ca, Ba, Sr) (SG: $Fm\overline{3}m$) and tysonite-type (MF_3, M = La, Ce, Pr, Nd) (SG: $P\overline{3}c1$) structures.[15−17] In the case of tysonite-type $La_{1-x}Ba_xF_{3-x}$ compounds, the ionic mobility is mainly due to the migration of fluoride vacancies.[17,18] In the case of fluorite-type $Ba_{1-x}La_xF_{2+x}$ compounds, ionic conductivity arises due to the migration of interstitial fluoride ions.[19,8,18] However, in the case of nanocrystalline fluorite-type $Ba_{1-x}La_xF_{2+x}$ compounds, the total conductivity is dominated by the grain boundaries, but the fluoride conduction mechanism is not clearly understood.[17] Rongeat et al. investigated the conductivity mechanisms in nanocrystalline fluorite- and tysonite-type compounds synthesized by mechanical milling.[8,17] Nanocrystalline, tysonite-type $La_{1-x}Ba_xF_{3+x}$ compounds showed less conductivity compared to the corresponding single crystals.[17] In contrast, nanocrystalline fluorite-type compounds showed higher conductivity than the corresponding single crystals, inconsistent with other studies.[20] Düvel et al. also investigated both the fluorite- and tysonite-type structures in $Ba_{1-x}La_xF_{2+x}$ synthesized by mechanochemical methods.[18] They have also made similar conclusions. As fluorite-type compounds show high ionic conductivity in the

Received: March 12, 2018
Accepted: April 27, 2018
Published: May 9, 2018

DOI: 10.1021/acsami.8b04108

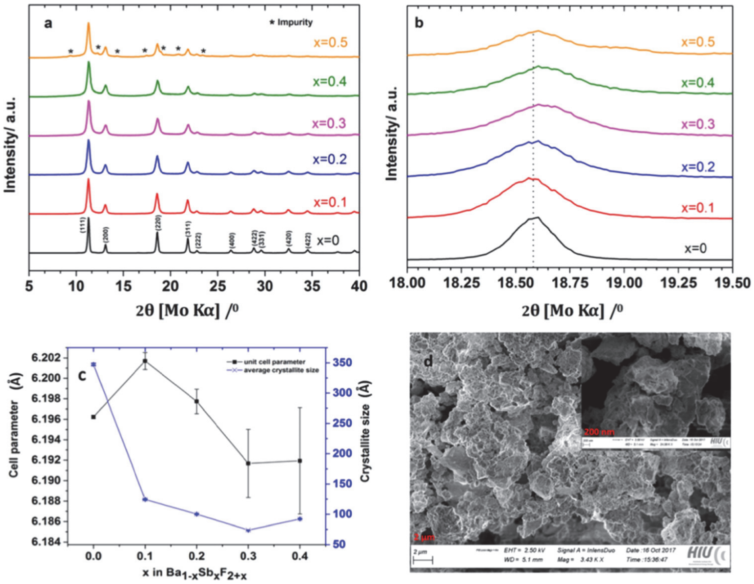

Figure 1. (a) XRD pattern of $Ba_{1-x}Sb_xF_{2+x}$ ($0 \leq x \leq 0.5$) composition, (b) enlargement of XRD pattern from 18 to 19.50 2θ values, (c) cell parameter and crystallite size plots of each amount of dopant x, and (d) scanning electron microscopy (SEM) image of $Ba_{0.7}Sb_{0.3}F_{2.3}$ with 2.0 μm magnification and inset image with 200 nm magnification.

nanocrystalline state (easy to integrate into solid-state battery), we chose to work on fluorite-type compounds in this study. Furthermore, the nanocrystalline fluorite-type solid solution can be easily synthesized by mechanical milling.[17,18,21]

Two strategies can be adopted to improve the ionic conductivity of fluorite-type compounds: homogeneous doping (by doping with aliovalent or isovalent ions) and heterogeneous doping (dispersing the second phase). Both methods were investigated to improve the ionic conductivity of fluorite-type compounds. In the case of CaF_2, ionic conductivity increased after grain boundary activation by Lewis acids. Lewis acids like SbF_5 and BF_3 can attract fluoride ions to create vacancies that promote fluoride-ion migration in the grain boundaries.[22] In the case of homogeneous doping, it has been reported that doping with monovalent fluorides (NaF or KF) produces fluoride vacancies, whereas doping with trivalent fluorides (LaF_3, CeF_3, or SmF_3) generates interstitial fluorine ions.[23,24] Addition of a small quantity of NaF or KF to pure BaF_2 resulted in a marginal increase in the ionic conductivity of BaF_2. However, doping with trivalent fluorides showed remarkable effects on the ionic conductivity, as investigated in a detailed study on BaF_2 doped with different rare-earth elements ($Ba_{1-x}R_xF_{2+x}$). Ivanov-Shits et al. synthesized $Ba_{1-x}R_xF_{2+x}$ by doping of BaF_2 with rare-earth metal fluorides RF_3.[25] The conductivity increased for all rare-earth elements with x (above percolation threshold) until a saturation stage at high concentration due to the decrease of activation energy. The highest conductivity has been observed for La-doped BaF_2, $\sigma_{200°C} = 1.9 \times 10^{-4}$ S cm^{-1} for $Ba_{0.6}La_{0.4}F_{2.4}$. Recently, Rongeat and co-workers have prepared nanocrystalline fluorite-type $Ba_{1-x}La_xF_{2+x}$ ($0 \leq x \leq 0.55$) compound and observed similar results. For nanocrystalline $Ba_{0.6}La_{0.4}F_{2.4}$, an ionic conductivity of 1.9×10^{-4} S cm^{-1} at 160 °C was observed.

Although it is rational to think that aliovalent ion doping (KF or LaF_3) can improve the ionic conductivity, the ionic conductivity of BaF_2 was improved by doping with isovalent fluorides.[26,27] In fact, SnF_2-doped BaF_2 shows much higher conductivity than either KF- or LaF_3-doped compounds. Thanks to the lone pair of electrons on SnF_2, which strongly influences the fluoride sublattice and contributes to the high fluoride-ion conductivity in $BaSnF_4$.[28,29] As a consequence, some of Sn^{2+}-containing compounds like $MSnF_4$ (M = Pb, Ba, Sr) show the highest fluoride-ion conductivities at room temperature (RT).[28−30] Apart from Sn^{2+}, there are other cations (Sb^{3+}, Bi^{3+}, Pb^{2+}, Tl^{+}), which carry the lone pair of electrons and are assumed to have a similar effect on ionic conductivity. In this scenario, it is interesting to see the effect of SbF_3 doping in BaF_2. Sb^{3+}, being an aliovalent cation (to Ba^{2+}) and carrying a lone pair of electrons, might strongly contribute to enhancing the ionic conductivity of BaF_2. Hence, for the first time, we have investigated the effect of SbF_3 doping on the ionic conductivity of BaF_2. Nanocrystalline $Ba_{1-x}Sb_xF_{2+x}$ ($0.1 \leq x \leq 0.4$) solid solutions were synthesized by mechanical milling, and their phase purity was determined by X-ray diffraction (XRD). The ionic conductivity of the solid solutions was investigated by electrochemical impedance spectroscopy (EIS). The electrochemical cycling performance of FIB using $Ba_{0.7}Sb_{0.3}F_{2.3}$ as cathode, Ce and Zn as anode, and $La_{0.9}Ba_{0.1}F_{2.9}$ as solid electrolyte was also investigated.

■ EXPERIMENTAL SECTION

Synthesis. BaF_2 (99.9%), LaF_3 (anhydrous, 99.9% rare-earth oxides), and multiwalled carbon nanotubes (MWCNTs) (95%) were purchased from Sigma-Aldrich. CaF_2 (99.7%), SrF_2 (99%), and SbF_3 (99.6%) were purchased from Alfa Aesar. High-energy mechanical milling was used to synthesize $Ba_{1-x}Sb_xF_{2+x}$ ($0 \leq x \leq 0.5$). Before milling, the precursors were dried for 15 h under vacuum at 200 °C to remove the adsorbed moisture. All compositions were prepared by mechanical milling of a mixture of stoichiometric amounts of BaF_2 and SbF_3 for 18 h at 600 rpm under argon atmosphere. The ball-to-powder weight ratio was kept constant at 12:1. Silicon nitride jars (volume, 80 mL) and 20 balls (diameter, 10 mm) were used as milling media. Milling was performed using a planetary-type mill (FRITSCH Pulverisette 6). $Ba_{0.7}La_{0.3}F_{2.3}$ was produced according to a previous report[8] by ball milling stoichiometric amounts of BaF_2 and LaF_3 for 18 h at 600 rpm. For fabricating the cells, $La_{0.9}Ba_{0.1}F_{2.9}$ was used as electrolyte and the synthesis of this material was done based on a previous report.[17] The electrolyte was synthesized by milling LaF_3 and BaF_2 at 600 rpm for 12 h, and the cathode was prepared by mixing $Ba_{0.7}Sb_{0.3}F_{2.3}$ (90 wt %) and MWCNT (10 wt %). The Ce anode composite was prepared by gentle milling of Ce powder (90 wt %) and MWCNT (10 wt %) at 200 rpm for 3 h. The Zn anode composite was prepared by mixing Zn powder (40 wt %), $La_{0.9}Ba_{0.1}F_{2.9}$ (50 wt %), and MWCNT (10 wt %) at 300 rpm for 12 h.

Characterization. X-ray diffraction (XRD) patterns of the educts and the as-milled powders were recorded using a STOE STADI-P instrument with Mo Kα source. Profile matching refinements were performed on the XRD patterns for cell parameters determination, using the Le Bail method with the FullProf software.[31] Instrumental broadening was taken into account using LaB_6 reference diffraction data. The sample contribution to X-ray line broadening was calculated by using the Thompson−Cox−Hastings pseudo-Voigt function that includes both size and strain-broadening terms for Lorentzian and Gaussian components.[32] The apparent crystallite size and the upper limit of microstrain are then internally calculated by FullProf using Langford's method.[33]

The electronic conductivity was measured by chronoamperometry at a constant voltage of 2.0 V using a Bio-Logic VMP 3 instrument. The surface morphology of powdered samples was investigated using a ZEISS LEO 1530 scanning electron microscope.

Electrochemical Impedance Spectroscopy (EIS). Zahner IM6 device was used to record DC impedance spectra, and ZView software was used for fitting the measured impedance. The frequency range was 8 MHz to 1.0 Hz, and the voltage amplitude was 10 mV. Impedance spectra were recorded at 25, 60, 80, 100, 120, 140, 160, 180, and 200 °C under Ar atmosphere. For impedance measurements, 7 mm diameter pellets were pressed with a 2 ton force for 1 min and both sides coated with Au layer (thickness, 15 nm) as ion-blocking electrodes. The thickness of all pellets was approximately 0.8 mm.

Cell Assembly. Full cells were assembled under a protective atmosphere (Ar) by pressing the powders of the cathode, electrolyte, and the anode together, with the cathode on top and the electrolyte in-between. Enough material was introduced to avoid any short circuit. The three-layer pellet was inserted in a modified Swagelok-type cell, which is compatible to operate at elevated temperatures. Electrochemical cycling of the cells was performed using Arbin battery tester. The cells were cycled at 150 °C and a current density of 10 μA cm^{-2} within the voltage window of 1.0−3.5 V. The capacities were calculated referring to the weight of the active material SbF_3 in the cathode $Ba_{0.7}Sb_{0.3}F_{2.3}$.

RESULTS AND DISCUSSION

Structural Evolution of $Ba_{1-x}Sb_xF_{2+x}$ $(0 \leq x \leq 0.5)$.

$Ba_{1-x}Sb_xF_{2+x}$ $(0 \leq x \leq 0.5)$ solid solutions were synthesized by mechanical milling of stoichiometric mixtures of BaF_2 and SbF_3, as detailed in Experimental Section. The XRD patterns of all compounds are given in Figure 1a. Phase-pure fluorite-type compounds were obtained after 18 h of milling for $x < 0.5$. For higher doping content, reflections corresponding to demixing of SbF_3 were observed, indicating the solubility limit of the solid solution. With the increase of dopant concentration, overall shifts of the reflection positions toward higher angles were observed for all of the compositions, except for $Ba_{0.9}Sb_{0.1}F_{2.1}$, where the shift is very little in the other direction, toward lower angles (Figure 1b; reflection at ≈18.5°). This was unexpected considering the smaller size of Sb^{3+} (0.76 Å in 6-fold coordination in SbF_3) compared to Ba^{2+} (1.35 and 1.42 Å in 6- and 8-fold coordination, respectively),[34] which should lead to the decrease of a cell parameter and a position shift toward higher angles. The lattice parameter of $Ba_{0.8}Sb_{0.2}F_{2.2}$ is larger compared to that of BaF_2 but smaller than that of $Ba_{0.9}Sb_{0.1}F_{2.1}$. However, for $x = 0.3$ and 0.4, the smaller Sb^{3+} outweighs the effect of interstitial fluoride ions. Rongeat et al. investigated the nanocrystalline fluorite-type $Ba_{1-x}La_xF_{2+x}$ system, where a gradual reduction of lattice parameter was observed due to the substitution of smaller La^{3+} in place of larger Ba^{2+}.[8] However, in the case of Sb^{3+} substitution, lattice parameter increased initially ($Ba_{0.9}Sb_{0.1}F_{2.1}$ and $Ba_{0.8}Sb_{0.2}F_{2.2}$) and then decreased ($Ba_{0.7}Sb_{0.3}F_{2.3}$ and $Ba_{0.6}Sb_{0.4}F_{2.4}$) relative to BaF_2. These results suggest that there is a strong interplay between the interstitial occupancy of fluoride ions, dopant cation size, and lone pair of electrons. In the case of $Ba_{0.5}Sb_{0.5}F_{2.5}$, some extra reflections were observed, besides the reflections corresponding to the fluorite-type structure (marked *). Due to the presence of impurities, we have not calculated the lattice parameters of $Ba_{0.5}Sb_{0.5}F_{2.5}$. In the case of LaF_3-doped BaF_2 compounds, it was possible to achieve high doping level like $x \geq 0.5$,[8] but for SbF_3, doping level is limited to $x < 0.5$. This indicates that even with less amount of SbF_3 doping more interstitial sites are occupied, which could be due to the effect of lone pair of electrons on Sb^{3+}, which will repel the negatively charged fluoride ions and push them to occupy other/more interstitial sites than required by the stoichiometry. This might

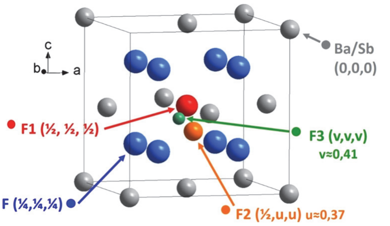

Figure 2. Representative structural view of $Ba_{1-x}Sb_xF_{2+x}$ (doped fluorite).

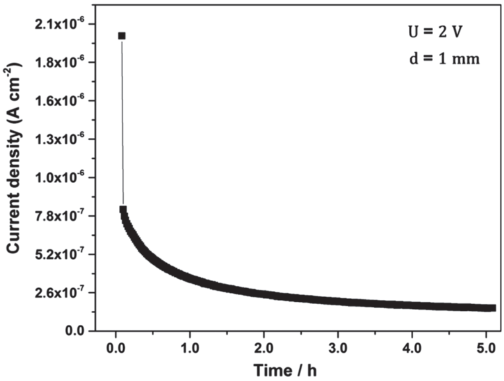

Figure 3. Chronoamperometry of the $Ba_{0.6}Sb_{0.4}F_{2.4}$ compound at 25 °C for 5 h.

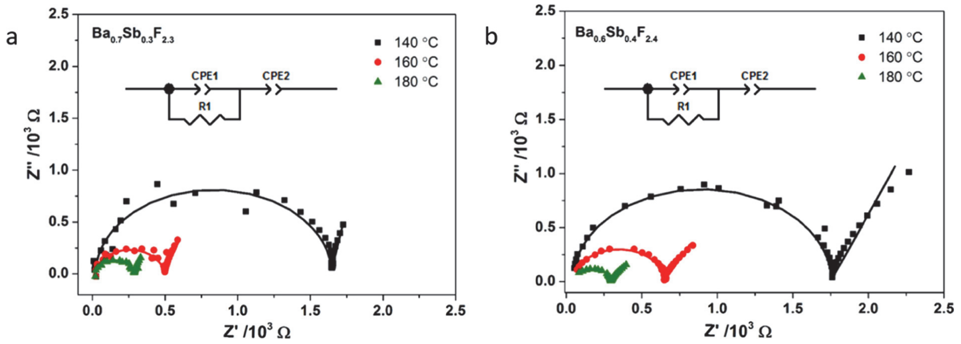

Figure 4. Nyquist plots of (a) $Ba_{0.7}Sb_{0.3}F_{2.3}$ and (b) $Ba_{0.6}Sb_{0.4}F_{2.4}$ obtained at different temperatures (symbols) and the corresponding fit (lines). The equivalent circuits used for the fit are shown in the insets.

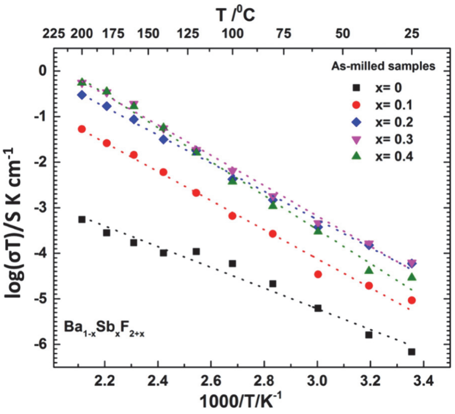

Figure 5. Arrhenius plots of ionic conductivity of ball-milled $Ba_{1-x}Sb_xF_{2+x}$ ($0 \leq x \leq 0.4$) compounds. The symbols are conductivities measured from impedance measurements, and the dotted lines denote the linear fit obtained for calculating activation energies.

also explain the initial increase of lattice parameter in the case of $Ba_{0.9}Sb_{0.1}F_{2.1}$ and $Ba_{0.8}Sb_{0.2}F_{2.2}$. However, further structural characterizations are required to validate these hypotheses.

In fluorite-type structures (Figure 2), cations (here Ba and Sb, represented in gray) form an face-centered cubic network, in which the anions occupy all tetrahedral sites (here F, in blue). This arrangement results in the formation of FCa4 polyhedra. Earlier studies on rare-earth-doped fluorite-type compounds indicated that the extra fluoride ions occupy different interstitial positions, depending on the dopant concentration. The interstitial positions can be denoted as F1, F2, and F3 (marked in red, orange, and green, respectively, in Figure 2).[35,36] The most obvious interstitial position is the F1 site, of cubic symmetry, located at (1/2, 1/2, 1/2) between the eight equivalent fluorine ions (F site in blue). The F2 position is displaced along the ⟨110⟩ direction, and the F3 position along the ⟨111⟩ direction. Hypothetical fourth F4 (w,w,w with $w = 0.31$) interstitial position has also been reported, but this is merely an off-center shift of the anions from the ideal site of fluorine ions F (1/4, 1/4, 1/4).[37] This F1 site and its 12 equivalent positions (middle of the cubic edges) are solely populated at low dopant concentrations, until $x = 0.05$.[35] At higher dopant concentrations, F2 and F3 interstitial sites are being occupied.[36] Further, an increase of these sites population facilitates the formation of fluoride clusters in the structure, which have dominating influence on the evolution of the conductivity with increased doping. For example, high dopant concentration can lead to the formation of antiprisms, which will trap fluoride ions located on the F2 site.[38] Formation of F^- clusters leads to decrease in the total conductivity of rare-earth-doped fluorite-type compounds, above a certain threshold, as mentioned above and will be discussed later. However, further structural characterization is necessary to fully understand the local structure of $Ba_{1-x}Sb_xF_{2+x}$ compounds.

Table 2. Values of Fitted Parameters of the Equivalent Circuit for $Ba_xSb_{1-x}F_{2+x}$

sample	$Ba_{1-x}Sb_xF_{2+x}$				
x	0	0.1	0.2	0.3	0.4
R_1 at 160 °C (10^2 Ω)	5393.68	72.9	12.33	4.61	5.97
CPE1 at 160 °C (10^{-10} F s^{a-1})	3.52	7.85	2.91	10.78	3.05
CPE2 at 160 °C (10^{-6} F s^{a-1})	1.95	4.62	5.83	10.14	31.89

Table 1. Results of Profile Matching Refinements and Conductivity Parameters for $Ba_{1-x}Sb_xF_{2+x}$ and $Ba_{0.7}La_{0.3}F_{2.3}$

sample	$Ba_{1-x}Sb_xF_{2+x}$					$Ba_{0.7}La_{0.3}F_{2.3}$
x	0	0.1	0.2	0.3	0.4	
cell parameter (Å)	6.196	6.201	6.197	6.191	6.191	6.111
crystallite size (nm)	34.73	12.45	10.01	7.39	9.23	17.59
σ at 160 °C (10^{-4} S cm^{-1})	0.0039	0.333	1.98	4.41	3.89	1.55
E_a (eV)	0.45	0.63	0.61	0.66	0.73	0.57
σ_0 (10^5 S K cm^{-1})	0.0003	2.75	10.23	64.00	489.77	2.26

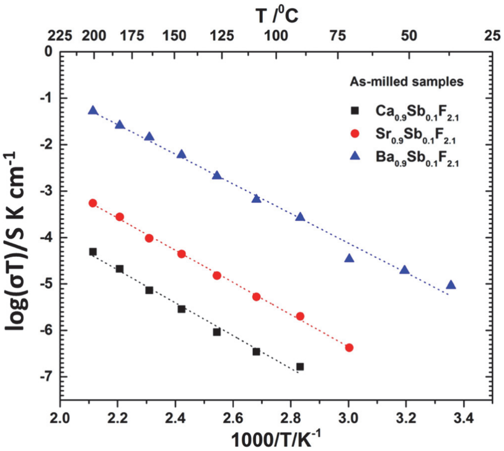

Figure 6. Arrhenius plot of ionic conductivities of ball-milled $Ca_{0.9}Sb_{0.1}F_{2.1}$ and $Sr_{0.9}Sb_{0.1}F_{2.1}$ compounds compared to $Ba_{0.9}Sb_{0.1}F_{2.1}$. The symbols represent the measured data, and the dotted lines denote the linear fit, which was used to calculate activation energies.

Microstructural information on the $Ba_{1-x}Sb_xF_{2+x}$ ($0 \leq x < 0.5$) samples was also obtained and is shown in Figure 1c. The calculated average crystallite sizes for all compositions were in the 7−15 nm range, except for pure BaF_2, whose average crystallite size was 35 nm. It is interesting to note that the average crystallite size decreases with SbF_3 doping, but its cause is not clear yet. To investigate the primary particle size and the morphology, SEM images of $Ba_{0.7}Sb_{0.3}F_{2.3}$ were collected and are shown in Figure 1d. Primary particle size was in the 2.0−5.0 μm range, with the small crystallites being aggregated to form bigger particles, which is typical for ball-milled samples.

Ionic Conductivity of $Ba_{1-x}Sb_xF_{2+x}$ Compounds. Electronic and ionic conductivities of $Ba_{1-x}Sb_xF_{2+x}$ ($0 \leq x < 0.5$) solid solutions were investigated to evaluate the potential of these new compounds as fluoride-ion conductors. To determine the electronic conductivity, chronoamperometry measurements were performed by applying a constant potential of 2.0 V on pellets $Ba_{1-x}Sb_xF_{2+x}$ ($0 \leq x \leq 0.4$) and measuring the current as a function of time. Figure 3 illustrates for $x = 0.4$ the behavior of measured current versus time when a potential of 2.0 V was applied. During the start of the measurement, the current quickly fell to lower values, which can be assigned to the polarization of the material.[39] After that, the current density gradually decreased to reach an asymptotic value around 2.6×10^{-7} A cm^{-2}, obtained after 5 h of measurement when the electronic conductivity was completely relaxed. The electronic conductivity of the material was then calculated using eq 1

$$\sigma_{el} = I \cdot d / UA \qquad (1)$$

where I is the current, U is the applied potential, d is the pellet thickness, and A is the area of the pellet. The obtained electronic conductivity value is 7.8×10^{-9} S cm^{-1}, which is much lower than that of metals or semiconductors,[40] indicating the electronic insulating behavior of these new $Ba_{1-x}Sb_xF_{2+x}$ solid solutions.

Electrochemical impedance spectroscopy (EIS) was used to determine the ionic conductivity of $Ba_{1-x}Sb_xF_{2+x}$ ($0 \leq x < 0.5$) solid solutions. Complex impedance spectra of $Ba_{0.7}Sb_{0.3}F_{2.3}$ and $Ba_{0.6}Sb_{0.4}F_{2.4}$ obtained at different temperatures are shown in Figure 4a,b. The spectra consist of a half-circle at high frequency (MHz) and a straight line at low frequency (Hz), which represents the charging of ionic species at the electrolyte−electrode interface.[41,42] Similar EIS patterns were observed for all other compositions (Supporting Information, Figure S8). The total resistance of the system corresponds to the real part of the complex impedance and is determined at the intercept of the measured spectra with the x-axis at low frequency. Fitting of the measured spectra with the help of equivalent circuits has been developed to get a precise resistance value.[43] An equivalent circuit (inset in Figure 4) composed of two constant phase elements (CPE1 and CPE2) and an Ohmic resistor (R_1) was used to fit the impedance data. CPE1 and CPE2 represent capacitive properties of one part of a sample (bulk or grain boundaries), whereas the resistor represents its bulk resistive properties. The ionic conductivity σ of the electrolyte was calculated according to eq 2

$$\sigma = d / AR_1 \qquad (2)$$

where d stands for pellet thickness and A stands for its area.

Fitting curves (shown with solid lines) and measured plots (symbols) match quite well (Figure 4). For all compositions, the overall resistance decreases with temperature, indicating a

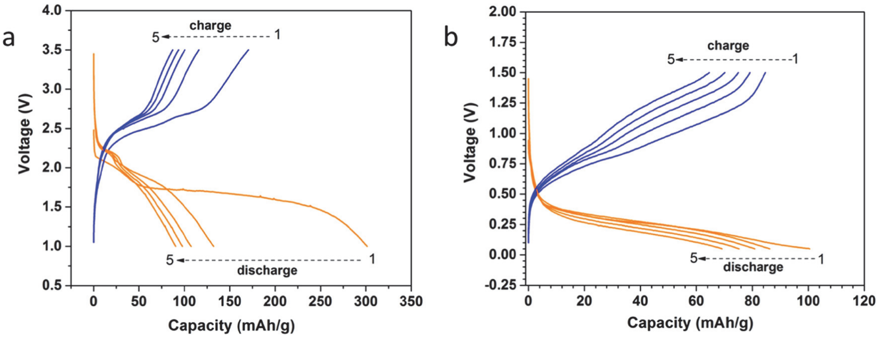

Figure 7. Voltage-composition profiles obtained at 150 °C with a current density of 10 μA cm^{-2} for the first five cycles of (a) $Ba_{0.7}Sb_{0.3}F_{2.3}/La_{0.9}Ba_{0.1}F_{2.9}/Ce$ and (b) $Ba_{0.7}Sb_{0.3}F_{2.3}/La_{0.9}Ba_{0.1}F_{2.9}/Zn$ cells.

conductivity increase ($\sigma \propto 1/R$, eq 2). The calculated ionic conductivity of $Ba_{1-x}Sb_xF_{2+x}$ ($0 \leq x \leq 0.4$) solid solutions is shown in Figure 5. As for many other ionic conductors, $\ln(\sigma T)$ evolves linearly vs $1/T$, indicating that the ionic conductivity is following an Arrhenius-like law (eq 3)

$$\sigma \times T = \sigma_0 \times e^{-(E_a/kT)} \tag{3}$$

where E_a, k, and σ_0 stand for the activation energy, the Boltzmann constant, and the preexponential factor, respectively. Calculated $-E_a/k$ and $\ln(\sigma_0)$ correspond to slope and intercept, respectively. As can be observed in Figure 5, the ionic conductivity of $Ba_{1-x}Sb_xF_{2+x}$ solid solutions increased with the dopant concentration and seemed to reach a broad maximum of $0.2 \leq x \leq 0.4$. At low temperature, the ionic conductivity of $Ba_{0.6}Sb_{0.4}F_{2.4}$ is slightly lower than that of $Ba_{0.8}Sb_{0.2}F_{2.2}$ and $Ba_{0.7}Sb_{0.3}F_{2.3}$, and at high temperatures, the ionic conductivity of $Ba_{0.8}Sb_{0.2}F_{2.2}$ is slightly lower than that of $Ba_{0.7}Sb_{0.3}F_{2.3}$ and $Ba_{0.6}Sb_{0.4}F_{2.4}$. Doping above $x = 0.3$ does not seem to increase the ionic conductivity further, which is in good agreement with structural considerations of interstitials F^- ions trapped in defects clusters.[40] However, the change in conductivity was marginal within all SbF_3-doped samples. The maximum conductivity was obtained for the sample $Ba_{0.7}Sb_{0.3}F_{2.3}$, which was 4.4×10^{-4} S cm^{-1} at 160 °C. Activation energies for every composition were calculated using the slope of their linear fit and compared in Table 1 as well as their ionic conductivity at 160 °C.

Impedance spectra were further analyzed to identify grain and grain boundary contributions to the ionic conductivity of $Ba_{1-x}Sb_xF_{2+x}$ ($0 \leq x < 0.5$). The impedance spectra shapes of our polycrystalline samples are similar to those of polycrystalline fluorite-type samples, but very different from those of polycrystalline tysonite-type samples.[8,17] Tysonite-like compounds contain two half-circles at high frequencies related to bulk phenomena and grain boundaries and one straight line at low frequencies related to the electrode−electrolyte interface,[9,13] whereas fluorite-like compounds display only one semicircle.[8] For our spectra, if resistance values depended upon sample composition as well as temperature, capacitance values were almost similar for all compositions and slightly change with temperature, based on the data extracted from the fits with the equivalent circuit. Capacitance data corresponding to the first semicircle (CPE1) are close to 10^{-10} F, and those corresponding to the straight line (CPE2) are in the range of 10^{-6}−10^{-5} F (Table 2). The CPE1 values are consistent with grain boundaries phenomena (10^{-11}−10^{-8} F), and the CPE2 values are consistent with sample−electrode interfaces phenomena (10^{-7}−10^{-5} F).[44]

The absence of a semicircle corresponding to bulk phenomena has been explained by the short-circuiting of bulk resistance by the lower resistance along the grain boundaries.[8] Consequently, the bulk contribution is surpassed by grain boundaries contribution resulting in only one semicircle. The ionic conductivities of the ball-milled samples are then mostly governed by diffusion along the grain boundaries. More precisely, Rongeat et al. concluded that if the defects present in bulk (interstitials F^- ions) do not contribute directly to the conduction, then they probably influence the defects present in the grain boundaries (vacancies).[8] According to the data presented above, it is possible that a similar mechanism is valid for the $Ba_{1-x}Sb_xF_{2+x}$ compounds. To compare the results of the $Ba_{1-x}Sb_xF_{2+x}$ compounds to those reported for $Ba_{0.7}La_{0.3}F_{2.3}$, we have produced this material in the same manner as described in the previous report.[8] Compared to $Ba_{0.7}La_{0.3}F_{2.3}$, the ionic conductivity of $Ba_{0.7}Sb_{0.3}F_{2.3}$ is nearly double at 160 °C (Table 2), which means that an additional contribution to the conductivity might indeed be coming from the presence of lone pair of electrons on Sb^{3+}. Thoroughly examining the local atomic environments in both structures could be the key to understand the origin of this ionic conductivity improvement.

The influence of alkaline-earth cations on the ionic conductivity was also evaluated through the synthesis and characterizations of $Ca_{1-x}Sb_xF_{2+x}$ and $Sr_{1-x}Sb_xF_{2+x}$ ($0 \leq x < 0.5$) solid solutions. In these cases, the solid solution formation was seemingly possible only for a lower amount of dopant (SbF_3), i.e., for $x \leq 0.1$ with Ca and for $x \leq 0.3$ with Sr (Supporting Information, Figures S6 and S7). The $Sr_{0.9}Sb_{0.1}F_{2.1}$ and $Ca_{0.9}Sb_{0.1}F_{2.1}$ compounds were thus selected for comparison with the Ba counterpart. Impedance spectra of $Sr_{0.9}Sb_{0.1}F_{2.1}$ and $Ca_{0.9}Sb_{0.1}F_{2.1}$ exhibited one semicircle at high frequency (MHz) and one straight line at low frequency (Hz), looking similar to that of $Ba_{0.9}Sb_{0.1}F_{2.1}$. However, the resistance measured was systematically higher compared to that of $Ba_{0.9}Sb_{0.1}F_{2.1}$. The corresponding calculated ionic conductivities of $Ca_{0.9}Sb_{0.1}F_{2.1}$ and $Sr_{0.9}Sb_{0.1}F_{2.1}$ at 160 °C are 1.7×10^{-8} and 2.2×10^{-7} S cm^{-1}, respectively. These conductivity values are 2 or 3 orders of magnitude lower than those of their Ba analogues (Figure 6 and Table 1), although they possess similar crystal structure. This is in good agreement with previous reports on SrF_2 or CaF_2 and their doped compounds, which showed lower conductivity than their Ba counterparts.[45] The calculated values of activation energies were 0.70, 0.68, and 0.63 eV for $Ca_{0.9}Sb_{0.1}F_{2.1}$, $Sr_{0.9}Sb_{0.1}F_{2.1}$, and $Ba_{0.9}Sb_{0.1}F_{2.1}$ compounds, respectively.

As the ionic conductivity of $Ba_{0.7}Sb_{0.3}F_{2.3}$ is high, this compound could be interesting as an electrolyte in FIB. However, the cycling was not possible using $Ba_{0.7}Sb_{0.3}F_{2.3}$ as electrolyte due to the low electrochemical stability of Sb^{3+} (versus Ce anode). Therefore, $Ba_{0.7}Sb_{0.3}F_{2.3}$ was rather used as cathode material (in a composite with carbon nanotubes) with high intrinsic fluoride-ion conductivity. Tysonite-type $La_{0.9}Ba_{0.1}F_{2.9}$ was used as an electrolyte, and Ce and Zn as anode materials. The galvanostatic charge−discharge profiles of the cells for the first five cycles are shown in Figure 7 (obtained at a current density of 10 μA cm^{-2}). The capacities presented here correspond to the weight percent of SbF_3 in the cathode. The first discharge capacity of the Ce-based cell amounts to 301 mA h g^{-1} at an average voltage of 1.7 V. This value represents only 66% of the theoretical specific capacity of SbF_3 (450 mA h g^{-1}), but is still higher than the one reported with the BiF_3 cathode.[7] The lower discharge capacity suggests that incomplete reaction occurred at cathode due to the presence of isolated grains of active material not sufficiently connected by mass and/or electron transfer, which remains to be confirmed. The first charge curve shows a capacity of 170 mA h g^{-1}, which corresponds to 56% of the first discharge capacity. The huge difference between the first discharge and charge capacities is most probably due to the large volume changes in the electrode materials. In situ TEM studies on fluoride-ion batteries show that volume changes in the electrode material will lead to the delamination of the electrode and electrolyte layers at the interface and the isolation of the active material ionically and electronically.[46] Thereby, less active material is available for the reaction during subsequent charge and cycling. Zn-based cells show low-voltage plateau due to the lower reduction potential

DOI: 10.1021/acsami.8b04108
ACS Appl. Mater. Interfaces 2018, 10, 17249−17256

of Zn compared to Ce. They also show less capacity compared to Ce-based cells, but better cycling stability.

CONCLUSIONS

The SbF_3-doped BaF_2 solid solutions were synthesized by mechanical milling, and the ionic conductivities of $Ba_{1-x}Sb_xF_{2+x}$ compounds were measured by impedance spectroscopy. The highest conductivity of 4.4×10^{-4} S cm^{-1} at 160 °C was obtained for $Ba_{0.7}Sb_{0.3}F_{2.3}$. This conductivity value is double than that of the LaF_3-doped analogue. The increased conductivity of $Ba_{0.7}Sb_{0.3}F_{2.3}$, compared to $Ba_{0.7}La_{0.3}F_{2.3}$, might be an effect of the lone pair of electrons of Sb^{3+} instead. Similar to earlier studies on polycrystalline-doped BaF_2, the ionic conductivity in $Ba_{1-x}Sb_xF_{2+x}$ compounds is considered to proceed through the migration of vacancies along the grain boundaries. Further, the lone pair on Sb^{3+} seems to have a positive influence on fluoride-ion conductivity. However, at present, we are uncertain about the exact role of the effect of the lone pair. A further study about the role of lone pair might be helpful for further conductivity improvement. We also showed that the carbon−$Ba_{0.7}Sb_{0.3}F_{2.3}$ composite could be used as cathode material for fluoride-ion batteries against multiple anode materials (Ce, Zn).

ASSOCIATED CONTENT

Supporting Information

The Supporting Information is available free of charge on the ACS Publications website at DOI: 10.1021/acsami.8b04108.

> Observed and calculated XRD patterns of as-ball-milled $Ba_{1-x}Sb_xF_{2+x}$ ($0 \leq x < 0.5$); XRD patterns of as-ball-milled $Ca_{0.9}Sb_{0.1}F_{2.1}$ and $Ca_{0.8}Sb_{0.2}F_{2.2}$; XRD patterns of as-ball-milled $Sr_{0.9}Sb_{0.1}F_{2.1}$, $Sr_{0.8}Sb_{0.2}F_{2.2}$, and $Sr_{0.7}Sb_{0.3}F_{2.3}$; and observed and fitted Nyquist plots of $Ba_{0.9}Sb_{0.1}F_{2.1}$, $Ba_{0.8}$ $Sb_{0.2}F_{2.2}$, and $Ba_{0.7}Sb_{0.3}F_{2.3}$ at 160 °C (PDF)

AUTHOR INFORMATION

Corresponding Author

*E-mail: munnangi.reddy@kit.edu.

ORCID

M. Anji Reddy: 0000-0001-9101-0252

Notes

The authors declare no competing financial interest.

ACKNOWLEDGMENTS

The authors acknowledge financial support from the European Union through the European Regional Development Fund (Dora Plus Action 1) and Estonian Ministry of Education and Research through Grant PUT1534. They gratefully thank Tobias Braun, Helmholtz Institute Ulm, for assisting in the SEM measurements. R.W. acknowledges Tallinn University of Technology and Karlsruhe Institute of Technology.

REFERENCES

(1) Tarascon, J. M.; Armand, M. Issues and Challenges Facing Rechargeable Lithium Batteries. *Nature* **2001**, *414*, 359−367.

(2) Hasa, I.; Buchholz, D.; Passerini, S.; Scrosati, B.; Hassoun, J. High Performance $Na_{0.5}[Ni_{0.23}Fe_{0.13}Mn_{0.63}]O_2$ Cathode for Sodium-Ion Batteries. *Adv. Energy Mater.* **2014**, *4*, No. 1400083.

(3) Zhao-Karger, Z.; Zhao, X. Y.; Wang, D.; Diemant, T.; Behm, R. J.; Fichtner, M. Performance Improvement of Magnesium Sulfur Batteries with Modified Non-Nucleophilic Electrolytes. *Adv. Energy Mater.* **2015**, *5*, No. 1401155.

(4) Baukal, W. *Ger. Offen.* 1971, GWXXBX DE 2017128.

(5) Kennedy, J. H.; Hunter, J. C. Thin Film Galvanic Cell $Pb/PbF_2/PbF_2$, CuF_2/Cu. *J. Electrochem. Soc.* **1976**, *123*, 10−14.

(6) Schoonman, J. A Solid-State Galvanic Cell with Fluoride-Conducting Electrolytes. *J. Electrochem. Soc.* **1976**, *123*, 1772−1775.

(7) Reddy, M. A.; Fichtner, M. Batteries Based on Fluoride Shuttle. *J. Mater. Chem.* **2011**, *21*, 17059−17062.

(8) Rongeat, C.; Reddy, M. A.; Witter, R.; Fichtner, M. Nanostructured Fluorite-Type Fluorides As Electrolytes for Fluoride Ion Batteries. *J. Phys. Chem. C* **2013**, *117*, 4943−4950.

(9) Dieudonné, B.; Chable, J.; Body, M.; Legein, C.; Durand, E.; Mauvy, F.; Fourcade, S.; Leblanc, M.; Maisonneuve, V.; Demourgues, A. The Key Role of the Composition and Structural Features in Fluoride Ion Conductivity in Tysonite $Ce_{1-x}Sr_xF_{3-x}$ Solid Solutions. *Dalton Trans.* **2017**, *46*, 3761−3769.

(10) Dieudonné, B.; Chable, J.; Mauvy, F.; Fourcade, S.; Durand, E.; Lebraud, E.; Leblanc, M.; Legein, C.; Body, M.; Maisonneuve, V.; Demourgues, A. Exploring the $Sm_{1-x}Ca_xF_{3-x}$ Tysonite Solid Solution as a Solid-State Electrolyte: Relationships between Structural Features and F^- Ionic Conductivity. *J. Phys. Chem. C* **2015**, *119*, 25170−25179.

(11) Rongeat, C.; Reddy, M. A.; Diemant, T.; Behm, R. J.; Fichtner, M. Development of New Anode Composite Materials for Fluoride Ion Batteries. *J. Mater. Chem. A* **2014**, *2*, 20861−20872.

(12) Nowroozi, M. A.; Ivlev, S.; Rohrer, J.; Clemens, O. La_2CoO_4: A New Intercalation Based Cathode Material For Fluoride Ion Batteries with Improved Cycling Stability. *J. Mater. Chem. A* **2018**, *6*, 4658−4669.

(13) Zhang, L.; Anji Reddy, M.; Gao, P.; Fichtner, M. Development of Dense Solid State Thin-Film Electrolyte for Fluoride Ion Batteries. *J. Alloys Compd.* **2016**, *684*, 733−738.

(14) Zhang, L.; Reddy, M. A.; Gao, P.; Diemant, T.; Jürgen Behm, R.; Fichtner, M. Study of All Solid-State Rechargeable Fluoride Ion Batteries Based on Thin-Film Electrolyte. *J. Solid State Electrochem.* **2017**, *21*, 1243−1251.

(15) Puin, W.; Rodewald, S.; Ramlau, R.; Heitjans, P.; Maier, J. Local and Overall Ionic Conductivity in Nanocrystalline CaF_2. *Solid State Ionics* **2000**, *131*, 159−164.

(16) Chable, J.; Dieudonne, B.; Body, M.; Legein, C.; Crosnier-Lopez, M.-P.; Galven, C.; Mauvy, F.; Durand, E.; Fourcade, S.; Sheptyakov, D.; Leblanc, M.; Maisonneuve, V.; Demourgues, A. Fluoride Solid Electrolytes: Investigation of the Tysonite-Type Solid Solutions $La_{1-x}Ba_xF_{3-x}$ ($x < 0.15$). *Dalton Trans.* **2015**, *44*, 19625−19635.

(17) Rongeat, C.; Anji Reddy, M.; Witter, R.; Fichtner, M. Solid Electrolytes for Fluoride Ion Batteries: Ionic Conductivity in Polycrystalline Tysonite-Type Fluorides. *ACS Appl. Mater. Interfaces* **2014**, *6*, 2103−2110.

(18) Düvel, A.; Bednarcik, J.; Šepelák, V.; Heitjans, P. Mechanosynthesis of the Fast Fluoride Ion Conductor $Ba_{1-x}La_xF_{2+x}$: From the Fluorite to the Tysonite Structure. *J. Phys. Chem. C* **2014**, *118*, 7117−7129.

(19) Wang, F.; Grey, C. P. Probing the Defect Structure of Anion-Excess $Ca_{1-x}Y_xF_{2+x}$ ($x = 0.03−0.32$) with High-Resolution ^{19}F Magic-Angle Spinning Nuclear Magnetic Spectroscopy. *Chem. Mater.* **1998**, *10*, 3081−3091.

(20) Maier, J. Ionic Conduction in Space Charge Regions. *Prog. Solid State Chem.* **1995**, *23*, 171−263.

(21) Wilkening, M.; Duvel, A.; Preishuber-Pflugl, F.; da Silva, K.; Breuer, S.; Sepelak, V.; Heitjans, P. Structure and Ion Dynamics of Mechano Synthesized Oxides and Fluorides. *Z. Kristallogr. - Cryst. Mater.* **2017**, *232*, 107−127.

(22) Maier, J. Ionic Conduction in Space Charge Regions. *Prog. Solid State Chem.* **1995**, *23*, 171−263.

(23) Wilkening, M.; Duvel, A.; Preishuber-Pflugl, F.; da Silva, K.; Breuer, S.; Sepelak, V.; Heitjans, P. Structure and Ion Dynamics of Mechano Synthesized Oxides and Fluorides. *Z. Kristallogr. - Cryst. Mater.* **2017**, *232*, 107−127.

(24) Saito, Y.; Maier, J. Ionic Conductivity Enhancement of the Fluoride Conductor CaF2 by Grain Boundary Activation Using Lewis Acids. *J. Electrochem. Soc.* **1995**, *142*, 3078−3083.

(25) Ivanov-Shits, A.; Murin, I. Solid State Ionics; Saint-Petersburg State University: Saint-Petersburg, 2010; Vol. *2*.

(26) Ahmad, M. M.; Yamane, Y.; Yamada, K. Structure, Ionic Conduction, And Giant Dielectric Properties of Mechanochemically Synthesized $BaSnF_4$. *J. Appl. Phys.* **2009**, *106*, No. 074106.

(27) Düvel, A.; Ruprecht, B.; Heitjans, P.; Wilkening, M. Mixed Alkaline-Earth Effect in the Metastable Anion Conductor $Ba_{1-x}Ca_xF_2$ ($0 \leq x \leq 1$): Correlating Long-Range Ion Transport with Local Structures Revealed by Ultrafast ^{19}F MAS NMR. *J. Phys. Chem. C* **2011**, *115*, 23784−23789.

(28) Chaudhuri, S.; Wang, F.; Grey, C. P. Resolving the Different Dynamics of the Fluorine Sublattices in the Anionic Conductor $BaSnF_4$ by Using High-Resolution MAS NMR Techniques. *J. Am. Chem. Soc.* **2002**, *124*, 11746−11757.

(29) Preishuber-Pflügl, F.; Epp, V.; Nakhal, S.; Lerch, M.; Wilkening, M. Defect-Enhanced F^- Ion Conductivity in Layer-Structured Nanocrystalline $BaSnF_4$ Prepared by High-Energy Ball Milling Combined with Soft Annealing. *Phys. Status Solidi C* **2015**, *12*, 10−14.

(30) Sorokin, N. SnF_2-Based Solid Electrolytes. *Inorg. Mater.* **2004**, *40*, 989−997.

(31) Le Bail, A. Whole Powder Pattern Decomposition Methods and Applications: A Retrospection. *Powder Diffr.* **2005**, *20*, 316−326.

(32) Thompson, P.; Cox, D. E.; Hastings, J. B. Rietveld Refinement of Debye-Scherrer Synchrotron X-ray Data from Al_2O_3. *J. Appl. Crystallogr.* **1987**, *20*, 79−83.

(33) Langford, J. A Rapid Method for Analysing the Breadths of Diffraction and Spectral Lines Using the Voigt Function. *J. Appl. Crystallogr.* **1978**, *11*, 10−14.

(34) Shannon, R. Revised Effective Ionic Radii and Systematic Studies of Interatomic Distances in Halides and Chalcogenides. *Acta Crystallogr., Sect. A: Cryst. Phys., Diffr., Theor. Gen. Crystallogr.* **1976**, *32*, 751−767.

(35) Laval, J. P.; Frit, B. Defect Structure of Anion-Excess Fluorite-Related $Ca_{1-x}Y_xF_{2+x}$ Solid Solutions. *J. Solid State Chem.* **1983**, *49*, 237−246.

(36) Cheetham, A. K.; Fender, B. E. F.; Steele, D.; Taylor, R. I.; Willis, B. T. M. Defect Structure of Fluorite Compounds Containing Excess Anions. *Solid State Commun.* **1970**, *8*, 171−173.

(37) Laval, J. P.; Mikou, A.; Frit, B.; Roult, G. Short-Range Order in Heavily Doped CaF_2:Ln^{3+} Fluorites: A Powder Neutron Diffraction Study. *Solid State Ionics* **1988**, *28−30*, 1300−1304.

(38) Réau, J.; Matar, S.; Villeneuve, G.; Soubeyroux, J. Conduction Mechanisms in Fluorides and Oxide Fluorides with the Fluorite Structure: Ionic Conductivity, N.M.R. and Neutron Diffraction. *Solid State Ionics* **1983**, *9−10*, 563−570.

(39) Nowak, S.; Berkemeier, F.; Schmitz, G. Ultra-Thin LiPON Films—Fundamental Properties and Application in Solid State Thin Film Model Batteries. *J. Power Sources* **2015**, *275*, 144−150.

(40) Matula, R. A. Electrical Resistivity of Copper, Gold, Palladium, and Silver. *J. Phys. Chem. Ref. Data* **1979**, *8*, 1147−1298.

(41) Meier, W.; Apblett, C.; Ingersoll, D.; McDaniel, A.; Ihlefeld, J. F. Preparation and Processing Temperature Effects on Ion Conductivity in Solution Derived Sodium Zirconium Phosphate ($NaZr_2P_3O_{12}$) Thin Films. *J. Electrochem. Soc.* **2014**, *161*, A364−A367.

(42) Udovic, T. J.; Matsuo, M.; Unemoto, A.; Verdal, N.; Stavila, V.; Skripov, A. V.; Rush, J. J.; Takamura, H.; Orimo, S. Sodium Superionic Conduction in $Na_2B_{12}H_{12}$. *Chem. Commun.* **2014**, *50*, 3750−3752.

(43) Ivanov-Shits, A. K.; Sorokin, N. I.; Fedorov, P. P.; Sobolev, B. P. Specific Features of Ion Transport in Nonstoichiometric Fluorite-Type $Ba_{1-x}R_xF_{2+x}$ (R = La-Lu) Phases. *Solid State Ionics* **1989**, *31*, 269−280.

(44) Irvine, J. T. S.; Sinclair, D. C.; West, A. R. Electroceramics: Characterization by Impedance Spectroscopy. *Adv. Mater.* **1990**, *2*, 132−138.

(45) Voronin, B. M.; Volkov, S. V. Ionic Conductivity of Fluorite-Type Crystals CaF_2, SrF_2, BaF_2, and $SrCl_2$ at High Temperatures. *J. Phys. Chem. Solids* **2001**, *62*, 1349−1358.

(46) Hammad Fawey, M.; Chakravadhanula, V. S. K.; Anji Reddy, M.; Rongeat, C.; Scherer, T.; Hahn, H.; Fichtner, M.; Kübel, C. In situ TEM Studies of Micron-Sized All-Solid-State Fluoride Ion Batteries: Preparation, Prospects and Challenges. *Microsc. Res. Tech.* **2016**, *79*, 615−624.

Publication II

Mohammad, I.; Witter, R.; Fichtner, M.; Anji Reddy, M., Room Temperature Rechargeable Solid-State Fluoride Ion Batteries. *ACS Appl. Energy Mater.* 2018, 1, 4766-4775.

https://pubs.acs.org/doi/pdf/10.1021/acsaem.8b00864

ACS APPLIED ENERGY MATERIALS
Article
Cite This: ACS Appl. Energy Mater. 2018, 1, 4766−4775
www.acsaem.org

Room-Temperature, Rechargeable Solid-State Fluoride-Ion Batteries

Irshad Mohammad,[†,⊥] Raiker Witter,[†,§] Maximilian Fichtner,[⊥,§] and M. Anji Reddy*[,⊥]

[†]Technomedicum, Tallinn University of Technology, Ehitajate tee 5, Tallinn 19086, Estonia
[⊥]Helmholtz Institute Ulm (HIU) for Electrochemical Energy Storage, Helmholtz Strasse 11, Ulm 89081, Germany
[§]Institute of Nanotechnology (INT), Karlsruhe Institute of Technology (KIT), Hermann-von-Helmholtz-Platz 1, Eggenstein-Leopoldshafen 76344, Germany

Supporting Information

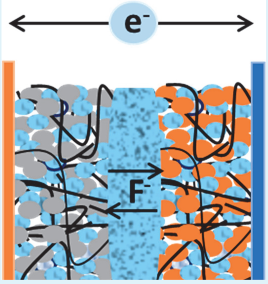

ABSTRACT: Fluoride ion batteries (FIBs) are among interesting electrochemical energy storage systems that are being considered as alternatives to lithium-ion batteries (LIBs). FIB offers high specific energy and energy density, thermal stability, and safety. Despite the advantages posed by the FIBs, several challenges need to be addressed to realize its full potential. We have been working on various aspects related to FIB with the aim of developing sustainable fluoride ion batteries. So far rechargeable FIBs have been demonstrated only at an elevated temperature like 150 °C and above. Here, for the first time, we demonstrate room-temperature (RT) rechargeable fluoride-ion batteries using $BaSnF_4$ as fluoride transporting solid electrolyte. The high ionic conductivity of tetragonal $BaSnF_4$ (3.5×10^{-4} S cm^{-1}) enables the building of RT FIB. We built fluoride ion batteries using Sn and Zn as anodes and BiF_3 as a cathode. We have investigated the electrochemical properties of two different electrochemical cells, $Sn/BaSnF_4/BiF_3$ and $Zn/BiSnF_4/BiF_3$ at various temperatures (25 °C, 60 °C, 100 °C, and 150 °C). The first discharge capacity of the $Sn/BaSnF_4/BiF_3$ and $Zn/BiSnF_4/BiF_3$ cells amounts to 120 mA h g^{-1} and 56 mA h g^{-1} at room temperature, respectively. Although Sn-based cells showed capacity fading, Zn-based cells provided relatively stable cycling behavior at low temperatures. High reversible capacities were observed at elevated operating temperature. EIS, ex-situ XRD, and SEM studies were performed on the cells to investigate the reaction mechanism.

KEYWORDS: *fluoride-ion batteries, $BaSnF_4$, fluoride-ion conductors, Zn anode, Sn anode*

INTRODUCTION

Batteries based on fluoride ion transfer are promising for electrochemical energy storage applications because of their ability to store a large amount of chemical energy.[1] Fluoride (F^-) is a monovalent anion, with low weight and high charge density. The high mobility of F^- in few solid host materials and its large electrochemical stability window make fluoride an attractive charge transporting ion. By combining fluoride transporting electrolyte with suitable metal and metal fluoride electrodes, high voltage electrochemical cells can be built. Further, the monovalent nature of fluoride allows metals to form bivalent or trivalent metal fluorides. Thus, metals can store more than one electron/metal reversibly, and hence, high theoretical capacities can be achieved. Besides high specific energy promises, solid state fluoride ion batteries offer high thermal stability and safety due to nonflammability of fluorides. Indeed, primary electrochemical cells based on fluoride ion transfer were realized long ago,[2−7] and largely overlooked until the demonstration of rechargeable fluoride ion batteries recently.[1] Baukal built FIB using doped-CaF_2 as an electrolyte, Mg as an anode, and NiF_2 or CuF_2 as cathode materials. The cells were operated at high temperatures (400−500 °C).[3] However, no electrochemical data were presented describing the reversibility of the system. Kennedy and Hunter presented a primary FIB cell based on thin film configuration, using PbF_2 as an electrolyte, Pb as an anode, and CuF_2 as a cathode (mixed with PbF_2). The cells were discharged (40% of the theoretical capacity), but charging was not demonstrated.[4] Hagenmuller et al. demonstrated primary FIB cells using β-PbF_2 as a solid electrolyte, Pb as anode and BiF_3 as a cathode.[5] Similar results were reported with $BiO_{0.09}F_{2.82}$ as cathode instead of BiF_3.[6] Later, Potanin demonstrated FIB cells using doped LaF_3 or CeF_3 as an electrolyte, La or Ce as an anode, and doped PbF_2 or BiF_3 as cathode materials. The cells with PbF_2 as cathode delivered 130 mA h g^{-1} and cells with BiF_3 as cathode delivered ~200 mA h g^{-1} between 2.0 and 2.5 V.[7] However, cells were operated at high temperatures (500 °C).

Recently, Reddy and Fichtner for the first time demonstrated rechargeable fluoride ion batteries working at a temperature of 150 °C using solid electrolyte.[1] They have used tysonite-type $La_{0.9}Ba_{0.1}F_{2.9}$ as a solid electrolyte, cerium metal as an anode and various metal fluoride composites as cathode materials. Subsequently, several attempts were made to improve the performance of FIBs: by using nanocrystalline fluorite-type electrolytes,[8] Mg+MgF_2-based composite as an anode,[9] intercalation-based materials as cathodes,[10,11] and by

Received: June 1, 2018
Accepted: August 3, 2018
Published: August 3, 2018

ACS Publications

DOI: 10.1021/acsaem.8b00864
ACS Appl. Energy Mater. 2018, 1, 4766−4775

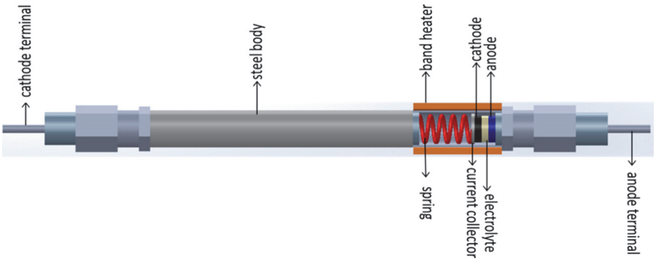

Figure 1. Schematic sketch of the modified Swagelok type cell with band heater.

employing thin electrolyte and electrode layers.[12−14] However, in all cases, the cells were operated at 150 °C or above. Few reports demonstrated the working of fluoride ion batteries at room temperature (RT) employing liquid electrolytes.[15−17] For example, an RT primary fluoride ion battery was demonstrated using a bifluoride-poly(ethylene glycol)-based electrolyte, Mg as an anode, and BiF_3 as a cathode. Although the cells show high first discharge capacity of 250 mA h g^{-1}, charging of the cell was not possible. Recently, rechargeable battery based on fluoride shuttle has been demonstrated using ionic liquid-based electrolyte, PbF_2 formed on Pb plate as anode and Bi needle as the cathode. The cells were charged and discharged reversibly. Nevertheless, there was no clear indication of specific capacities. Further, they reported rapid capacity fading with cycling.[17] Hitherto, there are no reports on rechargeable room temperature solid-state fluoride ion batteries.

The main challenge in the development of RT solid-state FIB lies in the development of fluoride ion transporting solid electrolyte with significant ionic conductivity at RT and with a wide electrochemical stability window (ESW). Rare-earth-based fluorides with tysonite-type structure, for example, $Ce_{0.975}Sr_{0.025}F_{2.975}$ and $Sm_{0.95}Ca_{0.05}F_{2.95}$ show high ionic conductivity in the order of 10^{-4} S cm^{-1} even at RT.[18,19] However, the reported high ionic conductivity in these compounds was achieved only in the form of sintered discs, which is difficult to integrate into full cell configuration, due to the mechanical incompatibility of sintered discs with the ball-milled polycrystalline cathode and anode composites. Interestingly, Sn-based metal fluorides such as $PbSnF_4$ and tetragonal $BaSnF_4$ show high ionic conductivity at RT.[20−25] The ionic conductivity of $PbSnF_4$ and $BaSnF_4$ is in the order of 1×10^{-3} and 1×10^{-4} S cm^{-1} respectively, at 298 K. Despite their high ionic conductivity, these electrolytes have not been tested as solid electrolytes in FIB so far.

Here, we used $BaSnF_4$ as a solid electrolyte to fabricate solid-state FIB. Although $PbSnF_4$ exhibits high ionic conductivity than $BaSnF_4$, we choose to work with $BaSnF_4$ as Pb-free system. $BaSnF_4$ offers high thermal and chemical stabilities in addition to favorable mechanical properties. More importantly, polycrystalline $BaSnF_4$ synthesized via mechanical milling shows ionic conductivity similar to the material synthesized by the high-temperature solid-state method. Therefore, we used mechanochemically synthesized $BaSnF_4$ as a solid electrolyte to demonstrate room temperature solid-state FIBs.

■ EXPERIMENTAL SECTION

Synthesis. Bismuth trifluoride (BiF_3) (anhydrous, 98%), and tin difluoride (SnF_2) (99%) were received from Alfa Aesar. Barium fluoride (BaF_2) (99%), Sn nanopowder (99%) and multiwalled carbon nanotubes (MWCNT) (95%) were received from Sigma-Aldrich. All chemicals were handled in an Ar-filled glovebox to avoid interaction with air. Further, metal fluorides were dried at appropriate temperatures for several hours under vacuum to remove any absorbed moisture. Mechanical milling was used for mixing and synthesis of electrode composites and solid electrolyte, respectively. Mechanical milling was performed using a zirconia vial and balls in an Ar atmosphere by a planetary ball mill (Fritsch P6). The ball to powder ratio was kept the same for each experiment, which was 16:1.

Characterization of Structure and Morphology. X-ray diffraction (XRD) analysis of the electrolyte and electrode composites was performed using STOE STADI-P instrument with Mo−Kα source. Ex-situ XRD was performed using a Bruker D8 Advance diffractometer (Bruker, Karlsruhe, Germany). Ex situ XRD was recorded with Cu Kα radiation (λ = 0.154 nm) in the 2θ range of 20°−60°. Pellets after electrochemical testing were loaded into dome-type sample holders (Bruker AXS Inc.) equipped with a knife edge beam stop for low background and sealed inside an Ar-filled glovebox. Profile matching refinements were done using the Le Bail method and Langford's method with the FullProf software.[26,27] Scanning electron microscopy (SEM) was performed using on ZEISS 1550VP field-emission SEM (Carl Zeiss, Germany). Because of the sufficient electronic conductivity of the electrodes, SEM measurements were performed without a coating of any conductive layer. Similar to ex situ XRD, ex situ SEM measurements were also performed on charged and discharged pellets.

Electrochemical Impedance Spectroscopy (EIS). Electrochemical impedance spectroscopy (EIS) measurements were carried out using a Zahner IM6 electrochemical workstation in the frequency range of 8 MHz to 1 Hz and with a voltage amplitude of 10 mV. In the case of $BaSnF_4$ electrolyte, the spectra were collected at different temperatures starting from RT up to 200 °C. EIS measurements were performed on pellets (∼7 mm diameter and ∼1 mm thick) pressed with 2 tons pressure and sputtered with gold on both sides as an ion blocking electrodes. In the case of FIB cells, impedance spectra were recorded at RT before and after 10 cycles.

Battery Assembly and Testing. Cell fabrication was done in an Ar-filled glovebox. The three-layer pellet for electrochemical testing was fabricated by pressing anode/electrolyte/cathode layers together. The layers were pressed with a pressure of 2 tons, and the pressure was maintained for 1 min using a desktop pressing tool (Specac). The thickness and diameter of the final pellets were approximately 0.8 mm and 7 mm, respectively. The three-layer pressed pellets were then transferred to a modified Swagelok-type cell specially designed and fabricated for working at high temperatures. The cell reported was designed and developed in our research group and we were using the similar cells because the first report on rechargeable FIB.[1] Nevertheless, we have not published any report on cell design. A schematic picture of the high-temperature modified Swagelok-type cell setup with band heater is given in Figure 1. The sketch was created with

DOI: 10.1021/acsaem.8b00864
ACS Appl. Energy Mater. 2018, 1, 4766−4775

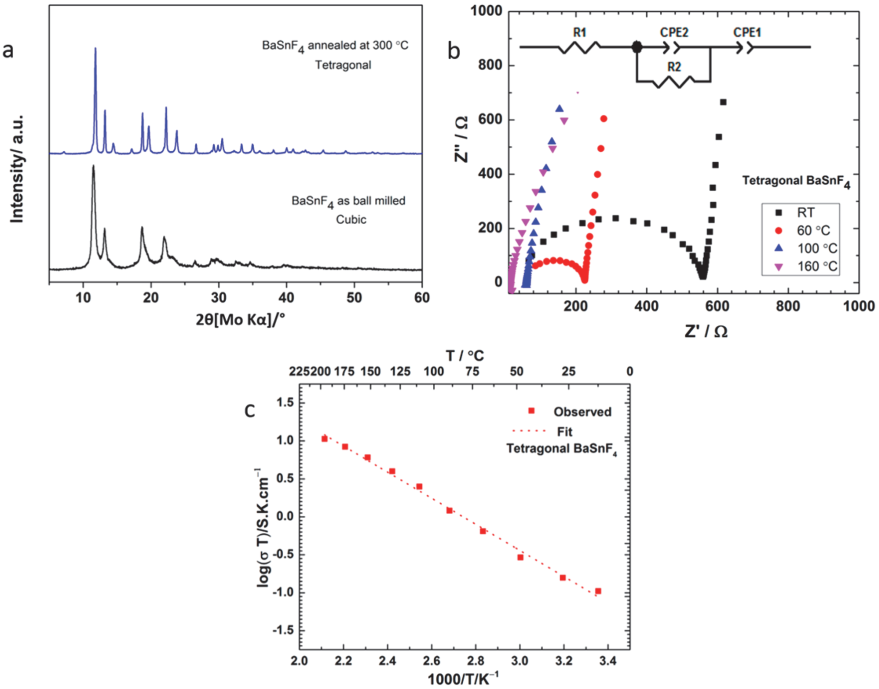

Figure 2. (a) XRD patterns of ball-milled and annealed $BaSnF_4$, (b) Nyquist plot obtained at different temperatures, and (c) Arrhenius plot for the ionic conductivity of tetragonal $BaSnF_4$.

SOLIDWORKS software. Recently, Grenier et al. developed a modified coin cell to investigate the electrochemical properties of FIB at 150 °C.[28] Electrochemical studies on cells were carried out at different temperatures such as 25, 60, 100, and 150 °C. The galvanostatic tests were performed using Arbin battery cycling unit. The cyclic voltammetry experiments were performed using Biologic instruments. Typical mass loading of cathode composite electrode was 5 mg. The cells were cycled at a current density of 10 μA cm^{-2} unless specified. The capacities were calculated referring to the weight of the active material in the cathode composite (BiF_3). The anode amount was used in excess compared to the weight of the cathode.

■ RESULTS AND DISCUSSION

Synthesis, Structure, and Ionic Conductivity of $BaSnF_4$. Tetragonal-$BaSnF_4$ (t-$BaSnF_4$) was synthesized according to an earlier report.[25] In a typical synthesis, stoichiometric amounts of BaF_2 and SnF_2 were milled for 12 h at 600 rpm. The as-milled samples consisted of cubic $BaSnF_4$. To synthesize the tetragonal phase, we annealed the milled sample at 300 °C for 2 h under vacuum. XRD patterns of as-obtained and annealed $BaSnF_4$ are given in Figure 2a. The average crystallite size of as obtained cubic $BaSnF_4$ was 5 nm as calculated by profile matching refinement (Figure S1). After 2 h of annealing, the cubic phase fully transformed to the tetragonal phase (Figure 2a, top layer). Annealing also led to a considerable narrowing of the XRD peaks because of grain growth. The average crystallite size increased from 5 to 25 nm after annealing (Figure S2).

The ionic conductivity of t-$BaSnF_4$ was determined from EIS measurements. EIS spectra were recorded at different temperatures varying from 25 to 200 °C. Figure 2b shows the Nyquist plot of t-$BaSnF_4$, together with the equivalent circuit (Figure 2b, inset). EIS spectra were characterized by a depressed semicircle at a higher frequency and a tilted straight line at low frequency. Total resistance was determined by fitting the Nyquist plot with an equivalent circuit. The equivalent circuit consists of a parallel combination of total resistance (R1) and a constant phase element (CPE1) arising from bulk and grain boundaries, and series combination with another constant phase element (CPE2) appear from blocking electrodes. The calculated ionic conductivity of t-$BaSnF_4$ was 3.5×10^{-4} S cm^{-1} at RT which is consistent with the reported value.[25] The activation energy (E_a) was found to be 0.34 eV for t-$BaSnF_4$ determined by fitting of Arrhenius plot with a straight line (Figure 2c), which matches with the reported value.[25] The ionic conductivity value is sufficient to build RT fluoride ion batteries.

Synthesis and Characterization of Electrode Composites. BiF_3 was chosen as cathode material as it exhibits high ionic conductivity for fluoride at RT.[29] Also, BiF_3 showed good reversibility in solid-state FIBs.[1,30] On the other hand, Sn and Zn were chosen as anode materials due to their predicted electrochemical stability against $BaSnF_4$ solid electrolyte (Table S1). Furthermore, SnF_2, the discharge product of Sn in FIB, is a good fluoride-ion conductor.[20] The use of highly electropositive metals (Mg, Ca, etc.) as anode materials is limited by the low electrochemical stability window of the electrolyte, which may chemically react with $BaSnF_4$ and form Sn metal at the interface.

The cathode composite was prepared by mechanically mixing BiF_3, MWCNT, and t-$BaSnF_4$ together at a weight ratio of 40:10:50. To prepare anode composites, stoichiometric amounts of Sn or Zn powder and MWCNT was first ball milled for 6 h at 300 rpm. In the second step, t-$BaSnF_4$ was added to this composite and milled it further to synthesize final electrode composite. The second milling step was performed at 100 rpm, to preserve the t-$BaSnF_4$ phase. Milling at higher RPM leads to the reconversion of t-$BaSnF_4$ to cubic $BaSnF_4$ in the electrode composites. The final weight ratio of Sn or Zn:$BaSnF_4$:MWCNT composite was 50:40:10. Figure 3 shows the XRD patterns of the composite electrode materials. All the composites show the presence of t-$BaSnF_4$ electrolyte in addition to the contained active material. No other, additional, peaks were observed in the XRD of the composite electrodes, indicating no intermediate crystalline phases formed between the solid electrolyte and active materials during mechanical milling.

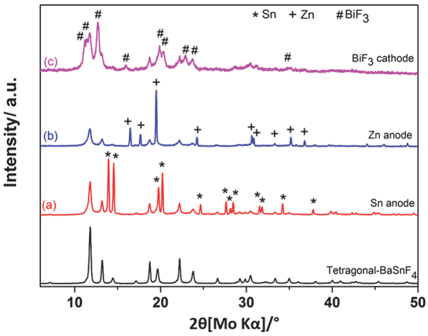

Figure 3. XRD patterns of $BaSnF_4$ and electrode composites: (a) Sn composite, (b) Zn composite, and (c) BiF_3 composite.

Figure 4a−c show the SEM images of BiF_3, Sn, and Zn composites, respectively. The SEM images show a homogeneous distribution of active material, solid electrolyte, and CNT. In the case of BiF_3 composite, the average length of CNT was relatively long compared to the CNT in Sn and Zn composites; this could due to the higher milling speed used to synthesize the Sn and Zn composites, which results in breaking of CNTs. In the case of Sn composite bigger particles of Sn are present (highlighted with squares). EDX mapping analysis was performed on Sn and Zn composites to monitor the distribution of active material, electrolyte, and CNT (Figures S3 and S4). The elements F, Ba, and Sn were found homogeneously distributed in the composite. Sn was present all over the composite as it was also contained in the electrolyte. Since $BaSnF_4$ was used as an electrolyte within the cell pellet the elements, F and Ba were widely spread (Figure S3). The uniform distribution of Zn surrounded by solid electrolyte can be seen in the composite (Figure S4). Figure 4a shows the cross-sectional SEM image of the typical three-layer pellet used in the study. Typical thickness of the cathode, anode, and electrolyte was 25, 85, 650 μm, with a total thickness of around 770 μm.

Electrochemical Studies. Figure 5a depicts cyclic voltammograms (CVs) of the Sn/$BaSnF_4$/BiF_3 cell scanned in the potential range of 0.05 to 1.2 V at 25 °C. During the first scan, a cathodic peak appeared at 0.1 V which corresponds to the reduction of BiF_3 to Bi metal, while in the forward scan, a broad anodic peak at 0.58 V was observed that corresponds to the oxidation of Bi metal to BiF_3. In subsequent cycles, both anodic and cathodic currents were gradually decreased, and their potentials shifted in the positive direction. The gradual decrease of peak current could be due to a lowered fraction of active material involved in the reduction and oxidation reactions. Nevertheless, the reversible oxidation and reduction indicate that bismuth fluoride reversibly reduced and oxidized in Sn/$BaSnF_4$/BiF_3 cell. Figure 5b−f shows the galvanostatic discharge−charge curves and cyclic performance of Sn/$BaSnF_4$/BiF_3 cells operated at temperatures of 25, 60, 100,

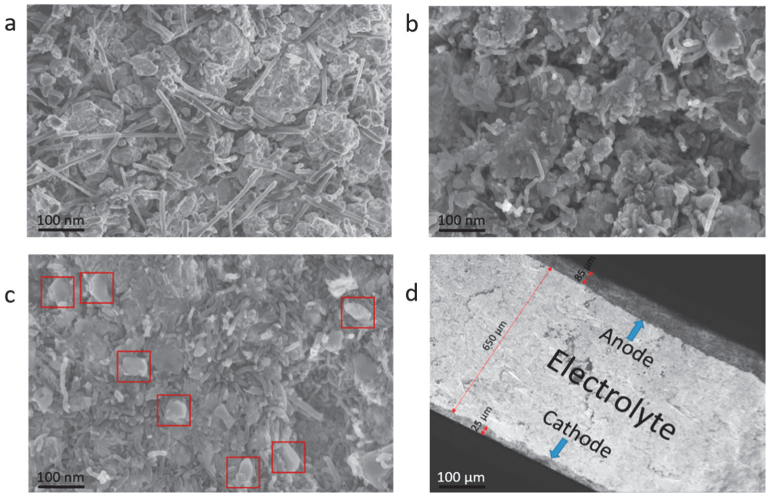

Figure 4. SEM images of (a) BiF_3 composite, (b) Zn composite, (c) Sn composite, and (d) cross-sectional view of a battery pellet.

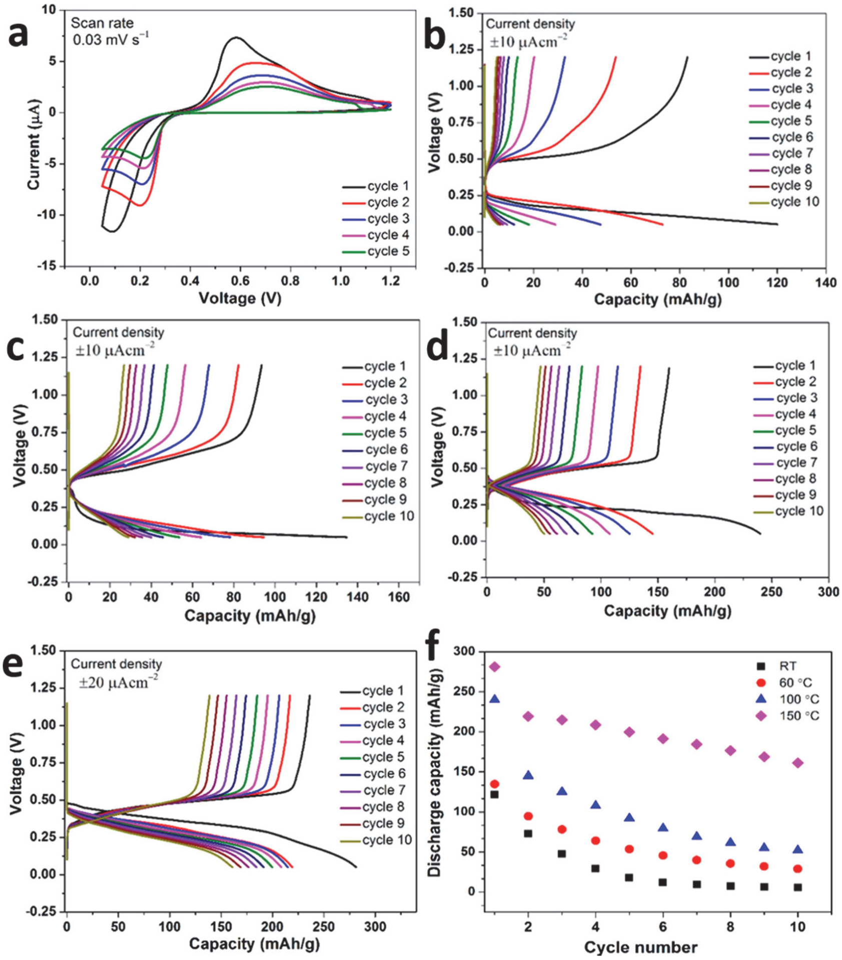

Figure 5. Electrochemical studies on Sn/BaSnF$_4$/BiF$_3$ cell. (a) Cyclic voltammogram obtained at a scan rate of 0.030 mV s^{-1} at 25 °C. First ten galvanostatic discharge−charge curves obtained at (b) 25, (c) 60, (d) 100, and (e) 150 °C. (f) Cycling performance of corresponding cells.

and 150 °C. The cell cycled at RT (Figure 5b) delivered a first discharge capacity of 120 mA h g^{-1} at a current density of 10 μA cm^{-2}. This value is 40% of the theoretical specific capacity of BiF$_3$ (302 mA h g^{-1}) and suggests incomplete conversion of BiF$_3$ to Bi. The first charge capacity amounts to 80 mA h g^{-1}, which corresponds to 66% of initial discharge capacity (120 mA h g^{-1}). In the following discharge/charge cycles capacity faded rapidly, after 4 cycles the discharge capacity reached 30 mA h g^{-1}. The capacity fading with cycling in solid state FIB is known.[1,30] It can be attributed to the volume changes in the electrode materials and an increase of the electrode−electrolyte interfacial resistance. Despite the capacity fading with cycling, the operation of a room-temperature solid-state rechargeable fluoride battery using BaSnF$_4$ electrolyte could be demonstrated.

To investigate the Sn/BaSnF$_4$/BiF$_3$ system in more detail, we have cycled the cells at elevated temperatures. Figure 5c, d show the discharge−charge curves of the cells cycled at 60 and 100 °C, at a current density of 10 μA cm^{-2}. The first discharge capacities of the cells operated at 60 and 100 °C amounted to 134 and 240 mA h g^{-1} which is 44 and 80% of the theoretical specific capacity of BiF$_3$, respectively. The first charge capacities were 94 mA h g^{-1} (60 °C) and 160 mA h g^{-1} (100 °C). After ten cycles the reversible capacities reduced to 26 mA h g^{-1} (60 °C) and 47 mA h g^{-1} (100 °C). To increase the rate of cycling the current density of the cell operated at 150 °C was raised to 20 μA cm^{-2} from 10 μA cm^{-2}. The first discharge capacity of the cell cycled at 150 °C, was 281 mA h g^{-1}, which is 93% of theoretical specific capacity (302 mA h g^{-1}), indicating almost complete conversion of BiF$_3$ to Bi. The first charge capacity of 231 mA h g^{-1} was obtained which is 82% of first discharge capacity. Similar to the cells operated at lower temperatures capacity fading was observed with cycling. However, the extent of capacity fading was less. After ten

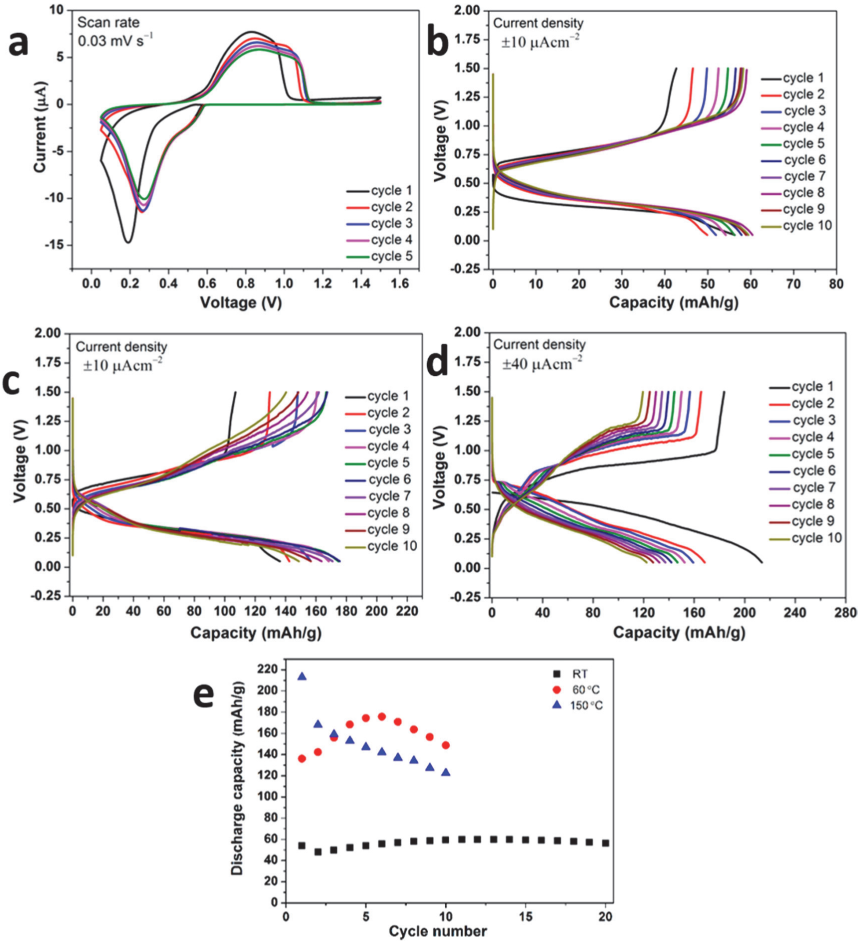

Figure 6. Electrochemical studies on Zn/$BaSnF_4$/BiF_3 cells. (a) Cyclic voltammogram obtained at a scan rate of 0.030 mV s^{-1}. First ten galvanostatic discharge−charge curves obtained at (b) 25, (c) 60, and (d) 150 °C. (e) Cycling performance of corresponding cells.

cycles a reversible capacity of 138 mA h g^{-1} was obtained. The cell operated at 150 °C showed better electrochemical performance compared to the cells operated at 25, 60, and 100 °C. Figure 5f shows the cycling behavior of the cells cycled at various temperatures. It can be observed that the first discharge capacity gradually increased, and the extent of capacity fading decreased with the increase in operating temperature. Although the volume changes in the electrode materials are same at all temperatures, the high capacity and improvement in capacity retention could be attributed to a decrease of resistance of the electrode−electrolyte interface with increasing temperature. Another possible reason is the increase in fluoride ion conductivity in the whole battery with increasing temperature.

The CV of Zn/$BaSnF_4$/BiF_3 cell operated at 25 °C is shown in the Figure 6a. The first cathodic and anodic peaks were observed at 0.19 and 0.82 V, respectively. The cathodic peak is due to the reduction of BiF_3 to Bi while the anodic peak corresponds to the oxidation of Bi to BiF_3. Upon reversible sweeping, the current associated with cathodic and anodic peaks decayed gradually, but to very less extent, which contrasts with the Sn/$BaSnF_4$/BiF_3 cell. Further, the cathodic and anodic peak potentials of Zn/$BaSnF_4$/BiF_3 system are observed at slightly higher voltage compared to Sn/$BaSnF_4$/BiF_3 system, which is due to the slightly higher electromotive force for the BiF_3−Zn system. Figure 6b−e shows galvanostatic discharge/charge curves and cyclic performance of Zn/$BaSnF_4$/BiF_3 cells operated at various temperatures. The first discharge and charge capacity of the cell operated at RT was 56 and 43 mA h g^{-1}, respectively (Figure 6a). On subsequent cycling, the discharge and charge capacities were found to increase slightly. This behavior is in contrast to the cells containing Sn as an anode, where capacity fading was observed during cycling. Also, the first discharge capacity of Zn cell was 56 mA h g^{-1} compared to 120 mA h g^{-1} of Sn cell. This could be due to oxidation of few Zn particles in the first cycle, which

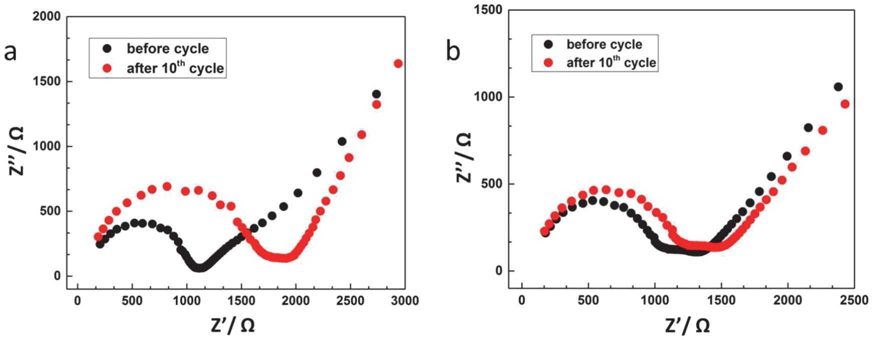

Figure 7. Nyquist plots of the cells recorded at 25 °C (a) for Sn/$BaSnF_4$/BiF_3 cell and (b) Zn/$BaSnF_4$/BiF_3 cell.

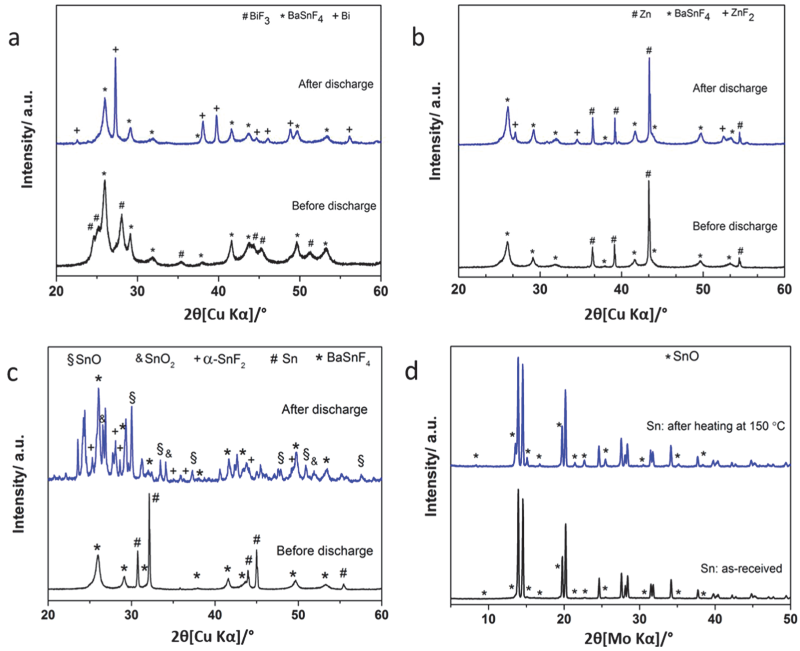

Figure 8. Before and after discharge XRD patterns of (a) BiF_3 composite, (b) Zn composite, and (c) Sn composite; (d) XRD patterns of as-received Sn and after heating it at 150 °C for 2 days in an Ar atmosphere.

were getting activated in the following cycles. The gradual increase of capacity with cycling was observed until 13th cycle at which a reversible capacity of 60 mA h g^{-1} reached. The cells showed very stable cycling. When the cell is operated at 60 °C, the first discharge and charge capacity raised to 136 and 107 mA h g^{-1}, respectively (Figure 6c). Similar to the RT cell, the charge and discharge capacities increased during initial cycling and decreased gradually with further cycling. After ten cycles, a reversible capacity of 140 mA h g^{-1} was obtained. To increase the rate of cycling, in the case of the cell operated at 150 °C, the current density was increased from 10 μA cm^{-2} to 40 μA cm^{-2}, which is four times higher compared to the cells operated at 25 and 60 °C. Despite the comparably high current density, high first discharge and charge capacities of 213 and 183 mA h g^{-1} were obtained, respectively. In contrast to the cells operated at 25 and 60 °C, no increment in capacity was observed during cycling at 150 °C. In this case, capacity faded with cycling. High temperature (150 °C) obviously led to the activation of Zn particles with no further increment in capacity over cycling. The cycling behavior of the cells operated at various temperatures is shown in Figure 6e. Again, significant improvement in capacity was observed when the cells were cycled at elevated temperatures. This could be due to an increase of ionic conductivity of whole battery components at higher temperatures. Further, the cycling performance of the Zn/$BaSnF_4$/BiF_3 cells is better at 25 and 60 °C compared to

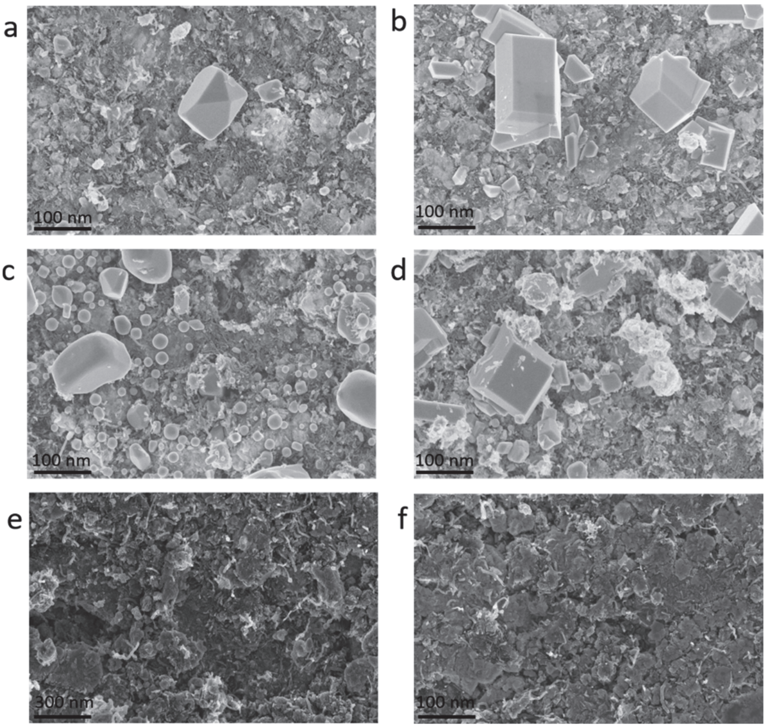

Figure 9. SEM images of Sn anodes: (a) pristine state, (b) after first discharge, (c) after the first charge, (d) after second discharge. SEM images of Zn anode: (e) pristine state and (f) after discharge.

$Sn/BaSnF_4/BiF_3$ cells. However, both cells performed similarly at 150 °C.

Ex Situ Analysis of $Sn/BaSnF_4/BiF_3$ and $Zn/BaSnF_4/BiF_3$ Cells. Although the initial discharge capacity of $Sn/BaSnF_4/BiF_3$ system was higher than that of $Zn/BaSnF_4/BiF_3$ system for each operational temperature, the capacity fading was much higher in the former case (except for the cells operated at 150 °C). To investigate the reasons for capacity fading, EIS measurements were performed on $Sn/BaSnF_4/BiF_3$ and $Zn/BaSnF_4/BiF_3$ cells before and after cycling at RT. Figure 7 shows the EIS spectra (Nyquist plot) of Sn and Zn cells recorded before and after ten cycles. The EIS spectra consist of a depressed semicircle and a tilted straight line at high and low-frequency regions, respectively. The semicircle can be attributed to electrode−electrolyte interface resistance, and the straight line represents the Warburg impedance. Interestingly, the resistance of the Sn and Zn containing cells is the same before the cycling. After ten discharge−charge cycles at RT, the resistance of the cell containing Sn anode is almost doubled, whereas the resistance of the cell containing Zn anode increased marginally. The increase in resistance of the Sn-containing cells might be the reason for the rapid capacity fading in Sn cells. During cycling of the cells, Sn will be converted to SnF_2 or Zn will be converted to ZnF_2. In both cases, severe volume changes are expected (+101% for Sn to SnF_2 and +127% for Zn to ZnF_2) (Table S1). The volume changes in the electrode material may result in the delamination of the electrode−electrolyte layer and electronic and ionic isolation of active material within the electrode composite. Both factors would result in the increase of cell impedance after cycling. Despite higher volume changes predicted for Zn/ZnF_2 couple compared to Sn/SnF_2 couple, Zn containing cells showed less resistance after cycling. Beyond volume changes, it appears that the crystallite size of the active material might play a role in determining the interfacial resistance of Sn-based cells.

To investigate the reaction mechanism, we recorded XRD patterns ex situ on three-layer pellets before and after discharge. For collecting the XRD patterns, $Zn/BaSnF_4/BiF_3$ and $Sn/BaSnF_4/BiF_3$ cells discharged at 150 °C were prepared, where almost complete conversion of BiF_3 to Bi was observed. Figure 8a shows XRD pattern of BiF_3 composite cathode before and after discharge. Before discharge, peaks corresponding to BiF_3 and t-$BaSnF_4$ were observed. After discharge to 0.05 V, BiF_3 peaks disappeared completely, demonstrating complete conversion at the cathode. In the XRD pattern, new peaks appeared which can be indexed to Bi metal which confirms the reduction of BiF_3 to Bi after discharge. The XRD pattern of Zn containing anode composite is shown in Figure 8b. Before discharge, diffraction peaks for Zn and t-$BaSnF_4$ electrolyte were observed. After discharge, few new reflections were observed (marked with +), which were assigned to ZnF_2 resulting from the oxidation of Zn metal after discharge. Diffraction peaks corresponding to Zn can be seen even after discharging because of the excess amount of anode material used.

The XRD patterns of Sn anodes before and after discharge are shown in Figure 8c. Before discharge XRD pattern shows the diffraction peaks of Sn and t-$BaSnF_4$. After discharge, reflections corresponding to α-SnF_2 phase (marked with +) were identified. SnF_2 exists in three polymorphs: monoclinic α-SnF_2 ($C2/c$), orthorhombic β-SnF_2 ($P2_12_12_1$) and tetragonal γ-SnF_2 ($P4_12_12$ or $P4_32_12$).[31] α-SnF_2 is the most stable phase at RT. α to γ phase transition occurs between 125 °C−190 °C. Cooling of γ-SnF_2 leads to the formation of β-phase (at 67 °C). Both γ-SnF_2 and β-SnF_2 are metastable below 110 °C.[32] The observation of α-SnF_2 in the discharged electrode is rational considering the metastability of γ-SnF_2 and β-SnF_2 below 110 °C. Although cells were operated at 150 °C, where γ-SnF_2 is expected to be stable, γ-SnF_2 might have converted to α-SnF_2 after cooling the cell to RT. Several other peaks were observed in addition to the peaks of α-SnF_2 and t-$BaSnF_4$ phases. Some of these peaks could be indexed to SnO and SnO_2. Presence of tin oxide impurities in the discharged electrode puzzled us initially as there were no impurities found in the milled electrode composite of Sn. The surface of the as-received Sn might have oxide impurities on the surface which might have been removed after mechanical milling at 300 rpm. To validate this hypothesis, we took the XRD of as-received Sn and after heating the Sn at 150 °C to reproduce the conditions that are present in the cell. Figure 8d shows the XRD patterns of as received Sn and after heating it at 150 °C for 2 days in an Ar atmosphere. The XRD patterns show the presence of minor impurities tin oxide (SnO). The intensity of the oxide peaks grew considerably after heating at 150 °C in an Ar atmosphere. These results suggest that as-received Sn sample contains tin oxide impurities mainly as an amorphous phase on the surface, which are unnoticeable in the ball milled composite but well crystallized during the heating process or the discharge of the cell at 150 °C. In addition to SnO impurity, we also observed SnO_2 in the XRD pattern of the discharged electrode (Figure 8c), which was not seen in the XRD pattern of the heated sample (Figure 8d). SnO_2 might have formed by the partial disproportion of SnO to Sn and SnO_2, during the discharge process.

To track the morphological changes, ex-situ SEM measurements were performed on the electrode composites before and after discharge. Sn/$BaSnF_4$/BiF_3 and Zn/$BaSnF_4$/BiF_3 cells discharged and charged at 150 °C were used for SEM measurements. Figure 9a−d shows the SEM images of the Sn side of the pellet (Sn/$BaSnF_4$/BiF_3): before discharge (Figure 9a), after discharge (Figure 9b), after first charge (Figure 9c) and after second discharge (Figure 9d). The pristine Sn composite contains pyramid-shaped crystals (Figure 9a). After first discharge, tetragonal-shaped particles were observed on the surface that could be due to the formation of SnF_2 (Figure 9b), which was evidenced in the ex situ XRD of Sn electrode after discharge (Figure 8c). After the first charge, more spherical particles were observed. After second discharge the tetragonal shaped particles reappeared, which confirms morphological changes at Sn electrode. From ex situ SEM images, it is clear that during cycling more of the bigger particles are present. The melting point of SnF_2 and Sn is 225 and 231.9 °C, respectively, which could have resulted in particle growth during cycling at 150 °C. SEM images of Zn anodes before and after discharge are shown in Figure 9e, f. In contrast to Sn electrode, Zn particles were not visible even in the pristine state of the Zn electrode. Further, we did not observe the formation of Zn dendrites, which is well-known in Zn−air batteries.[33] After discharge, very similar morphology was observed in comparison to the pristine state. This indicates that Zn and the oxidized ZnF_2 particles are not as large as in the case of Sn-SnF_2. This may explain the high reversibility found in the BiF_3−Zn system compared to the BiF_3−Sn system.

■ CONCLUSION

Tetragonal $BaSnF_4$ shows promising features as fluoride ion transporting solid electrolyte at 25 °C and enables the building of RT fluoride ion batteries, which was demonstrated for the first time. The cells can be operated at various temperatures ranging from 25 to 150 °C. We have discussed here two types of new FIB systems with Zn and Sn anode, while BiF_3 was used as the cathode. At RT, Sn/BiF_3 system exhibits a high first discharge capacity of 120 mA h g^{-1}, however with rapid fading upon cycling. On the other hand, the Zn/BiF_3 cell displays less first discharge capacity but stable cycling performance at RT. After 20 cycles the discharge capacity reached about 61 mA h g^{-1}. The rapid capacity fading in the case of Sn containing anode might be due to the increase of cell resistance during cycling and large particle size of Sn. Although we could demonstrate the feasibility of RT FIB here, the cells delivered low average voltage due to the low voltage redox couples (Sn/BiF_3 and Zn/BiF_3), resulting in a low energy density of the battery. One way to increase the voltage would be to use the high voltage insertion cathode materials such as $LaSrMnO_4F_2$ and related oxyfluorides. The use of highly electropositive metals (Mg, Ca, etc.) as anode materials is limited by the low electrochemical stability window of the electrolyte, which may react with $BaSnF_4$ and form Sn metal at the interface. Future work will be focused mainly on the search of appropriate anode and cathode combinations that can provide high specific energy and durability.

■ ASSOCIATED CONTENT

Ⓢ Supporting Information

The Supporting Information is available free of charge on the ACS Publications website at DOI: 10.1021/acsaem.8b00864.

Observed and calculated XRD patterns of as ball-milled and annealed $BaSnF_4$, EDX elemental mapping of Sn and Zn composites, table with calculated voltage values and volume changes (PDF)

■ AUTHOR INFORMATION

Corresponding Author

*E-mail: munnangi.reddy@kit.edu.

ORCID

Raiker Witter: 0000-0002-7085-2490
M. Anji Reddy: 0000-0001-9101-0252

Notes

The authors declare no competing financial interest.

■ ACKNOWLEDGMENTS

Financial support by the European Union through the European Regional Development Fund (Dora Plus Action 1) and Estonian Ministry of Education and Research through Grants PUT1534. The authors gratefully thank Mr. Tobias Braun, Helmholtz Institute Ulm, for assisting in the SEM measurements. R.W. gratefully acknowledges Tallinn University of Technology and Karlsruhe Institute of Technology. This work contributes to the research performed at CELEST (Center for Electrochemical Energy Storage Ulm-Karlsruhe).

REFERENCES

(1) Anji Reddy, M.; Fichtner, M. Batteries Based on Fluoride Shuttle. *J. Mater. Chem.* **2011**, *21* (43), 17059−17062.

(2) Baukal, W., Solid-electrolyte cell. *Ger. Offen.* 1971, DE2017128.

(3) Baukal, W.; Knodler, R.; Kuhn, W. Overview of the Applications of Solid Electrolytes. *Chem. Ing. Tech.* **1978**, *50*, 245−249.

(4) Kennedy, J. H.; Hunter, J. C. Thin Film Galvanic Cell Pb/PbF$_2$/PbF$_2$, CuF$_2$/Cu. *J. Electrochem. Soc.* **1976**, *123*, 10−14.

(5) Hagenmuller, P.; Reau, J. M.; Lucat, C.; Matar, S.; Villeneuve, G. Ionic Conductivity of Fluorite-Type Fluorides. *Solid State Ionics* **1981**, *3−4*, 341−345.

(6) Schoonman, J. A Solid-State Galvanic Cell with Fluoride-Conducting Electrolytes. *J. Electrochem. Soc.* **1976**, *123*, 1772−1775.

(7) Potanin, A. A. Solid State Chemical Current Source Based on Ionic Conductor of the Lanthanum Trifluoride Type. *J. Russ. Chem. Soc.* **2001**, *45*, 58−63.

(8) Rongeat, C.; Reddy, M. A.; Witter, R.; Fichtner, M. Nanostructured Fluorite-Type Fluorides As Electrolytes for Fluoride Ion Batteries. *J. Phys. Chem. C* **2013**, *117*, 4943−4950.

(9) Rongeat, C.; Anji Reddy, M.; Diemant, T.; Behm, R. J.; Fichtner, M. Development of New Anode Composite Materials for Fluoride Ion Batteries. *J. Mater. Chem. A* **2014**, *2*, 20861−20872.

(10) Nowroozi, M. A.; Wissel, K.; Rohrer, J.; Munnangi, A. R.; Clemens, O. LaSrMnO$_4$: Reversible Electrochemical Intercalation of Fluoride Ions in the Context of Fluoride Ion Batteries. *Chem. Mater.* **2017**, *29*, 3441−3453.

(11) Nowroozi, M. A.; Ivlev, S.; Rohrer, J.; Clemens, O. La$_2$CoO$_4$: a New Intercalation Based Cathode Material for Fluoride Ion Batteries with Improved Cycling Stability. *J. Mater. Chem. A* **2018**, *6*, 4658−4669.

(12) Zhang, L.; Anji Reddy, M.; Gao, P.; Fichtner, M. Development of Dense Solid State Thin-Film Electrolyte for Fluoride Ion Batteries. *J. Alloys Compd.* **2016**, *684*, 733−738.

(13) Zhang, L.; Reddy, M. A.; Gao, P.; Diemant, T.; Jürgen Behm, R.; Fichtner, M. Study of All Solid-State Rechargeable Fluoride Ion Batteries Based on Thin-Film Electrolyte. *J. Solid State Electrochem.* **2017**, *21*, 1243−1251.

(14) Zhang, L.; Reddy, M. A.; Fichtner, M. Electrochemical Performance of All Solid-State Fluoride-Ion Batteries Based on Thin-Film Electrolyte Using Alternative Conductive Additives and Anodes. *J. Solid State Electrochem.* **2018**, *22*, 997−1006.

(15) Gschwind, F.; Bastien, J. Parametric Investigation of Room-Temperature Fluoride-Ion Batteries: Assessment of Electrolytes, Mg-Based Anodes, and BiF$_3$-cathodes. *J. Mater. Chem. A* **2015**, 3, 5628−5634.

(16) Darolles, I.; Weiss, C. M.; Alam, M. M.; Tiruvannamalai, A.; Jones, S. C. Fluoride Ion Battery Compositions. U.S. Patent US 20120164541A1, June 28, 2012.

(17) Okazaki, K.-i.; Uchimoto, Y.; Abe, T.; Ogumi, Z. Charge−Discharge Behavior of Bismuth in a Liquid Electrolyte for Rechargeable Batteries Based on a Fluoride Shuttle. *ACS Energy Lett.* **2017**, *2*, 1460−1464.

(18) Dieudonné, B.; Chable, J.; Body, M.; Legein, C.; Durand, E.; Mauvy, F.; Fourcade, S.; Leblanc, M.; Maisonneuve, V.; Demourgues, A. The Key Role of the Composition and Structural Features in Fluoride Ion Conductivity in Tysonite Ce$_{1-x}$Sr$_x$F$_{3-x}$ Solid Solutions. *Dalton Trans.* **2017**, *46*, 3761−3769.

(19) Dieudonné, B.; Chable, J.; Mauvy, F.; Fourcade, S.; Durand, E.; Lebraud, E.; Leblanc, M.; Legein, C.; Body, M.; Maisonneuve, V.; Demourgues, A. Exploring the Sm$_{1-x}$Ca$_x$F$_{3-x}$ Tysonite Solid Solution as a Solid-State Electrolyte: Relationships between Structural Features and F$^-$ Ionic Conductivity. *J. Phys. Chem. C* **2015**, *119*, 25170−25179.

(20) Sorokin, N. SnF$_2$-Based Solid Electrolytes. *Inorg. Mater.* **2004**, *40*, 989−997.

(21) Chadwick, A. V.; Hammam, E. S.; Vanderputten, D.; Strange, J. H. Studies of Ionic Transport in MF$_2$-SnF$_2$ Systems. *Cryst. Lattice Defect. Amorph. Mater.* **1987**, *15*, 303−308.

(22) Ahmad, M. M.; Yamane, Y.; Yamada, K. Structure, Ionic Conduction, And Giant Dielectric Properties of Mechanochemically Synthesized BaSnF$_4$. *J. Appl. Phys.* **2009**, *106*, 074106.

(23) Düvel, A.; Ruprecht, B.; Heitjans, P.; Wilkening, M. Mixed Alkaline-Earth Effect in the Metastable Anion Conductor Ba$_{1-x}$Ca$_x$F$_{2+x}$ ($0 \le x \le 1$): Correlating Long-Range Ion Transport with Local Structures Revealed by Ultrafast ^{19}F MAS NMR. *J. Phys. Chem. C* **2011**, *115*, 23784−23789.

(24) Chaudhuri, S.; Wang, F.; Grey, C. P. Resolving the Different Dynamics of the Fluorine Sublattices in the Anionic Conductor BaSnF$_4$ by Using High-Resolution MAS NMR Techniques. *J. Am. Chem. Soc.* **2002**, *124*, 11746−11757.

(25) Preishuber-Pflügl, F.; Epp, V.; Nakhal, S.; Lerch, M.; Wilkening, M. Defect-Enhanced F$^-$ Ion Conductivity in Layer-Structured Nanocrystalline BaSnF$_4$ Prepared by High-Energy Ball Milling Combined with Soft Annealing. *Phys. Status Solidi (c)* **2015**, *12*, 10−14.

(26) Le Bail, A. Whole Powder Pattern Decomposition Methods and Applications: A retrospection. *Powder Diffr.* **2005**, *20*, 316−326.

(27) Langford, J. A Rapid Method for Analysing the Breadths of Diffraction and Spectral Lines Using the Voigt Function. *J. Appl. Crystallogr.* **1978**, *11*, 10−14.

(28) Grenier, A.; Porras Gutierrez, A. G.; Groult, H.; Dambournet, D. Modified coin cells to evaluate the electrochemical properties of solid-state fluoride-ion batteries at 150 °C. *J. Fluorine Chem.* **2016**, *191*, 23−28.

(29) Shafer, M. W.; Chandrashekhar, G. V.; Figat, R. A. New Fluoride Ion Conductor, K$_x$Bi$_{1-x}$F$_{3-2x}$ ($0.02 \le x \le .12$), with the Tysonite Structure. *Solid State Ionics* **1981**, *5*, 633−635.

(30) Bhatia, H.; Thieu, D. T.; Pohl, A. H.; Chakravadhanula, V. S. K.; Fawey, M. H.; Kübel, C.; Fichtner, M. Conductivity Optimization of Tysonite-type La$_{1-x}$Ba$_x$F$_{3-x}$ Solid Electrolytes for Advanced Fluoride Ion Battery. *ACS Appl. Mater. Interfaces* **2017**, *9*, 23707−23715.

(31) Denes, G.; Pannetier, J.; Lucas, J. About SnF$_2$ Stannous Fluoride. II. Crystal Structure of β- and γ-SnF$_2$. *J. Solid State Chem.* **1980**, *33*, 1−11.

(32) Denes, G. About SnF$_2$ Stannous Fluoride. VI. Phase Transitions. *Mater. Res. Bull.* **1980**, *15*, 807−819.

(33) Wang, K.; Pei, P.; Ma, Z.; Chen, H.; Xu, H.; Chen, D.; Wang, X. Dendrite growth in the recharging process of zinc−air batteries. *J. Mater. Chem. A* **2015**, *3*, 22648−22655.

Publication III

Mohammad, I.; Witter, R.; Fichtner, M.; Anji Reddy, M., Introducing Interlayer Electrolytes: Towards Room Temperature High Potential Solid State Rechargeable Fluoride Ion Batteries. *ACS Appl. Energy Mater.* 2019, 2, 1553-1562.

https://pubs.acs.org/doi/pdf/10.1021/acsaem.8b02166

ACS APPLIED ENERGY MATERIALS
Article
Cite This: ACS Appl. Energy Mater. 2019, 2, 1553−1562
www.acsaem.org

Introducing Interlayer Electrolytes: Toward Room-Temperature High-Potential Solid-State Rechargeable Fluoride Ion Batteries

Irshad Mohammad,[†,⊥] Raiker Witter,[†,§] Maximilian Fichtner,[⊥,§] and M. Anji Reddy[*,⊥]

[†]School of Information Technologies, Tallinn University of Technology, Ehitajate tee 5, 19086 Tallinn, Estonia
[⊥]Helmholtz Institute Ulm (HIU) Electrochemical Energy Storage, Helmholtzstr. 11, 89081 Ulm, Germany
[§]Karlsruhe Institute of Technology (KIT), Institute of Nanotechnology (INT), Hermann-von-Helmholtz-Platz 1, 76344, Eggenstein-Leopoldshafen, Germany

Supporting Information

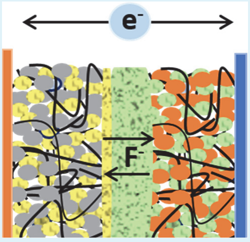

ABSTRACT: Solid-state fluoride ion batteries (FIBs) promise high specific energy, thermal stability, and safety. Research on FIBs is in its infancy, and a number of issues still need to be addressed to realize its full potential. Progress on FIB strongly depends on developing suitable fluoride-ion-transporting electrolytes at room temperature (RT). $BaSnF_4$ shows high ionic conductivity of 3.5×10^{-4} S cm^{-1} at RT. However, it has limited electrochemical stability window. Recently, we demonstrated RT rechargeable FIB utilizing $BaSnF_4$ as a solid electrolyte and low electropositive metals, such as Sn and Zn metals, as anodes because of the limited electrochemical stability of $BaSnF_4$, which results in low operating voltages. However, to enable cells with high operating potentials, the electrolyte should be compatible with highly electropositive metals (e.g., La, Ce). Although tysonite-type $La_{0.9}Ba_{0.1}F_{2.9}$ electrolyte was shown to be compatible with such metals, it has the drawback of low ionic conductivity at RT (0.4×10^{-6} S cm^{-1}). To overcome these limitations of the low electrolyte stability and low ionic conductivity, we applied an interlayer electrolyte to build FIB rather than pure electrolytes. A thin layer of $La_{0.9}Ba_{0.1}F_{2.9}$ was pressed together with a thick layer of $BaSnF_4$. Applying low-conductive $La_{0.9}Ba_{0.1}F_{2.9}$ as thin layer enhanced the total conductance of the pellet (compared to pure $La_{0.9}Ba_{0.1}F_{2.9}$), while it physically isolated the less stable and highly conductive electrolyte ($BaSnF_4$) from the anode. This approach allowed the demonstration of relatively high voltage FIBs at RT, which can otherwise not operate either with $BaSnF_4$ electrolyte alone. We optimized the total ionic conductivity of the interlayer electrolyte by altering the thickness of the $La_{0.9}Ba_{0.1}F_{2.9}$ layer. The total ionic conductivity of interlayer electrolyte was increased to 0.89×10^{-5} S cm^{-1} for 45 μm thick $La_{0.9}Ba_{0.1}F_{2.9}$ at RT, which is more than 1 order of magnitude higher compared to the pure $La_{0.9}Ba_{0.1}F_{2.9}$ (0.4×10^{-6} S cm^{-1}). Finally, we demonstrate the feasibility of operating FIB at RT utilizing the interlayer pellet as an electrolyte, BiF_3 as a cathode and Ce as an anode material. The approach described here would enable the design and development of new solid electrolytes with advanced properties with existing electrolytes.

KEYWORDS: *room-temperature fluoride ion batteries, interlayer electrolyte, fluoride ion conductors, $La_{0.9}Ba_{0.1}F_{2.9}$, $BaSnF_4$, Ce anode, BiF_3 cathode*

INTRODUCTION

Lithium-ion batteries (LIBs) are currently the main power sources of portable electronics and being introduced in the transportation sector to power electric vehicles (EVs) and for grid storage applications. The demand for electrochemical energy storage devices is continuously increasing and, consequently, the demand for alternative electrochemical energy storage (beyond Li-ion) technologies is growing. To this end, several post Li-ion technologies based on Na^+, Mg^{2+}, Al^{3+}, and F^- transport have been revisited and are being pursued actively.[1−4] Batteries based on fluoride transport offer attractive features.[4] The elemental properties of fluoride (high charge density, high electronegativity, and relatively low weight) qualify F^- as a good charge transporting and storing ion. By combining suitable fluoride transporting electrolyte with a metal and metal fluoride, we can build fluoride ion batteries (FIBs) similar to LIBs. Electrochemical cells based on fluoride shuttle have already been reported earlier.[5−10] However, these reports on FIB were focused on primary batteries (not rechargeable). Recently, Reddy and Fichtner demonstrated rechargeable FIBs operable at 150 °C by applying $La_{0.9}Ba_{0.1}F_{2.9}$ as a solid electrolyte, Ce as an anode, and BiF_3 as the cathode material.[4] Since then, several reports were published addressing the various issues related to fluoride ion batteries.[11−28] One of the remaining challenges is the high operating temperature of FIB.

A major roadblock for building RT FIB is the lack of suitable fluoride ion transporting electrolyte. The electrolyte in an electrochemical cell should possess a large electrochemical stability window, in addition to the fast transport of ions

Received: December 13, 2018
Accepted: January 29, 2019
Published: January 29, 2019

DOI: 10.1021/acsaem.8b02166
ACS Appl. Energy Mater. 2019, 2, 1553−1562

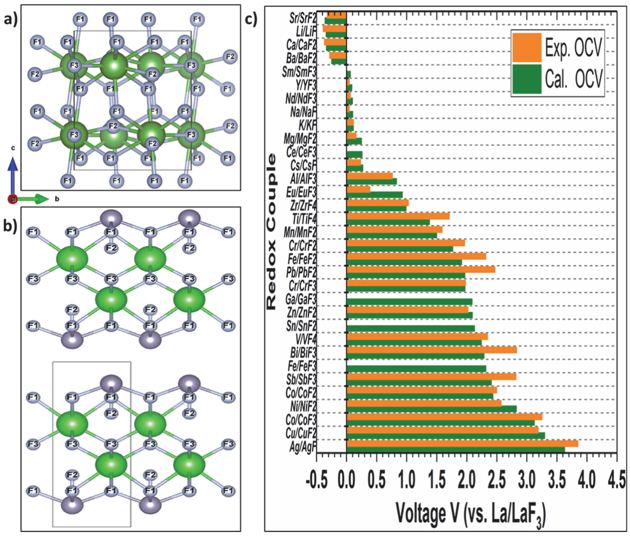

Figure 1. Crystal structure of (a) LaF_3 and (b) $BaSnF_4$. (c) Electromotive force (emf) of various metal/metal fluoride redox couples versus La/LaF_3 reference.

between the electrodes. Also, the electrolyte should be stable against the chemical reactions occurring at anode and cathode materials. In other words, the electrochemical potentials of cathode and anode should fall within the bottom of the conduction band and top of the valence band of a solid electrolyte.[29] Compounds consisting of highly electropositive elements will be useful to achieve a large electrochemical stability window. Indeed, several fluoride-transporting solid electrolytes fulfill the above criteria. Lanthanum trifluoride (LaF_3) is one such electrolyte.

LaF_3 adopts trigonal ($P\bar{3}c1$) tysonite-type structure. The structure of LaF_3 can be described as a layered structure. One layer is built-up of only fluoride ions (F1), and the second layer is built-up of fluoride ions (F2, F3), as well as La ions (Figure 1a). F3 ions are in the same plane as of La, but F2 ions slightly move out of the La−F plane making F2 and F3 crystallographically and dynamically different. These two layers are stacked alternatively perpendicular to the *c*-axis. The ratio of fluoride ions in LaF_3 is F1: F2: F3 = 12:4:2. High-resolution ^{19}F MAS NMR studies confirmed the existence of the three fluoride sites F1: F2: F3 in the LaF_3 structure.[30] The ionic conductivity of undoped LaF_3 single crystals is about 10^{-6} S cm^{-1} at RT, which can be significantly increased by doping with alkaline earth metals.[31,32] For example, the ionic conductivity of $La_{0.95}Ba_{0.05}F_{2.95}$ single crystals turned out to be $\sim 10^{-4}$ S cm^{-1} at RT, which would be adequate for operation of solid-state FIB at RT or slightly elevated temperatures. However, single crystals cannot be integrated into practical all-solid-state batteries. High conductivities that are similar to those reported for single crystals at RT could only be reached for corresponding nanocrystalline material at 150 °C.[33] Consequently, FIBs reported so far were operated at elevated temperatures.[4,12−19,27,28]

Nevertheless, we were recently able to demonstrate the first room-temperature rechargeable solid state fluoride-ion battery.[34] In contrast to LaF_3, compounds like $BaSnF_4$ and $PbSnF_4$ show high ionic conductivity also as pressed powders, however, at the cost of possessing a low electrochemical stability window. The structure of tetragonal $BaSnF_4$ can be derived from the cubic fluorite-type structure by ordering the cations BaBaSnSnBaBa, along (001) direction, again resulting in three different fluoride sites. They reside in the Sn−Sn, Ba−Sn, and Ba−Ba layers and are termed F1, F2, and F3, respectively (Figure 1b). The local environment of F3 ions in the Ba−Ba layers is similar to that of fluoride ions in BaF_2. The presence of a stereoactive lone pair on Sn gives rise to a repulsive interaction between the lone pair and negatively charged fluoride ion and results in the depletion of the fluoride ions in the Sn−Sn and Sn−Ba layers.[35] Further, the lone electron pair on Sn^{2+} strongly influences the fluoride ion sublattice and contributes to the high fluoride ion conductivity in $BaSnF_4$.[35] The ionic conductivity of tetragonal $BaSnF_4$ is 7×10^{-4} S cm^{-1} at RT,[36] which is adequate to operate FIBs at RT. More importantly, polycrystalline $BaSnF_4$ synthesized via mechanical milling shows ionic conductivity close to the single-crystal conductivity, making it applicable in an ASSB concept.[37]

Figure 1c shows the calculated electromotive force (emf) of various metal/metal fluoride redox couples. The details of the calculation were given in Experimental Section. EMF values corresponding to the figure are given in Table S1 (please see Supporting Information). The emf was referenced versus La/LaF_3 redox couple because of its high electrochemical stability and fluoride ion conductivity. If the potential of a particular redox couple is positive with respect to the electrolyte used, then redox reactions are not possible between the electrolyte and the electrode. On the other hand, if the redox potential of the redox couple is more negative than that of the electrolyte, then redox reaction may occur between electrode and electrolyte. The emf of Ce/CeF_3 couple is 0.002 V (exp.) versus La/LaF_3. Therefore, LaF_3 is a suitable electrolyte for Ce anode. In contrast, the emf of Ce/CeF_3 couple is −1.87 V

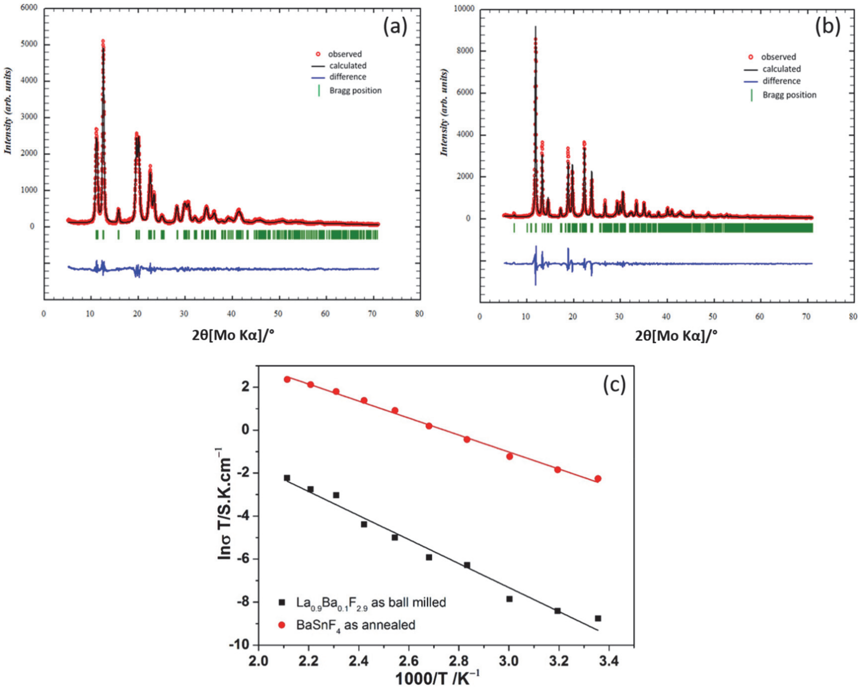

Figure 2. (a) Observed and calculated XRD patterns of (a) $La_{0.9}Ba_{0.1}F_{2.9}$ and (b) tetragonal $BaSnF_4$. (c) Arrhenius plots and fits (line) of the overall ionic conductivities for $La_{0.9}Ba_{0.1}F_{2.9}$ (as ball milled) and $BaSnF_4$ (as annealed) samples.

(cal.) versus Sn/SnF_2. Therefore, $BaSnF_4$ (as it contains SnF_2) not suitable for Ce or other high electropositive (La, Mg, etc.) anodes. The redox voltages can be used as a primary guide to judge the compatibility of electrode and electrolyte materials.

Recently, we demonstrated the RT rechargeable FIB utilizing $BaSnF_4$ as a solid electrolyte.[34] We applied low electropositive metals, such as Sn and Zn, as anode materials to be chemically compatible with $BaSnF_4$. The use of Sn and Zn against BiF_3 cathode resulted in a low operating potential, which led to the low specific energy. To achieve higher specific energies, the voltage of the cells has to be maximized, which can be accomplished by the usage of highly electropositive metals (like Ce, La) as anode materials. The application of high voltage fluoride insertion oxide cathodes materials might be another option;[15,16] however, at the cost of lower specific capacities leading to potentially reduced specific energies. On the other hand, metals like La and Ce are only compatible with electrolytes like $La_{0.9}Ba_{0.1}F_{2.9}$ (composed of highly electropositive elements), but the ionic conductivity of these electrolytes is too low to operate FIB at RT.

To overcome these obstacles of both electrolyte instability and low ionic conductivity, we introduce an interlayer electrolyte concept in fluoride ion batteries to combine the advantages of two ion conductors ($BaSnF_4$ and $La_{0.9}Ba_{0.1}F_{2.9}$). Thus, RT FIBs can be realized with higher voltages. Applying low ion conducting $La_{0.9}Ba_{0.1}F_{2.9}$ electrolyte as a thin layer will not compromise the total conductivity of the pellet much, and at the same time, it physically isolates the less stable and highly conductive electrolyte ($BaSnF_4$) from the anode. The direct contact between $BaSnF_4$ and Ce would lead to the formation CeF_3, BaF_2, and Sn metal at the interface (as the redox potential of Ce/CeF_3 couple is −1.87 V (cal.) vs Sn/SnF_2). Application of a thin layer of $La_{0.9}Ba_{0.1}F_{2.9}$ protects the Ce anode (the redox potential of Ce/CeF_3 couple is 0.002 V (exp.) vs La/LaF_3). This concept allows the demonstration of relatively high voltage FIBs at RT, which will otherwise not operate either with $BaSnF_4$ or $La_{0.9}Ba_{0.1}F_{2.9}$ electrolytes alone. Interlayer electrolytes have been used in lithium-ion and sodium-ion batteries mainly to protect reactive metals or to improve the interfacial resistance.[38−40] Here, we show the total ionic conductivity of the electrolyte can be increased significantly while extending the electrochemical stability window.

■ RESULTS AND DISCUSSION

Ionic Conductivity of $La_{0.9}Ba_{0.1}F_{2.9}$ and $BaSnF_4$. Figure 2a shows the profile matched XRD pattern of $La_{0.9}Ba_{0.1}F_{2.9}$. All the observed peaks can be indexed to the tysonite type LaF_3 structure. No additional peaks were observed, confirming the substitution of BaF_2 in LaF_3. The average crystallite size of $La_{0.9}Ba_{0.1}F_{2.9}$ was 12 nm as calculated by profile matching (Figure 2a). Figure 2b shows the profile matched XRD pattern of tetragonal $BaSnF_4$ (t-$BaSnF_4$). The average crystallite size of the tetragonal $BaSnF_4$ (t-$BaSnF_4$) turned out to be 20 nm according to the profile matching (Figure 2b). Figure 2c shows the Arrhenius plot for the ionic conductivity of $La_{0.9}Ba_{0.1}F_{2.9}$ and $BaSnF_4$ (see Figure S1 for the Nyquist plots of t-$BaSnF_4$). The ionic conductivities of $La_{0.9}Ba_{0.1}F_{2.9}$ and $BaSnF_4$ are 4 ×

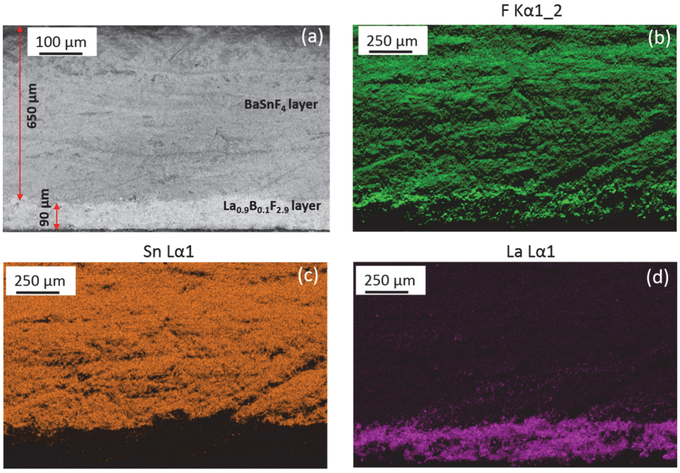

Figure 3. (a) Cross-sectional SEM view of an interlayer electrolyte pellet (20 mg of $La_{0.9}Ba_{0.1}F_{2.9}$) and EDX mapping images (b−d) of F, Sn, and La are shown.

10^{-7} S cm^{-1} and 3.5 × 10^{-4} S cm^{-1} at RT, respectively; these values are similar to reported ones.[33,35] The activation energy (E_a) values for $La_{0.9}Ba_{0.1}F_{2.9}$ and $BaSnF_4$ were 0.48 and 0.34 eV, respectively.

Ionic Conductivity of Interlayer Electrolytes. Interlayer electrolyte pellets were fabricated by uniaxial pressing the layers of $La_{0.9}Ba_{0.1}F_{2.9}$ (70 or 20 or 10 mg) and $BaSnF_4$ (70 or 120 or 130 mg) together at 2 tons for 1 min using a desktop press. The thickness and diameter of the pellets were measured to be approximately 0.88 and 7 mm, respectively. The interlayer pellet was examined by SEM and EDX. Figure 3 shows the cross-sectional SEM image and the corresponding EDX maps obtained for an interlayer electrolyte pellet ($La_{0.9}Ba_{0.1}F_{2.9}$ (20 mg)/$BaSnF_4$ (120 mg). The thickness of each electrolyte layer was measured by cross-sectional SEM (Figure 3a) and was found to be 90 and 650 μm for the $La_{0.9}Ba_{0.1}F_{2.9}$ and $BaSnF_4$ layer, respectively. The SEM image shows that the thin layer of $La_{0.9}Ba_{0.1}F_{2.9}$ uniformly attached to the $BaSnF_4$ layer, which can physically separate $BaSnF_4$ and anode layer. The EDX maps revealed a clear boundary between the $BaSnF_4$ and $La_{0.9}Ba_{0.1}F_{2.9}$ layer. While fluoride is distributed all across the pellet, Sn and La are confined in respective layers. This indicates that layers of final pellets did not intermix during pressing procedures of the powders.

To determine the ionic conductivity, EIS measurements were performed on the $La_{0.9}Ba_{0.1}F_{2.9}$ (70 mg)/$BaSnF_4$ (70 mg) pellet. The ionic conductivity of interlayer electrolyte was calculated from its resistance determined by impedance spectra. The total ionic conductivity (σ) of the interlayer electrolyte is calculated by eq 1

$$\sigma = d/AR \tag{1}$$

where R is the total resistance of the interlayer electrolyte is obtained from complex spectra, d is the pellet thickness, and A is the cross-sectional area of the pellet. Figure 4a and b shows related Nyquist plots of the electrolyte obtained at temperatures of 25 and 100 °C. The equivalent circuit for fitting the curves is shown in Figure 4e. Extracted parameters are presented in Table S2. All EIS spectra have similar features: despite having two different electrolytes, the EIS spectra consist of a single depressed semicircle at high frequencies and a tilted straight line at low frequencies. The presence of one semicircle indicates that the conduction mechanism is dominated either by grain boundary or bulk phenomena. The total resistance and thereby the conductivity of the electrolyte pellet was determined by fitting the Nyquist plots to the equivalent circuit (Figure 4e). From the Nyquist plots, it is evident that the radius of a semicircle for interlayer electrolyte is much smaller than that of pure $La_{0.9}Ba_{0.1}F_{2.9}$ (for all measured temperatures). The calculated ionic conductivity of the $La_{0.9}Ba_{0.1}F_{2.9}$ (70 mg)/$BaSnF_4$ (70 mg) electrolyte at RT was 0.8 × 10^{-6} S cm^{-1}, which is two times higher compared to pure $La_{0.9}Ba_{0.1}F_{2.9}$ (0.4 × 10^{-6} S cm^{-1}) at RT.

To further improve the total ionic conductivity, the amount of the $La_{0.9}Ba_{0.1}F_{2.9}$ in interlayer was reduced from 70 to 20 mg to decrease the overall resistance. In Figure 4c and d, the Nyquist plots of interlayer electrolyte $La_{0.9}Ba_{0.1}F_{2.9}$ (20 mg)/$BaSnF_4$ (120 mg) and the equivalent circuit is shown. The impedance spectra consist of a depressed semicircle at higher frequency, followed by a tilted straight line at a lower frequency similar to the spectra obtained for the $La_{0.9}Ba_{0.1}F_{2.9}$ (70 mg)/$BaSnF_4$ (70 mg) pellet. Thus, the total ionic conductivity of the interlayer $La_{0.9}Ba_{0.1}F_{2.9}$ (20 mg)/$BaSnF_4$ (120 mg) electrolyte improved by more than 1 order of magnitude for all tested temperatures to become 0.35 × 10^{-5} S cm^{-1} at RT (Table S2). We estimated the capacitance associated with Q2 and Q3 to find the dominating conduction mechanism: Q2 was in the range of 10^{-8}–10^{-10} F, and the tilted straight line gives for Q3 a value close to 10^{-6} F (Table S2). The Q2 values can be related to grain boundaries phenomena (10^{-11}–10^{-8} F), and the Q3 values are consistent with electrolyte–electrode interfaces phenomena (10^{-7}–10^{-5} F).[41] Also, it is interesting to note that the Q2 value for $La_{0.9}Ba_{0.1}F_{2.9}$ (20 mg)/$BaSnF_4$ (120 mg) was 6 × 10^{-8} F, whereas for $La_{0.9}Ba_{0.1}F_{2.9}$ (70 mg)/$BaSnF_4$ (70 mg) it was 2 × 10^{-10} F at RT. These high capacitances reveal that there is a significant contribution from bulk or grain boundaries (R2). Since the impedance spectra are expected to have two

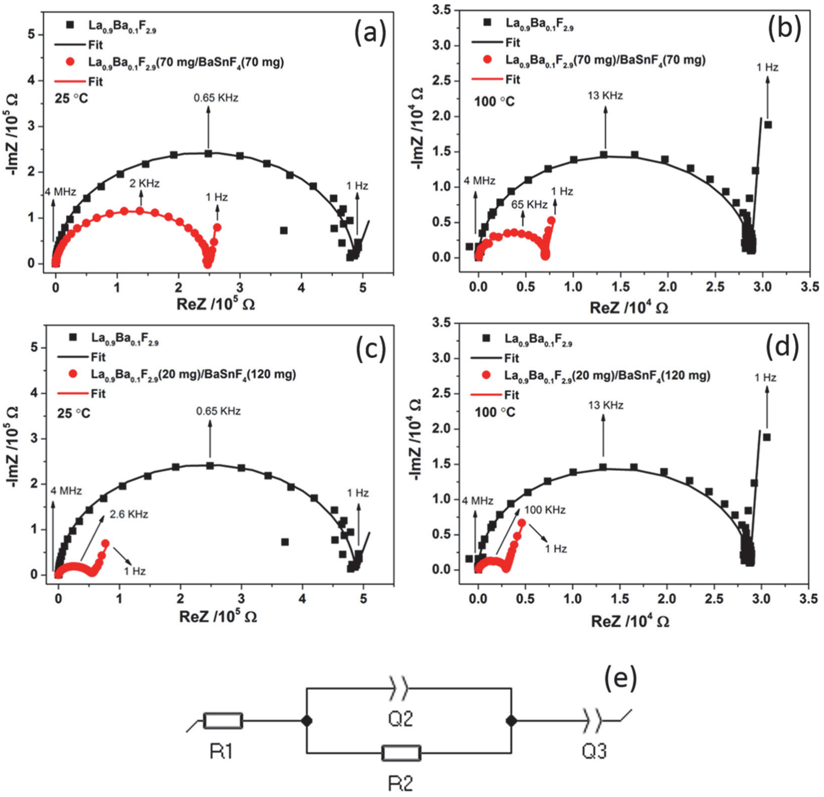

Figure 4. Nyquist plots obtained at (a) 25 and (b) 100 °C for $La_{0.9}Ba_{0.1}F_{2.9}$ (70 mg)/$BaSnF_4$ (70 mg) and $La_{0.9}Ba_{0.1}F_{2.9}$ pellets. Nyquist plots obtained at (c) 25 and (d) 100 °C for $La_{0.9}Ba_{0.1}F_{2.9}$ (20 mg)/$BaSnF_4$ (120 mg) and $La_{0.9}Ba_{0.1}F_{2.9}$ pellets. (e) Represent equivalent circuit used to fit the EIS spectra. R1 and R2 correspond to contact resistance and total resistance (bulk and grain boundary), respectively. Q2 and Q3 represent capacitance associated with R2 (bulk and grain boundary) and blocking electrodes, respectively.

semicircles corresponding to two electrolytes ($BaSnF_4$ and $La_{0.9}Ba_{0.1}F_{2.9}$), the absence of the second semicircle indicates that there is no significant resistance across the $BaSnF_4$ electrolyte and the interface between the two layers.

We have further reduced the interlayer amount of $La_{0.9}Ba_{0.1}F_{2.9}$ electrolyte to 10 mg. Figure 5a–d depicts the Nyquist plot of $La_{0.9}B_{0.1}F_{2.9}$ (10 mg)/$BaSnF_4$ (130 mg) pellet obtained at 25, 60, 100, and 150 °C. Figure 5e shows the equivalent circuit used for the fitting impedance spectra. The Nyquist plot of this thinner interlayer electrolyte consists of two highly depressed semicircles (at high and intermediate frequencies) and a tilted straight line at lower frequencies (Figure 5a). From these, we have estimated the capacitances associated with Q2 and Q3: 10^{-9} F and 10^{-6} F, respectively (Table S3).[41] The total ionic conductivity of $La_{0.9}Ba_{0.1}F_{2.9}$ (10 mg)/$BaSnF_4$ (130 mg) is 0.89×10^{-5} S cm^{-1} at RT, which is roughly 22 times higher compared to pure $La_{0.9}Ba_{0.1}F_{2.9}$ (4×10^{-7} S cm^{-1}) but around 39 times smaller than pure $BaSnF_4$ (3.5×10^{-4} S cm^{-1}). The total ionic conductivity increased with rising temperature. At 60 °C, the total ionic conductivity of $La_{0.9}Ba_{0.1}F_{2.9}$ (10 mg)/$BaSnF_4$ (130 mg) increased to 2.8×10^{-4} S cm^{-1}, approaching that of pure $BaSnF_4$ at RT (Table S3). On the basis of capacitance values, the first semicircle at high frequencies was attributed to the combined contribution of resistance from bulk and grain boundaries of the interlayer ($La_{0.9}Ba_{0.1}F_{2.9}$). The second highly depressed semicircle at intermediate frequencies corresponds to the resistance of the interface of the two layers. The appearance of this second semicircle indicates that the interfacial resistance contribution was not suppressed as for the $La_{0.9}Ba_{0.1}F_{2.9}$ (20 or 70 mg)/$BaSnF_4$ (120 or 70 mg) systems. On the basis of the capacitance values, it becomes evident that the contribution from interfacial resistance becomes higher as the thickness of the $La_{0.9}Ba_{0.1}F_{2.9}$ electrolyte layer is reduced.

Full Cell Assembly and Testing. To validate the compatibility of the interlayer electrolyte with high electropositive metals like Ce, we assembled FIB cells utilizing $La_{0.9}Ba_{0.1}F_{2.9}$ (20 mg)/$BaSnF_4$ (120 mg) as an electrolyte, BiF_3 composite as cathode and Ce composite as an anode. The cathode composite consisted of BiF_3, $BaSnF_4$, and MWCNT. The anode composite was made from Ce, LBF, and MWCNT. The pellets were fabricated by pressing the anode composite, $La_{0.9}Ba_{0.1}F_{2.9}$, $BaSnF_4$, and cathode composite (BiF_3) together using a desktop press. Though the ionic conductivity of $La_{0.9}Ba_{0.1}F_{2.9}$ (10 mg)/$BaSnF_4$ (130 mg) electrolyte is higher compared to $La_{0.9}Ba_{0.1}F_{2.9}$ (20 mg)/$BaSnF_4$ (120 mg), we used

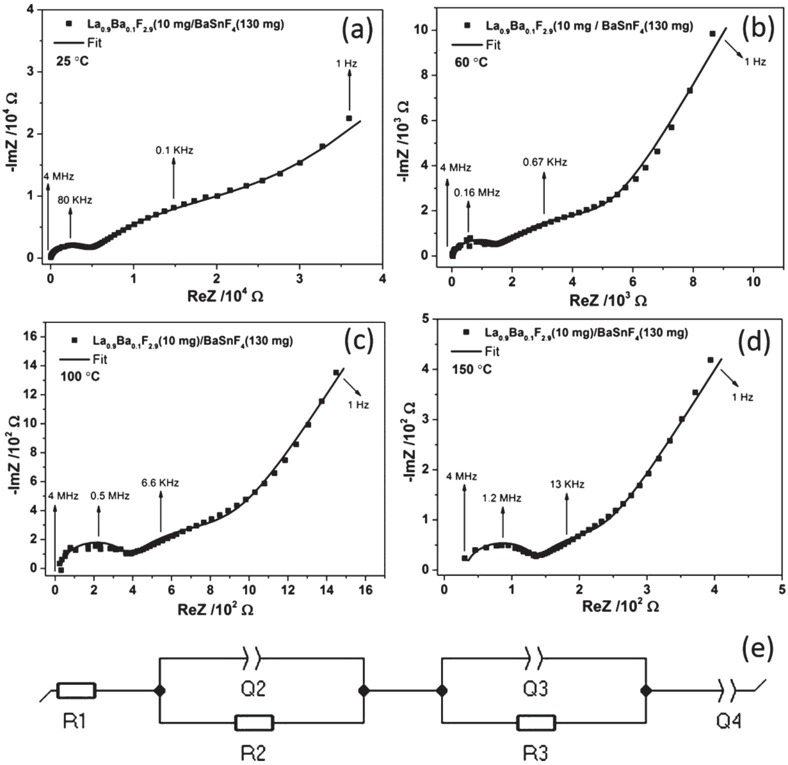

Figure 5. Nyquist plot obtained at (a) 25 (b), 60, (c), 100, and (d) 150 °C for $La_{0.9}Ba_{0.1}F_{2.9}$ (10 mg)/$BaSnF_4$ (130 mg) pellet. In panel e, the corresponding equivalent circuit for fitting the plots is depicted. R1, R2, and R3 correspond to contact resistance, total resistance (bulk and grain boundary), and interfacial resistance, respectively. Q2, Q3, and Q4 represent capacitance associated with R2 (bulk and grain boundary), R3 (interface), and the blocking electrodes, respectively.

the later composition to avoid the possibility of physical contact between the anode and $BaSnF_4$ electrolyte. Figure 6 shows the cross-sectional SEM image of the pellet and corresponding EDX mapping. The average thickness for the anode, $La_{0.9}Ba_{0.1}F_{2.9}$, $BaSnF_4$, and cathode layers was determined to be 80, 90, 670, and 45 μm, respectively. EDX analysis was carried out to map the elemental distribution. Fluoride was distributed homogeneously across the pellet. Sn was detected in the cathode and $BaSnF_4$ layers. La was distributed in $La_{0.9}Ba_{0.1}F_{2.9}$ and in the anode layers. Ce was found in the electrolyte layer as well in addition to the anode layer. To investigate the cross sections of the pellet, we cut the pellet using an ultrasonic knife. Ce might have spread over the electrolyte layer during the cutting process of the pellet.

The open circuit voltage (OCV) of Ce/$La_{0.9}Ba_{0.1}F_{2.9}$–$BaSnF_4$/BiF_3 cell turned out to be 2.6 V. The voltage-capacity profiles of Ce/$La_{0.9}Ba_{0.1}F_{2.9}$/$BaSnF_4$/BiF_3 cell is shown in Figure 7a. The cell was operated at 25 °C with a current density of 10 μA cm^{-2}. The first discharge and charge capacities are 27 and 23 mA h g^{-1} respectively. The average first discharge and charge voltages were 1.4 and 3.2 V resulting in a large hysteresis of 1.6 V during the first cycle. Second and subsequent discharges show different behavior with an average discharge and charge voltage plateau of 2.2 and 3.0 V, with an hysteresis of 0.8 V, which is much less compared to first discharge and charge. During the second or subsequent cycles, capacity faded gradually and decreased to 3.0 mA h g^{-1} after five cycles (Figure 7a). The reason for obtaining low capacity and poor electrochemical performance is due to the low ionic conductivity of $La_{0.9}Ba_{0.1}F_{2.9}$ (20 mg)/$BaSnF_4$ (120 mg) at RT (3.5×10^{-6} S cm^{-1}).

Despite low capacity, we were able to cycle Ce/$La_{0.9}Ba_{0.1}F_{2.9}$–$BaSnF_4$/BiF_3 cell at RT, which was not feasible either using $La_{0.9}Ba_{0.1}F_{2.9}$ or $BaSnF_4$ as electrolytes. While we were not able to pass or withdraw any current from Ce/$La_{0.9}Ba_{0.1}F_{2.9}$/BiF_3 cell at RT because of the low ionic conductivity of $La_{0.9}Ba_{0.1}F_{2.9}$, Ce/$BaSnF_4$/BiF_3 cell showed an OCV of 1.2 V, which could be due to the direct interfacial reaction between Ce and $BaSnF_4$ and discharging of the cell resulted in an immediate voltage drop to 0 V (Figure 7b).

To verify the advantage of the interlayer electrolyte at higher temperatures, we have cycled the cell at 150 °C. Figure 7c shows voltage-capacity profiles of Ce/$La_{0.9}Ba_{0.1}F_{2.9}$–$BaSnF_4$/BiF_3 cell cycled at 150 °C for the first five cycles. The cell was cycled between 1.8 and 3.5 V. The first discharge capacity corresponds to 251 mA h g^{-1}, which is 83% of the theoretical specific capacity (302 mA h g^{-1}). The first discharge curve exhibits an average voltage of 2.5 V. The first charge capacity

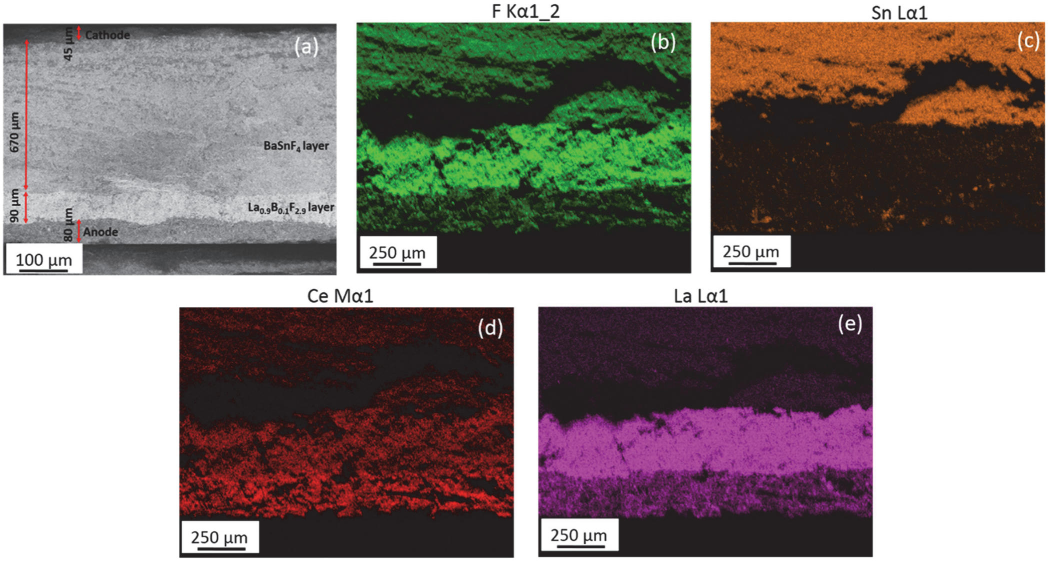

Figure 6. (a) Cross-sectional SEM view of a battery pellet (Ce/$La_{0.9}Ba_{0.1}F_{2.9}$ (20 mg)-$BaSnF_4$ (120 mg)/BiF_3. Also, cross-sectional views with EDX mapping images (b–e) of F, Sn, Ce, and La are shown.

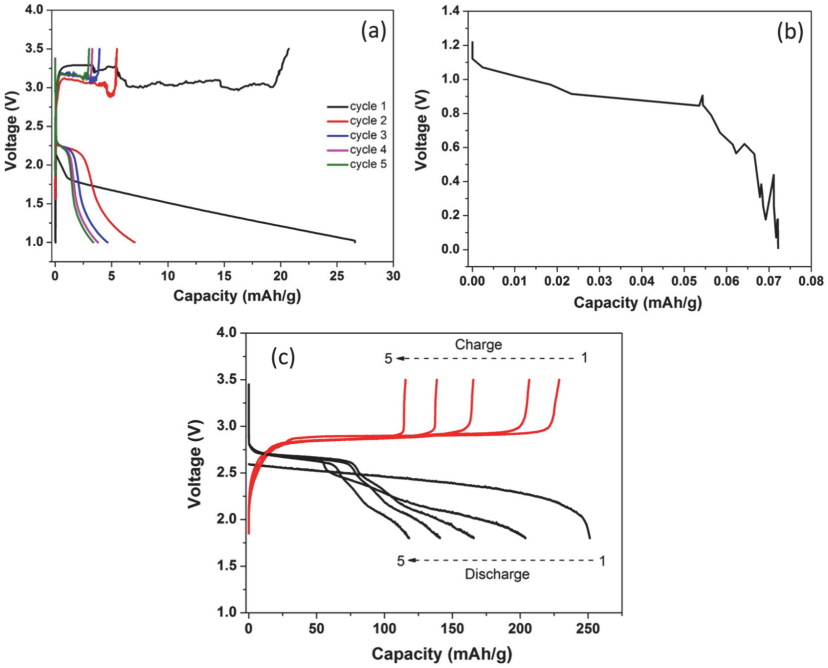

Figure 7. Voltage–capacity profiles obtained at 25 °C with a current density of 10 $\mu A\ cm^{-2}$ for the (a) Ce/$La_{0.9}Ba_{0.1}F_{2.9}$–$BaSnF_4$/BiF_3 and (b) Ce/$BaSnF_4$/BiF_3 cell. (c) Voltage–capacity profiles of the Ce/$La_{0.9}Ba_{0.1}F_{2.9}$–$BaSnF_4$/BiF_3 cell obtained at 150 °C with a current density of 10 $\mu A\ cm^{-2}$.

amounts to 228 mA h g^{-1}, which is 93% of initial discharge capacity. The first charge profile exhibits an average voltage of 2.8 V, resulting in a low hysteresis of 0.3 V during the first cycle. In the following cycles, capacity faded gradually and reached 119 mA h g^{-1} after 5 cycles. The possible reason for quick fading is due to the weakening of electrode/electrolyte interfacial contact or loss of interparticle contacts caused by reversible volume changes at BiF_3 electrode during discharge and charge process. Despite capacity fading, the interlayer electrolyte based cell shows high capacity and lower hysteresis voltage. The FIB using interlayer electrolyte shows the first discharge capacity of 61 mA h g^{-1} higher than that of reported FIB based on pure as-milled $La_{0.9}Ba_{0.1}F_{2.9}$ electrolyte.[4] In contrast to previously reported FIB, our cell showed 0.35 V higher discharge voltage.

The cathode side of cycled pellets was examined using ex situ XRD: cells were discharged at 150 °C to achieve the maximum conversion of BiF_3 to Bi. At RT only 10% of the theoretical capacity was observed with Ce anode. Ex situ XRD patterns are shown in Figure S2. Before discharge, the peaks of active material (BiF_3) and electrolyte ($BaSnF_4$) (Figure S2, bottom layer) can be observed, indicating no chemical reaction occurred between BiF_3 and $BaSnF_4$. After first discharge, the BiF_3 phase was converted entirely to Bi (Figure S2, top layer). This indicates a complete defluorination of BiF_3 at 150 °C indicating fluoride transfer across the electrolyte layers and interfaces. The electrochemical performance of the Ce/$La_{0.9}Ba_{0.1}F_{2.9}$–$BaSnF_4$/BiF_3 cells is not significant, which is mainly due to the low ionic conductivity of the interlayer electrolyte (0.35×10^{-5} S cm^{-1} at RT). Synthesis of the interlayer electrolyte with even high fluoride ion conductivity is possible by reducing the thickness of $La_{0.9}Ba_{0.1}F_{2.9}$ via chemical methods or atomic layer deposition (ALD). Earlier we have demonstrated that high reversible capacities can be achieved if the ionic conductivity of the solid electrolyte is significantly high.[34]

CONCLUSION

We have developed a new interlayer electrolyte with high fluoride ion conductivity of 0.89×10^{-5} S cm^{-1} at RT, which is compatible with high electropositive metals like Ce. The interlayer electrolyte consists of a thin layer (<50 μm) of $La_{0.9}Ba_{0.1}F_{2.9}$ and a thick layer (<700 μm) of $BaSnF_4$ electrolytes. Applying low conductive $La_{0.9}Ba_{0.1}F_{2.9}$ as thin layer enhanced the total conductivity of the pellet by an order of magnitude (compared to pure $La_{0.9}Ba_{0.1}F_{2.9}$), while it physically isolated the less stable and highly conductive electrolyte ($BaSnF_4$) from the anode. This approach allows the demonstration of relatively high voltage FIBs at RT otherwise not feasible to operate either with $BaSnF_4$ or $La_{0.9}Ba_{0.1}F_{2.9}$ electrolytes alone. We demonstrated the feasibility of operating FIB at RT utilizing the interlayer pellet as an electrolyte, BiF_3 as a cathode and Ce as anode material. Although the electrochemical performance of the Ce/$La_{0.9}Ba_{0.1}F_{2.9}$–$BaSnF_4$/BiF_3 cells is not good enough for a practical application, the approach described here would pave the way to design and development of advanced electrolytes with existing electrolytes. Further, with improved coating methods, it might be possible to achieve high ionic conductivities similar (or even higher) to that of $BaSnF_4$ while extending its electrochemical stability window.

EXPERIMENTAL SECTION

Calculation of Open Circuit Voltage. Enthalpy of formation of metal fluorides, which was used to calculate the open circuit voltage was extracted from materials project.[42]

Sample Preparation. Materials synthesis, characterization, battery assembly, and testing of cells, were carried out under argon atmosphere. Electrolyte and electrode materials were prepared by ball milling. $La_{0.9}Ba_{0.1}F_{2.9}$ and $BaSnF_4$ were synthesized according to the previous reports.[26,32] $La_{0.9}Ba_{0.1}F_{2.9}$ was synthesized by milling the stoichiometric amounts of BaF_2 (Sigma-Aldrich, 99.9%) and LaF_3 (Sigma-Aldrich, 99.9%, anhydrous) for 12 h at 600 rpm under an Ar atmosphere. Milling was performed using silicon nitride vial (80 mL) and balls (10 mm in diameter) with a ball to powder weight ratio of 12:1. Tetragonal $BaSnF_4$ was synthesized in two steps: first, cubic $BaSnF_4$ was obtained by milling stoichiometric amounts of BaF_2 and SnF_2 (Alfa Aesar, 99.99%) for 12 h at 600 rpm using ZrO_2 vial (80 mL) and balls (10 mm in diameter), and in the second step, the tetragonal phase was achieved by heating cubic $BaSnF_4$ at 300 °C for 2 h under Ar atmosphere. The BiF_3 (Sigma-Aldrich, 99.99%) cathode composite was prepared by mixing active material BiF_3 (40 wt %), $BaSnF_4$ (50 wt %), and MWCNT (10 wt %) together at 300 rpm for 12 h. Ce anode composite was synthesized by milling stoichiometric amounts of Ce powder (Alfa Aesar, 99.9% (REO)) and multiwalled carbon nanotubes (MWCNT) (Sigma-Aldrich, 95%) gently at 200 rpm for 2 h. In the second step, Ce–C composite was added to the $La_{0.9}Ba_{0.1}F_{2.9}$ electrolyte in an appropriate weight ratio (Ce: $La_{0.9}Ba_{0.1}F_{2.9}$: MWCNT = 50:40:10) and milled further for 2 h at 100 rpm. The MWCNT and electrolyte were added to ensure the ionic and electronic conductivity of electrodes.

Characterization. *X-ray Diffraction (XRD).* X-ray diffraction (XRD) analysis of the electrolyte and electrode composites was performed using a STOE STADI-P instrument with Mo–Kα source. Ex situ XRD was performed using a Bruker D8 Advance diffractometer operating with Cu Kα radiation (λ = 0.154 nm) in the 2θ range of 20–60°. Pellets after electrochemical testing were loaded into dome-type sample holders (Bruker AXS Inc.) equipped with a knife edge beam stop for low background and sealed inside an Ar-filled glovebox. Profile matching refinements were performed on the XRD patterns for cell average crystallite size calculation, using Langford's method with the FullProf software.[43]

Scanning Electron Microscopy (SEM) and Energy Dispersive X-ray (EDX) Spectroscopy. The morphology of samples was investigated using high-resolution scanning electron microscopy (LEO 1550VP Field Emission SEM, Zeiss) equipped with an energy-dispersive spectrometer. To avoid contact with the external environment, samples were prepared in the glovebox and transferred into SEM chamber using inert atmosphere transfer box.

Electrochemical Impedance Spectroscopy (EIS). Ionic conductivity was evaluated from EIS spectra recorded on pellets (7 mm diameter and ~0.88 mm thickness) pressed at 2 tons for 1 min and sputtered with gold metal on both sides as an ion blocking electrodes. EIS spectra were recorded using Zahner/IM6 device at temperatures ranging from 25 to 200 °C under Ar atmosphere. Measurements were carried out over a wide range frequency range from 8 MHz to 1 Hz with a voltage amplitude of 10 mV. The EIS data were fitted using EC-Lab software by applying an equivalent circuit.

Battery Fabrication and Electrochemical Testing. All solid-state fluoride ion battery pellets were fabricated by pressing anode composite (Ce), thin-layer $La_{0.9}Ba_{0.1}F_{2.9}$, $BaSnF_4$ electrolytes, and cathode composite (BiF_3) together using a desktop press (Specac) inside an argon-filled glovebox with water and oxygen contents below 0.1 ppm. The pellet was then transferred to a modified Swagelok type cell. Stainless steel discs were used as current collectors. Electrochemical testing of cells was performed at 25 and 150 °C using an Arbin battery tester (BT-2000) in galvanostatic mode. The high temperature (150 °C) cells were cycled between the voltage of 1.8 and 3.5 V at a current density of 10 μA cm^{-2}, while the RT cells were operated between 1.0 to 3.5 V at this current density. The specific capacities were calculated referring to the weight of the active material (BiF_3) in the cathode since anode was used in excess.

ASSOCIATED CONTENT

Supporting Information

The Supporting Information is available free of charge on the ACS Publications website at DOI: 10.1021/acsaem.8b02166.

> Nyquist plots of $La_{0.9}Ba_{0.1}F_{2.9}$ and $BaSnF_4$ obtained at different temperature, XRD patterns of BiF_3 side of battery pellet before and after discharge until 1.8 V, table of open circuit voltages of various metal/metal fluoride redox couples, table of fitting parameters of the Nyquist plots for $La_{0.9}Ba_{0.1}F_{2.9}$, $La_{0.9}Ba_{0.1}F_{2.9}$ (70 mg)/$BaSnF_4$ (70 mg), $La_{0.9}Ba_{0.1}F_{2.9}$ (20 mg)/$BaSnF_4$ (120 mg), and $La_{0.9}B_{0.1}F_{2.9}$ (10 mg)/$BaSnF_4$ (130 mg) (PDF)

AUTHOR INFORMATION

Corresponding Author

*E-mail: munnangi.reddy@kit.edu.

ORCID

Raiker Witter: 0000-0002-7085-2490
M. Anji Reddy: 0000-0001-9101-0252

Notes

The authors declare no competing financial interest.

ACKNOWLEDGMENTS

Financial support by the European Union through the European Regional Development Fund (Dora Plus Action 1) and Estonian Ministry of Education and Research through Grants PUT 1534. The authors gratefully thank Mr. Tobias Braun and Dr. Johann Chable, Helmholtz Institute Ulm, for assisting the SEM and EIS measurements. R.W. is gratefully acknowledging Tallinn University of Technology and Karlsruhe Institute of Technology. Funding is also acknowledged by the HORIZON 2020 FET-OPEN project “LiRichFCC” (Grant 711792). This work contributes to the research performed at CELEST (Center for Electrochemical Energy Storage Ulm-Karlsruhe).

REFERENCES

(1) Slater, M. D.; Kim, D.; Lee, E.; Johnson, C. S. Sodium-Ion Batteries. *Adv. Funct. Mater.* **2013**, *23*, 947−958.

(2) Zhao-Karger, Z.; Zhao, X. Y.; Wang, D.; Diemant, T.; Behm, R. J.; Fichtner, M. Performance Improvement of Magnesium Sulfur Batteries with Modified Non-Nucleophilic Electrolytes. *Adv. Energy Mater.* **2015**, *5*, 1401155.

(3) Lin, M. C.; Gong, M.; Lu, B. G.; Wu, Y. P.; Wang, D. Y.; Guan, M. Y.; Angell, M.; Chen, C. X.; Yang, J.; Hwang, B. J.; Dai, H. J. An Ultrafast Rechargeable Aluminium-Ion Battery. *Nature* **2015**, *520*, 324−328.

(4) Reddy, M. A.; Fichtner, M. Batteries Based on Fluoride Shuttle. *J. Mater. Chem.* **2011**, *21*, 17059−17062.

(5) Kennedy, J. H.; Hunter, J. C. Thin Film Galvanic Cell Pb/PbF_2/PbF_2, CuF_2/Cu. *J. Electrochem. Soc.* **1976**, *123*, 10−14.

(6) Baukal, W. Solid-Electrolyte CellGer. Offen.DE 2017128, 1971.

(7) Baukal, W.; Knodler, R.; Kuhn, W. Overview of the Applications of Solid Electrolytes. *Chem. Ing. Tech.* **1978**, *50*, 245−249.

(8) Hagenmuller, P.; Reau, J. M.; Lucat, C.; Matar, S.; Villeneuve, G. Ionic Conductivity of Fluorite-Type Fluorides. *Solid State Ionics* **1981**, 3−4, 341−345.

(9) Schoonman, J. A Solid-State Galvanic Cell with Fluoride-Conducting Electrolytes. *J. Electrochem. Soc.* **1976**, *123*, 1772−1775.

(10) Potanin, A. A. Solid State Chemical Current Source Based on Ionic Conductor of the Lanthanum Trifluoride Type. *J. Russ. Chem. Soc.* **2001**, *45*, 58−63.

(11) Rongeat, C.; Reddy, M. A.; Witter, R.; Fichtner, M. Nano-Structured Fluorite-Type Fluorides as Electrolytes for Fluoride Ion Batteries. *J. Phys. Chem. C* **2013**, *117*, 4943−4950.

(12) Rongeat, C.; Reddy, M. A.; Diemant, T.; Behm, R. J.; Fichtner, M. Development of New Anode Composite Materials for Fluoride Ion Batteries. *J. Mater. Chem. A* **2014**, *2*, 20861−20872.

(13) Clemens, O.; Rongeat, C.; Reddy, M. A.; Giehr, A.; Fichtner, M.; Hahn, H. Electrochemical Fluorination of Perovskite Type $BaFeO_{2.5}$. *Dalton Trans.* **2014**, *43*, 15771−15778.

(14) Hammad Fawey, M.; Chakravadhanula, V. S. K.; Reddy, M. A.; Rongeat, C.; Scherer, T.; Hahn, H.; Fichtner, M.; Kübel, C. In Situ TEM Studies of Micron-Sized All-Solid-State Fluoride Ion Batteries: Preparation, Prospects, and Challenges. *Microsc. Res. Tech.* **2016**, *79*, 615−624.

(15) Nowroozi, M. A.; Wissel, K.; Rohrer, J.; Reddy, M. A.; Clemens, O. $LaSrMnO_4$: Reversible Electrochemical Intercalation of Fluoride Ions in the Context of Fluoride Ion Batteries. *Chem. Mater.* **2017**, *29*, 3441−3453.

(16) Nowroozi, M. A.; Ivlev, S.; Rohrer, J.; Clemens, O. La_2CoO_4: A New Intercalation Based Cathode Material for Fluoride Ion Batteries with Improved Cycling Stability. *J. Mater. Chem. A* **2018**, *6*, 4658−4669.

(17) Zhang, L.; Reddy, M. A.; Gao, P.; Fichtner, M. Development of Dense Solid State Thin-Film Electrolyte for Fluoride Ion Batteries. *J. Alloys Compd.* **2016**, *684*, 733−738.

(18) Zhang, L.; Reddy, M. A.; Gao, P.; Diemant, T.; Jürgen Behm, R.; Fichtner, M. Study of All Solid-State Rechargeable Fluoride Ion Batteries Based on Thin-Film Electrolyte. *J. Solid State Electrochem.* **2017**, *21*, 1243−1251.

(19) Zhang, L.; Reddy, M. A.; Fichtner, M. Electrochemical Performance of All Solid-State Fluoride-Ion Batteries Based on Thin-Film Electrolyte Using Alternative Conductive Additives and Anodes. *J. Solid State Electrochem.* **2018**, *22*, 997−1006.

(20) Grenier, A.; Porras-Gutierrez, A. G.; Body, M.; Legein, C.; Chrétien, F.; Raymundo-Piñero, E.; Dollé, M.; Groult, H.; Dambournet, D. Solid Fluoride Electrolytes and Their Composite with Carbon: Issues and Challenges for Rechargeable Solid State Fluoride-Ion Batteries. *J. Phys. Chem. C* **2017**, *121*, 24962−24970.

(21) Grenier, A.; Porras-Gutierrez, A.-G.; Groult, H.; Beyer, K. A.; Borkiewicz, O. J.; Chapman, K. W.; Dambournet, D. Electrochemical Reactions in Fluoride-Ion Batteries: Mechanistic Insights from Pair Distribution Function Analysis. *J. Mater. Chem. A* **2017**, *5*, 15700−15705.

(22) Darolles, I.; Weiss, C. M.; Alam, M. M.; Tiruvannamalai, A.; Jones, S. C. Fluoride Ion Battery Compositions. U.S. Patent US20120164541 A1, 2012.

(23) Gschwind, F.; Bastien, J. Parametric Investigation of Room-Temperature Fluoride-Ion Batteries: Assessment of Electrolytes, Mg-Based Anodes, and BiF_3-Cathodes. *J. Mater. Chem. A* **2015**, *3*, 5628−5634.

(24) Okazaki, K.-I.; Uchimoto, Y.; Abe, T.; Ogumi, Z. Charge-Discharge Behavior of Bismuth in a Liquid Electrolyte for Rechargeable Batteries Based on a Fluoride Shuttle. *ACS Energy Lett.* **2017**, *2*, 1460−1464.

(25) Dieudonné, B.; Chable, J.; Body, M.; Legein, C.; Durand, E.; Mauvy, F.; Fourcade, S.; Leblanc, M.; Maisonneuve, V.; Demourgues, A. The Key Role of the Composition and Structural Features in Fluoride Ion Conductivity in Tysonite $Ce_{1-x}Sr_xF_{3-x}$ Solid Solutions. *Dalton Trans.* **2017**, *46*, 3761−3769.

(26) Dieudonné, B.; Chable, J.; Mauvy, F.; Fourcade, S.; Durand, E.; Lebraud, E.; Leblanc, M.; Legein, C.; Body, M.; Maisonneuve, V.; Demourgues, A. Exploring the $Sm_{1-x}Ca_xF_{3-x}$ Tysonite Solid Solution as a Solid-State Electrolyte: Relationships Between Structural Features and F^- Ionic Conductivity. *J. Phys. Chem. C* **2015**, *119*, 25170−25179.

(27) Thieu, D. T.; Fawey, M. H.; Bhatia, H.; Diemant, T.; Chakravadhanula, V. S. K.; Behm, R. J.; Kübel, C.; Fichtner, M. CuF_2

as Reversible Cathode for Fluoride Ion Batteries. *Adv. Funct. Mater.* **2017**, *27*, 1701051.

(28) Mohammad, I.; Chable, J.; Witter, R.; Fichtner, M.; Reddy, M. A. Synthesis of Fast Fluoride-Ion-Conductive Fluorite-Type $Ba_{1-x}Sb_xF_{2+x}$ ($0.1 \leq x \leq 0.4$): A Potential Solid Electrolyte for Fluoride-Ion Batteries. *ACS Appl. Mater. Interfaces* **2018**, *10*, 17249−17256.

(29) Goodenough, J. B.; Park, K.-S. The Li-Ion Rechargeable Battery: A Perspective. *J. Am. Chem. Soc.* **2013**, *135*, 1167−1176.

(30) Wang, F.; Grey, C. P. Probing the Mechanism of Fluoride-Ion Conduction in LaF_3 and Strontium-Doped LaF_3 with High-Resolution ^{19}F MAS NMR. *Chem. Mater.* **1997**, *9*, 1068−1070.

(31) Schoonman, J.; Oversluizen, G.; Wapenaar, K. E. D. Solid Electrolyte Properties of LaF_3. *Solid State Ionics* **1980**, *1*, 211−221.

(32) Sorokin, N. I.; Krivandina, E. A.; Zhmurova, Z. I.; Sobolev, B. P.; Fominykh, M. V.; Fistul, V. V. Superionic Conductivity of the Heterovalent Solid Solutions $R_{1-x}M_xF_{3-x}$ (R = REE, M= Ca, Ba) with Tysonite-Type Structure. *Phys. Solid State* **1999**, *41*, 573−575.

(33) Rongeat, C.; Reddy, M. A.; Witter, R.; Fichtner, M. Solid Electrolytes for Fluorides Ion Batteries: Ionic Conductivity in Polycrystalline Tysonite-Type Fluorides. *ACS Appl. Mater. Interfaces* **2014**, *6*, 2103−2110.

(34) Mohammad, I.; Witter, R.; Fichtner, M.; Reddy, M. A. Room Temperature Rechargeable Solid State Fluoride Ion Batteries. *ACS Appl. Energy Mater.* **2018**, *1*, 4766−4775.

(35) Chaudhuri, S.; Wang, F.; Grey, C. P. Resolving the Different Dynamics of the Fluorine Sublattices in the Anionic Conductor $BaSnF_4$ by Using High-Resolution MAS NMR Techniques. *J. Am. Chem. Soc.* **2002**, *124*, 11746−11757.

(36) Preishuber-Pflügl, F.; Epp, V.; Nakhal, S.; Lerch, M.; Wilkening, M. Defect-Enhanced F^- ion Conductivity in Layer-Structured Nanocrystalline $BaSnF_4$ Prepared by High-Energy Ball Milling Combined with Soft Annealing. *Phys. Status Solidi (c)* **2015**, *12*, 10−14.

(37) Ahmad, M. M.; Yamane, Y.; Yamada, K. Structure, Ionic Conduction, and Giant Dielectric Properties of Mechanochemically Synthesized $BaSnF_4$. *J. Appl. Phys.* **2009**, *106*, 074106.

(38) Liu, B.; Gong, Y.; Fu, K.; Han, X.; Yao, Y.; Pastel, G.; Yang, C.; Xie, H.; Wachsman, E. D.; Hu, L. Garnet Solid Electrolyte Protected Li-Metal Batteries. *ACS Appl. Mater. Interfaces* **2017**, *9*, 18809−18815.

(39) Kim, J.-K.; Mueller, F.; Kim, H.; Bresser, D.; Park, J.-S.; Lim, D.-H.; Kim, G.-T.; Passerini, S.; Kim, Y. Rechargeable-Hybrid-Seawater Fuel Cell. *NPG Asia Mater.* **2014**, *6*, e144.

(40) Zhou, W.; Li, Y.; Xin, S.; Goodenough, J. B. Rechargeable Sodium All-Solid-State Battery. *ACS Cent. Sci.* **2017**, *3*, 52−57.

(41) Irvine, J. T. S.; Sinclair, D. C.; West, A. R. Electroceramics: Characterization by Impedance Spectroscopy. *Adv. Mater.* **1990**, *2*, 132−138.

(42) Jain, A.; Hautier, G.; Ong, S. P.; Moore, C.; Fischer, C.; Persson, K.; Ceder, G. Formation Enthalpies by Mixing GGA and GGA + U Calculations. *Phys. Rev. B: Condens. Matter Mater. Phys.* **2011**, *84*, 045115.

(43) Langford, J. A Rapid Method for Analysing the Breadths of Diffraction and Spectral Lines Using the Voigt Function. *J. Appl. Crystallogr.* **1978**, *11*, 10−14.

Publication IV

Mohammad, I.; Witter, R., Testing Mg as an anode against BiF_3 and SnF_2 cathodes for room temperature rechargeable fluoride ion batteries. *Materials Letters* 2019, 244, 159-162.

https://www.sciencedirect.com/science/article/pii/S0167577X19302769

Materials Letters 244 (2019) 159–162

Contents lists available at ScienceDirect

Materials Letters

journal homepage: www.elsevier.com/locate/mlblue

Testing Mg as an anode against BiF_3 and SnF_2 cathodes for room temperature rechargeable fluoride ion batteries

Irshad Mohammad [a], Raiker Witter [a,b,c,*]

[a] School of Information Technologies, Tallinn University of Technology, Akadeemia tee 15A, 12618 Tallinn, Estonia
[b] Institute of Nanotechnology, Karlsruhe Institute of Technology (KIT), POB 3640, 76021 Karlsruhe, Germany
[c] Institute of Quantum Optics, University Ulm, Albert-Einstein-Allee 11, 89081 Ulm, Germany

ARTICLE INFO

Article history:
Received 3 January 2019
Received in revised form 4 February 2019
Accepted 6 February 2019
Available online 15 February 2019

Keywords:
Fluoride ion batteries
$LiPF_6$
Mg + MgF_2 anode
BiF_3 and SnF_2 cathodes
Energy storage devices

ABSTRACT

In the attempt of developing post-lithium technologies for electrochemical energy storage devices, rechargeable batteries based on fluoride shuttle have recently attracted attention due to the perspective of achieving high energy densities. In this study, we present relatively high voltage room temperature rechargeable fluoride ion batteries (FIBs) using a liquid electrolyte. FIBs were built using $LiPF_6$ as an electrolyte, Mg + MgF_2 as an anode, and BiF_3 and SnF_2 as cathodes. We have investigated two types of FIB systems such as $Mg+MgF_2/LiPF_6/BiF_3$, and $Mg+MgF_2/LiPF_6/SnF_2$ at room temperature. The electrochemical analyzes were performed on sealed steel case coin cells containing a FIB pellet. A current density of 38 $\mu A\,cm^{-2}$ was applied. First discharge capacities of 160 and 185 $mA{\cdot}h{\cdot}g^{-1}$ were obtained for the $Mg+MgF_2/LiPF_6/BiF_3$ and $Mg+MgF_2/LiPF_6/SnF_2$ electrochemical systems, respectively. The reaction mechanisms of these FIBs were investigated by X-ray diffraction, impedance measurements, cyclic voltammetry and constant current battery cycling.

1. Introduction

The usage of batteries and supercapacitors has become a daily life routine due to usage in all kinds of portable and mobile electric devices. Nowadays, supercapacitors are being used to increase the efficiency of hybrid electric vehicles. Recently, two prototypes of supercapacitors were developed [1]. On the other hand, batteries are increasingly demanded to store energy generated by various renewable sources. Until now, several types of batteries based on cation chemistries such as Li^+, Na^+, K^+, Mg^{2+}, Al^{3+} have been widely investigated [2–6]. Apart from this, alternative battery technologies based on anions as charge carriers such as Cl^- and F^- have been reported [7,8]. The chloride ion battery (CIB) was recently demonstrated by Fichtner's group using ionic liquid or organic solvent-based electrolytes [7,9]. Since then, development of the chloride system has significantly progressed [10–12]. Whereas the fluoride ion battery (FIB) concept was introduced a long time ago, it was largely overlooked until Anji and Fichtner demonstrated the reversibility of solid state fluoride ion batteries [8]. FIBs offer high theoretical energy densities more than 5000 $Wh{\cdot}L^{-1}$, when an appropriate combination of electrodes is used. The high energy density is due to the large change in free energy during the formation of the different metal fluorides, resulting in high theoretical voltages. Further, more than one electron can be reversibly stored when bivalent or trivalent metals react with several fluorides, yielding high theoretical specific capacities. Apart from high theoretical energy promises, fluoride ion batteries provide high thermal stability and better safety due to low-toxicity of metal fluorides. Currently, FIB systems are in an early stage of development and large improvements are needed regarding the performance of electrodes and electrolytes.

Fluoride ion batteries have been investigated mostly using solid electrolytes, however, they were operated at a temperature of 150 °C or above [8,13–16]. Up to date, only a handful number of papers demonstrated that FIBs are performing at room temperature. In our recent report, we have shown room-temperature rechargeable solid state FIBs using solid electrolyte. We have constructed these FIBs with $BaSnF_4$ as an electrolyte, BiF_3 as a cathode, Sn and Zn as anodes [17]. Other reports investigated room temperature FIBs (RT-FIBs) employing liquid electrolytes. Recently, rechargeable RT-FIB was demonstrated applying ionic-based liquid electrolyte, Bi as a cathode, and PbF_2 as anode [18]. However, all the rechargeable RT-FIBs apply low electropositive metals as an anode, resulting in low operating voltages. In an earlier report, RT-FIBs were investigated using poly(ethylene glycol) (PEG) based compound as liquid electrolyte, Mg as an anode, and BiF_3 as a cathode, but reversibility of FIBs was not achieved [19]. In this present

---

[*] Corresponding author.
E-mail address: raiker.witter@mail.com (R. Witter).

https://doi.org/10.1016/j.matlet.2019.02.052
0167-577X/

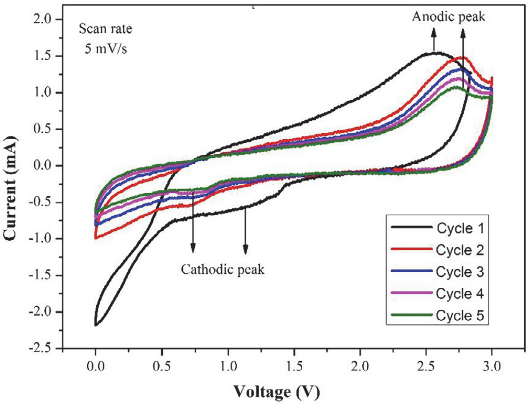

Fig. 1. Cyclic voltammogram profiles of Mg+MgF_2/$LiPF_6$/BiF_3 obtained at a scan rate of 5 mV/s.

study, we have shown the reversibility of RT-FIBs using Mg + MgF_2 composite as an anode. It was reported in an earlier patent that $LiPF_6$ as a liquid electrolyte can be used for FIBs, because it has the ability to conduct both Li^+ and PF_6^- ions, delivering via charge transfer also F^- without decomposition [20]. Here, we test the usage of $LiPF_6$ as fluoride ion transport electrolyte to build the FIBs. We have discharged BiF_3 and SnF_2 as cathodes against Mg + MgF_2 as the anode using $LiPF_6$ electrolyte.

2. Experimental

All materials preparations were carried out in an Ar-filled glove box. Bismuth trifluoride (BiF_3) (anhydrous, 98%), SnF_2 (99%) and carbon black (C.B.) were obtained from Alfa Aesar. Mg powder (99.8%) was obtained from Sigma Aldrich. The 1 M $LiPF_6$ in organic solvents and Whatman GF/D glass microfiber sheets (675 µm thickness) were purchased from Sigma Aldrich. Electrodes composites such as Mg + MgF_2, BiF_3, and SnF_2 were prepared by mechanical milling. Prior to making electrode composites, BiF_3, SnF_2, and MgF_2 were ball milled for 12 h at 600 rpm under vacuum. The milling was done by balls and jar made of silicon nitride using a planetary-type mill (Tencan). The ball to powder ratio was 16:1, and the sizes of balls were 10, 5 and 2 mm in diameters. To prepare anode composite, Mg and C.B. was first ball milled at 300 rpm for 6 h, following by adding as-milled MgF_2 in an appropriate weight ratio (Mg:MgF_2:C.B. = 50:40:10) and milled further for 6 h at 300 rpm. The cathode composites were prepared by ball milling as-milled BiF_3 or SnF_2 (90% by weight) and C.B. (10% by weight) together for 6 h at 300 rpm. Before assembling the batteries, the electrode composites were first pressed into 10 mm pellets. The pellets were pressed with a pressure of 1 ton, and the pressure was maintained for 1 min using a pellet pressing tool (Across international). The thickness of anode pellet was approximately 1 mm, whereas the thickness of cathode pellets was approximately 0.5 mm. For electrochemical analysis, the anode(pellet)/separator (soaked with $LiPF_6$)/cathode(pellet)-layers were assembled together in sealed coin cell CR2032 cases. The Galvanostatic charge-discharge tests were performed using a Keysight DC power analyzer (N6705B). The specific capacities were calculated on the basis of the weight of active material in cathodes since the anode

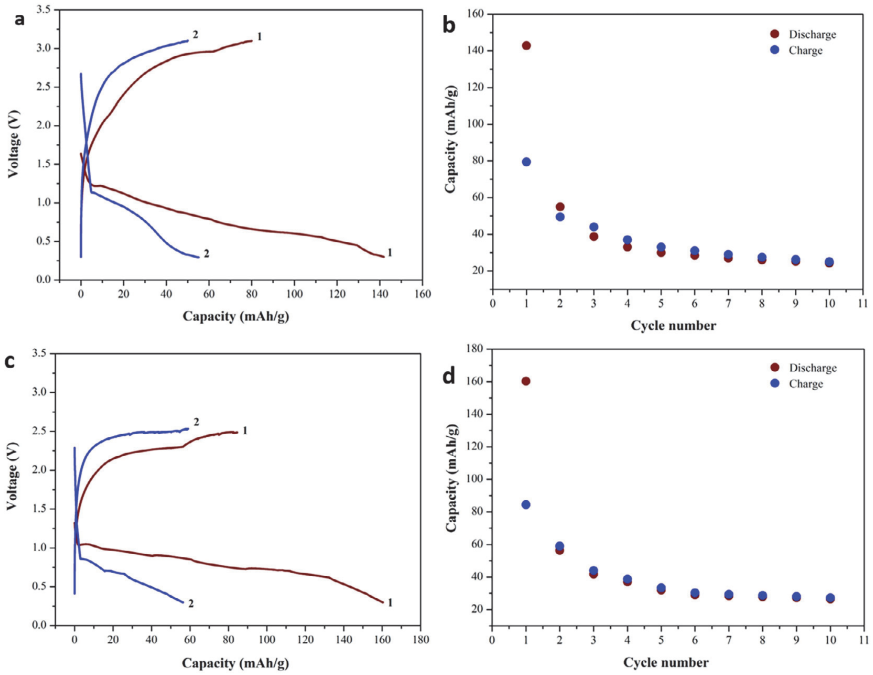

Fig. 2. Electrochemical studies of the Mg+MgF_2/$LiPF_6$/BiF_3-cell: (a) first two charge-discharge curves, (b) cycling behaviour; and the Mg+MgF_2/$LiPF_6$/SnF_2-cell: (c) first two charge-discharge curves, (d) cycling behaviour are given.

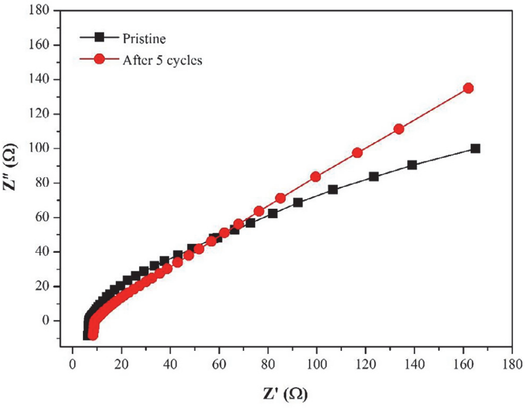

Fig. 3. Nyquist plots of Mg+MgF_2/$LiPF_6$/BiF_3-cell obtained at 25 °C before and after 5 cycles.

material was used in excess. X-ray diffraction (XRD) measurements were performed using an AXS Bruker D5005 Advance instrument with Cu Kα radiation (λ1-1.54056 Å, λ2-1.544390 Å) with variable slit.

3. Results and discussion

BiF_3 and SnF_2 were selected as cathode materials due to the fact that they possess high fluoride ion conductivity at room temperature. Also, these materials provided as cathodes for FIBs good reversibility, as reported earlier. Here, both cathodes were cycled against Mg/MgF_2 anode using $LiPF_6$ as fluoride conducting electrolyte. The cyclic voltammograms (CVs) of the Mg+MgF_2/$LiPF_6$/BiF_3-cell scanned in the potential range of 0–3 V at 25 °C are shown in Fig. 1. The CV profile of the cell consists of a cathodic and anodic peak. The cathode peak corresponds to the reduction of BiF_3 to Bi-metal, whereas the anodic peak represents the oxidation of Bi metal to BiF_3. During the first cycle, cathodic and anodic peaks appeared around 1 and 2.5 V, respectively. In the following cycle, both peak currents were gradually decreased, and their potentials shifted to the positive direction. The peak shift and decrease of anodic current could be attributed to loss of active material. However, the appearance of cathode and anode peaks indicates that bismuth fluoride is reversibly reduced and oxidized in the Mg+MgF_2/$LiPF_6$/BiF_3 cell.

Galvanostatic charge-discharge profiles and cycling behavior of Mg+MgF_2/$LiPF_6$/BiF_3-cell are given in Fig. 2a and b. The cell delivered as first discharge capacity 142 mA·h·g^{-1} at a current density of 38 μA cm^{-2} (Fig. 2a). This value is 47 % of the theoretical capacity of BiF_3 (302 mA·h·g^{-1}), suggesting partial conversion of BiF_3 to Bi. The first charge capacity was 80 mA·h·g^{-1}, meaning 56 % of capacity could be recovered from initial discharge. This demonstrates the reversibility of Mg + MgF_2 anode against BiF_3 cathode in FIB using liquid $LiPF_6$. However, in the following cycles capacity faded rapidly, after 10 cycles the discharge capacity reached 24 mA·h·g^{-1} (Fig. 2b).

Capacity fading with cycling is a well-known phenomenon in conversion type electrodes. It can be attributed to the volume changes in the electrode materials during charge and discharge processes. Volume changes may result in physical segregation of active material from electronic and ionic additives, which would result in capacity fading. Notable, we did not observe any decomposition into PF_5. Fig. 1c and d display galvanostatic charge-discharge curves and cyclic performance of Mg+MgF_2/$LiPF_6$/SnF_2-cell cycled at a current density of 38 μA cm^{-2}. The first discharge capacity amounts to 160 mA·h g^{-1}, which is 46 % of the theoretical specific capacity of SnF_2 (342 mA·h·g^{-1}), indicating that an incomplete reaction occurred at electrodes (Fig. 2c). The first charge capacity was 85 mA·h·g^{-1} and in the subsequent cycles capacity rapidly declined, reaching after 10 cycles a discharge capacity of 27 mA·h·g^{-1} (Fig. 2d). The volume changes at electrodes during the charge-discharge process might be a possible reason for capacity fading. Further investigations are needed. Possibly, the passivation layer of MgF_2 at the anode might also contribute to that. In SEM and EDX studies of the Mg anode, the formation of white flakes of MgF_2 on the anode surface after discharge was observed [19]. These white flakes were considered as passivation layers, which resist the F^- ions migration at the anode. Similar performances were observed for both FIB cells. Nevertheless, both cells demonstrated the reversibility of Mg + MgF_2 anode material for RT-FIBs.

In the attempt to obtain insight into the capacity fading mechanism, impedance measurements were carried out on the Mg+MgF_2/$LiPF_6$/BiF_3-cell before and after cycling. Fig. 3 displays the Nyquist plots of the cell obtained before and after 5 cycles. According to literature, impedance spectra of cells using liquid electrolytes show two semicircles at high frequency and a tilted straight line at low-frequency region [21]. The first semicircle at high-frequency region would correspond to bulk resistance, and the second semicircle would correspond to charge transfer resistance of the electrodes. However, our impedance spectra do not show full semicircles due to overlapping of each other. After five

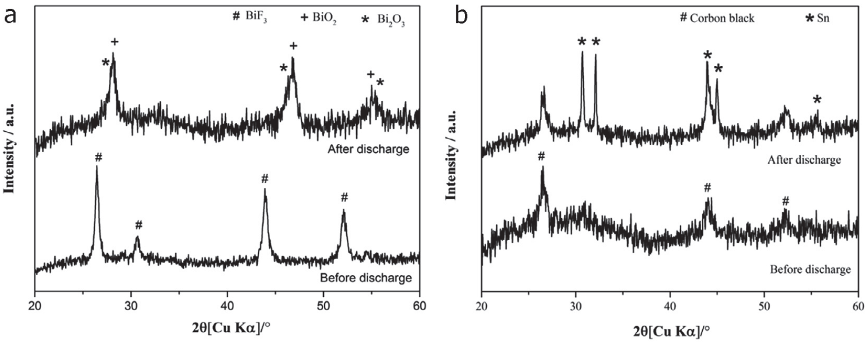

Fig. 4. XRD patterns of (a) BiF_3 and (b) SnF_2 cathodes before and after discharge.

discharge-charge cycles, the resistance of cell decreased slightly, confirming that internal resistance was not responsible for capacity fading. In addition to the passivation layer of MgF_2, electronic and ionic segregation of active material within the electrode could be the reason for fading which possibly came from volume changes of the electrode.

In order to understand the proposed mechanism of the electrochemical reaction, we recorded XRD patterns of the BiF_3 composite pellet before and after discharge, shown in Fig. 4a. Before discharge, diffraction peaks corresponding to BiF_3 were observed. This BiF_3-phase exhibits broad diffraction lines due to the presence of small crystallite sizes, which is common for ball-milled samples. After discharge, the peaks associated with BiF_3 disappeared, suggesting a complete conversion of BiF_3 at the cathode. In the XRD pattern, no peaks corresponding to the Bi-phase were seen, meaning, metallic Bi might be present in amorphous form. Further, new reflections above the noise level were observed, which were assigned to Bi_2O_3 and BiO_2. These oxides might have resulted from the chemical reaction of Bi with impurities. However, further studies are required to understand the full reaction mechanism. Fig. 4b shows the XRD pattern of SnF_2 pellet before and after discharge. Before discharge, few sharp peaks corresponding to carbon black were observed. In the XRD pattern, a broad peak centered at a 2θ value of 30 ° was obtained, corresponding to amorphous SnF_2 which was synthesized by ball milling. After discharge, new reflections appeared, which had been attributed to Sn, confirming the reduction of SnF_2 to the pure metal at the cathode.

4. Conclusion

In this study, we have demonstrated the reversibility of $Mg + MgF_2$ as anode against BiF_3 and SnF_2 cathodes using $LiPF_6$ as the electrolyte. We have investigated two types of FIB systems with BiF_3 and SnF_2 as cathodes, while $Mg + MgF_2$ was used as anode material. XRD measurements were carried out to investigate the electrochemical mechanism during the charge/discharge process. The BiF_3 based cell delivered as first discharge capacity $142\ mA{\cdot}h{\cdot}g^{-1}$, where the SnF_2 based cell exhibited a first discharge capacity of $160\ mA{\cdot}h{\cdot}g^{-1}$ at room temperature. These capacities were obtained at a high current density of $38\ \mu A{\cdot}cm^{-2}$. Capacity fading over cycling was observed in both cells. The fading upon cycling might be due to volume changes at electrodes and formation of a MgF_2 passivation layer at the anode. Nevertheless, this study opens a route to investigate new electrodes for FIBs applying the PF_6^- electrolyte systems.

Conflict of interest

None.

Acknowledgements

The work was financially supported by the Estonian Research Council (ETAg) through projects PUT126 and PUT 1534, the European Social Fund for project MTT68 and a TUT state stipend.

References

[1] S. Repp, E. Harputlu, S. Gürgen, N. Kremer, M. Castellano, F. Emen, N. Pompe, J. Wörner, A. Hoffmann, R. Thomann, S. Weber, K. Ocakoglu, E. Erdem, Synergetic effects of Fe^{3+} doped spinel $Li_4Ti_5O_{12}$ nanoparticles on reduced graphene oxide for high surface electrode hybrid supercapacitors, Nanoscale 10 (2018) 1877–1884.

[2] J.M. Tarascon, M. Armand, Issues and challenges facing rechargeable lithium batteries, Nature 414 (2001) 359–367.

[3] I. Hasa, D. Buchholz, S. Passerini, B. Scrosati, J. Hassoun, High performance $Na_{0.5}[Ni_{0.23}Fe_{0.13}Mn_{0.63}]O_2$ cathode for sodium-ion batteries, Adv. Energy Mater. 4 (15) (2014) 1400083.

[4] A. Eftekhari, Potassium secondary cell based on Prussian blue cathode, J. Power Sources 126 (2004) 221–228.

[5] Z. Zhao-Karger, X.Y. Zhao, D. Wang, T. Diemant, R.J. Behm, M. Fichtner, Performance improvement of magnesium sulfur batteries with modified non-nucleophilic electrolytes, Adv. Energy Mater. 5 (2015) 1401155.

[6] M.C. Lin, M. Gong, B. Lu, Y. Wu, D.Y. Wang, M. Guan, M. Angell, C. Chen, J. Yang, B.J. Hwang, H. Dai, An ultrafast rechargeable aluminium-ion battery, Nature 520 (2015) 324–328.

[7] X. Zhao, Sh. Ren, M. Bruns, M. Fichtner, Chloride ion battery: a new member in the rechargeable battery family, J. Power Sources 245 (2014) 706–711.

[8] M. Anji Reddy, M. Fichtner, Batteries based on fluoride shuttle, J. Mater. Chem. 21 (2011) 17059–17062.

[9] X. Zhao, Zh. Zhao-Karger, D. Wang, M. Fichtner, Metal oxychlorides as cathode material for chloride ion batteries, Angew. Chemie Int. Ed. 52 (2013) 13621–13624.

[10] P. Gao, M.A. Reddy, X.K. Mu, T. Diemant, L. Zhang, Z.R. Zhao-Karger, V.S.K. Chakravadhanula, O. Clemens, R.J. Behm, M. Fichtner, VOCl as a cathode for rechargeable chloride ion batteries, Angew. Chem. Int. Ed. 55 (2016) 4285–4290.

[11] X.Y. Zhao, Q. Li, T.T. Yu, M. Yang, K. Fink, X.D. Shen, Carbon incorporation effects and reaction mechanism of FeOCl cathode materials for chloride ion batteries, Sci. Rep. 6 (2016) 19448.

[12] F. Chen, Z.Y. Leong, H.Y. Yang, An aqueous rechargeable chloride ion battery, Energy Storage Mater. 7 (2017) 189–194.

[13] W. Baukal, R. Knodler, W. Kuhn, Overview of the applications of solid electrolytes, Chem. Ing. Tech. 50 (1978) 245–249.

[14] C. Rongeat, M. Anji Reddy, T. Diemant, R.J. Behm, M. Fichtner, Development of new anode composite materials for fluoride ion batteries, J. Mater. Chem. A 2 (2014) 20861–20872.

[15] D.T. Thieu, M.H. Fawey, H. Bhatia, T. Diemant, V.S.K. Chakravadhanula, R.J. Behm, C. Kübel, M. Fichtner, CuF_2 as reversible cathode for fluoride ion batteries, Adv. Funct. Mater. 27 (2017) 1701051.

[16] M.A. Nowroozi, K. Wissel, J. Rohrer, A.R. Munnangi, O. Clemens, $LaSrMnO_4$: reversible electrochemical intercalation of fluoride ions in the context of fluoride ion batteries, Chem. Mater. 29 (2017) 3441–3453.

[17] I. Mohammad, R. Witter, M. Fichtner, M.A. Reddy, Room temperature rechargeable solid state fluoride ion batteries, ACS Appl. Energy Mater. 1 (2018) 4766–4775.

[18] K.-I. Okazaki, Y. Uchimoto, T. Abe, Z. Ogumi, Charge-discharge behavior of bismuth in a liquid electrolyte for rechargeable batteries based on a fluoride shuttle, ACS Energy Lett. 2 (2017) 1460–1464.

[19] F. Gschwind, J. Bastien, Parametric investigation of roomtemperature fluoride-ion batteries: assessment of electrolytes, Mg based anodes, and BiF_3-cathodes, J. Mater. Chem. A 3 (2015) 5628–5634.

[20] Yazami, R., Fluoride Ion Electrochemical Cell. U.S. Patent January 29, 2009, US20090029237A1.

[21] V.S. Kolosnitsyn, E.V. Kuzmina, E.V. Karaseva, S.E. Mochalov, A study of the electrochemical processes in lithium-sulphur cells by impedance spectroscopy, J. Power Sources 196 (2011) 1478.

Curriculum vitae

Personal data

Name: Irshad Mohammad
Date of birth: 16.08.1989
Place of birth: Deoria (Uttar Pradesh)
Citizenship: India

Contact data

E-mail: irshad.mohammad636@gmail.com

Education

2015 – Until now Tallinn University of Technology – PhD
2011 – 2013 Indian Institute of Technology Madras – MSc
2006 – 2010 Buddha Post Graduate College Kushinagar – BSc
2004 – 2006 Krishak Intermediate College Deoria – Higher Secondary School

Language competence

English – Fluent
Hindi – Fluent
Urdu – Fluent

Professional employment

2014 – 2016 Tallinn University of Technology – Early Stage Researcher
2017 – 2018 Helmholtz Institute Ulm – Visiting Researcher

Elulookirjeldus

Isikuandmed

Nimi: Irshad Mohammad
Sünniaeg: 16.08.1989
Sünnikoht: Deoria (Uttar Pradesh)
Kodakondsus: India

Kontaktandmed

E-post: irshad.mohammad636@gmail.com

Hariduskäik

2015 – kuni praeguseni Tallinna Tehnikaülikool – PhD
2011 – 2013 Indian Institute of Technology Madras – MSc
2006 – 2010 Buddha Post Graduate College Kushinagar – BSc
2004 – 2006 Krishak Intermediate College Deoria – Higher Secondary School

Keelteoskus

Inglise keel – Kõrgtase
Hindi – Kõrgtase
Urdu – Kõrgtase

Teenistuskäik

2013 – 2016 Tallinna Tehnikaülikool – Nooremteadur
2017 – 2018 Helmholtz Institute Ulm – Külalisteadur